Title
Plasma-assisted Molecular Beam Epitaxy of Beta-Ga2O3: Growth, Doping, and Heterostructures

Author
Mauze, Akhil Ramnath Ganapati

Publication Date
2021

UNIVERSITY OF CALIFORNIA

Santa Barbara

Plasma-assisted Molecular Beam Epitaxy of Beta-Ga_2O_3: Growth, Doping, and Heterostructures

A dissertation submitted in partial satisfaction of the requirements for the degree

Doctor of Philosophy in Materials

by

Akhil Ramnath Ganapati Mauze

Committee in charge:

Professor James S. Speck, Chair

Professor Chris Palmstrom

Professor Umesh Mishra

Professor Chris Van de Walle

Professor Sriram Krishnamoorthy

December 2021

The dissertation of Akhil Ramnath Ganapati Mauze is approved.

Chris Palmstrom

Umesh Mishra

Chris Van de Walle

Sriram Krishnamoorthy

James S. Speck, Committee Chair

November 2021

Plasma-assisted Molecular Beam Epitaxy of Beta-Ga_2O_3: Growth, Doping, and Heterostructures

by

Akhil Ramnath Ganapati Mauze

Acknowledgements

I would like to thank my advisor Jim Speck for his guidance during my graduate research career. I am grateful for his direction and assistance in designing experiments, interacting with the research community, and developing my scientific mind. He always encouraged me to investigate my scientific curiosities with plenty of freedom and provided an example of enthusiasm for knowledge and critical thinking. I would also like to thank my committee members Chris Palmstrom, Chris Van de Walle, Umesh Mishra, and Sriram Krishnamoorthy. I have appreciated my discussions and collaboration with them furthering my scientific understanding and providing insight into my own research.

This experience was greatly helped by the MBE community at UCSB. In particular, Kurt Olsson and John English have been invaluable to my ability to conduct research and the development of my lab skills. Kurt is somehow able to manage the facilities for the MBE lab, assist with maintenances, fix and design critical components for our research equipment, and teach and be available for us researchers throughout the process. In addition, I would like to thank the various members of the MBE lab for their contribution to my research and making my experience at UCSB more enjoyable.

I would also like to thank the staff of the Microscopy, XRD, and Nanofab facilities for maintaining the tools researchers need to be productive and providing troubleshooting and help for us when we needed it. We are fortunate to have SSLEEC and Materials staff who have assisted me with anything administrative and helped me through my degree process. Additionally, I’d like to thank staff scientists Feng Wu and Tom Mates for their expertise and work characterizing material for the research presented throughout this dissertation. Feng Wu performed the TEM and APT necessary for much of this work, and Tom helped develop the SIMS analysis and train and assist me for the many SIMS measurements needed throughout these research projects.

I am lucky to have many great group members and fellow scientists who provided support, collaboration, and friendly conversations during my academic experience at UCSB. I'd like to thank Dr. Elaheh Ahmadi who trained me on the MBE and provided guidance and answers to any research or course related questions I had. I'd like to thank Dr. Yuewei Zhang and Takeki Itoh who I spent countless hours with performing maintenances, conducting experiments, and discussing research and life. I'd like to thank Dr. Esmat Farzana for her expertise on defect characterization and device processing and contribution to my research. I'd also like to thank the various other group members, Dr. Patrick Vogt, Dr. Sang-Heon Han, Nolan Hendricks, Kai Shek Qwah, Dr. Kelsey Jorgensen, Dr. Jianfeng Wang, Dr. Richard Cramer, Dr. Christian Robertson, and Dr. Morteza Monavarian for their insight and assistance in research, and for making the lab environment exciting and enjoyable. My colleagues have been valuable collaborators and friends throughout my time at UCSB.

Finally, I would like to thank my friends and family outside UCSB for their love and support during this process. My parents Smita and Ganapati Mauze have provided a shining example of hard work and virtue, and always encouraged me to pursue my interests. I'd also like to thank my sister Anisha who taught me so much about science growing up, and who is large part of the reason I decided to pursue a PhD.

Curriculum Vitae

Akhil Ramnath Ganapati Mauze

Santa Barbara, CA, 93117
(408) 242-1235 | akhilmauze@ucsb.edu

Education

University of California, Santa Barbara 2016-Present
In Progress: PhD Candidate, Materials

University of California, Los Angeles 2012-2016
B.S. Materials Science and Engineering, *Summa Cum Laude*

Experience

Graduate Student Researcher, Jim Speck Group, UCSB 2016- Present

- Growth of semiconductor thin films via molecular beam epitaxy
- Structural and materials characterization of film crystal quality
- Electronic analysis of semiconductor films for power electronic applications

Intern, Evans Analytical Group, Sunnyvale CA 2015

- Scanning electron microscopy on electronic and structural materials samples
- Ion polishing and sample preparation for various electron microscopy techniques

Skills

Molecular Beam Epitaxy Lab: Operation and maintenance of high vacuum equipment for plasma-assisted MBE and ozone MBE
Material Characterization: High Resolution X-ray Diffraction, Atomic Force Microscopy, Secondary Ion Mass Spectrometry, Scanning Electron Microscopy, Reflection High Energy Electron Diffraction, Optical Microscopy
Electronic Characterization: Hall measurement, Current-Voltage measurement
Processing: Tube Furnace Annealing, ICP etching, ion polishing, sputter coating, Dicing Saw
Data Analysis: MATLAB, Microsoft Excel, Origin, Mathematica

Graduate Teaching Assistant

- Graduate level Fundamentals of Electronic Solids
- Undergraduate Introduction to Materials Science

Awards and Honors

IEE Excellence in Research Graduate Fellowship	2020
Best Student Paper, Compound Semiconductor Week	2019
Outstanding Materials Science B.S. Award, UCLA	2016

Select Publications

Journal

A. Mauze, Y. Zhang, T. Itoh, and J.S. Speck. "Sn Doping of (010) β-Ga_2O_3 films grown by plasma-assisted molecular beam epitaxy" Applied Physics Letters 117, 222102 (2020).

A. Mauze, Y. Zhang, T. Itoh, F. Wu, and J.S. Speck, "Metal oxide catalyzed epitaxy (MOCATAXY) of β-Ga_2O_3 films in various orientations grown by plasma-assisted molecular beam epitaxy" APL Materials 8, 021104 (2020). (*Featured Article)*

A. Mauze, Y. Zhang, T. Mates, F. Wu, and J.S. Speck, "Investigation of unintentional Fe incorporation in (010) β-Ga_2O_3 films grown by plasma-assisted molecular beam epitaxy" Applied Physics Letters 115, 052102 (2019). (*Editor's Pick)*

S.H. Han, **A. Mauze** (co-first author), E. Ahmadi, T. Mates, Y. Oshima, and J.S. Speck. "n-type dopants in (001) β-Ga_2O_3 grown on (001) β-Ga_2O_3 substrates by plasma-assisted molecular beam epitaxy" Semiconductor Science and Technology 33, 045001 (2018).

A. Mauze, Y. Zhang, T. Itoh, H. Peelaers, C.G. Van de Walle, and J.S. Speck. "Mg doping and diffusion (010) β-Ga_2O_3 grown via plasma-assisted molecular beam epitaxy" Journal of Applied Physics. 130, 23 (to be published 2021).

A. Mauze, T. Itoh, Y. Zhang, F. Wu, and J.S. Speck. "001 β-$(Al_xGa_{1-x})_2O_3$ thin films grown via metal oxide catalyzed epitaxy" In Production.

Book Chapters

A. Mauze and J.S. Speck, 'Plasma-assisted molecular beam epitaxy I: Growth, doping, and heterostructures' M Higashiwaki and S Fujita. *Gallium Oxide: Materials Properties, Crystal Growth, and Devices.* Springer. 79-93. 2020

A. Mauze and J.S. Speck, 'Molecular Beam Epitaxy of β-Ga_2O_3' E. Farzana and J.S. Speck. *β-Ga_2O_3: Wide Bandgap Semiconductor Theory and Applications*. AIP Publishing. In Production

Conference and Workshop Presentations

"Sn Doping of β-Ga_2O_3 grown by plasma-assisted molecular beam epitaxy" Photonics West 2021, Virtual Conference (Oral Presenter)

"Metal Oxide Catalyzed Epitaxy: Growth and Sn doping of β-Ga_2O_3 in various orientations" Transparent Conductive Oxides 2019 Leipzig, Germany (Oral Presenter)

"Acceptors in (010) β-Ga_2O_3 grown by plasma-assisted molecular beam epitaxy" International Workshop on Gallium Oxide 2019 Columbus, Ohio (Oral Presenter)

"(010) β-Ga_2O_3 Metal Oxide Catalyzed Epitaxy (MOCATAXY) growth and Sn doping in plasma-assisted molecular beam epitaxy" Compound Semiconductor Week 2019 Nara, Japan (Oral Presenter) *Best Student Paper Award*

"Investigation of Fe incorporation in (010) β-Ga_2O_3 films grown by plasma-assisted molecular beam epitaxy" Compound Semiconductor Week 2019 Nara, Japan (Oral Presenter)

"Mg doped (010) β-Ga_2O_3 grown by plasma-assisted molecular beam epitaxy" Compound Semiconductor Week 2018 Boston, Massachusetts (Poster Presenter)

"Growth of Ge and Sn doped (001) β-Ga_2O_3 by PAMBE" International Workshop on Gallium Oxide 2017 Parma, Italy (Oral Presenter)

Abstract

Plasma-assisted Molecular Beam Epitaxy of Beta-Ga_2O_3: Growth, Doping, and Heterostructures

by

Akhil Ramnath Ganapati Mauze

As conventional semiconductors reach their materials limits for modern high power switching applications, we must look towards new materials systems. Ultrawide bandgap semiconductors provide opportunities for future efficient high voltage switches due to their ability to withstand high electric fields. In particular, β-Ga_2O_3 shows promise due to its high critical electric field (6-8 MV/cm), availability of high-quality melt grown bulk substrates, and donor and deep acceptor doping possibilities. This work focuses on growth and doping of β-Ga_2O_3 and its alloys via plasma-assisted molecular beam epitaxy (PAMBE).

Conventional PAMBE shows promise for (010) β-Ga_2O_3 growth, however other crystallographic orientations have lower growth rates and poor film quality due to significant suboxide desorption during growth. An indium catalyzed growth mechanism using an additional indium flux during PAMBE growth of β-Ga_2O_3 is demonstrated, allowing for significantly improved growth rates across various crystallographic orientations. This metal oxide catalyzed epitaxy (MOCATAXY) allows for improved film quality, demonstrated by minimal extended defects and smoother surface morphologies, particularly for (001) β-Ga_2O_3. The supplied In flux during MOCATAXY growth acts as

a catalyst, allowing for growth at high growth temperatures and Ga fluxes for which growth would not occur for conventional PAMBE. This In limits suboxide desorption during growth and does not incorporate into the film for sufficiently Ga rich growth conditions.

Donor doping is necessary for achieving a variety of device designs, with its use in contacts, channels, modulation doping, and drift regions. Donor doping with Ge, Sn, and Si is demonstrated for β-Ga_2O_3 grown on various orientations. While Ge doping can be used for a range of concentrations for conventional PAMBE, at higher growth temperatures and Ga fluxes its incorporation decreases, limiting its use for MOCATAXY. Sn shows the ability to achieve high doping concentrations in conventional PAMBE, however surface segregation during growth and a delay in incorporation into the film is observed for lower concentrations. Sn doping during MOCATAXY growth, however, allows for sharp, controllable doping profiles for a variety of Sn concentrations across various orientations. Furthermore, Sn doping of (010) β-Ga_2O_3 via MOCATAXY demonstrates the highest electron mobility for continuously doped β-Ga_2O_3 grown via MBE. Sn doping of (001) β-Ga_2O_3 via MOCATAXY shows significantly higher electron mobility than conventional PAMBE. Si doping is also investigated, showing degradation of (010) β-Ga_2O_3 film quality, however promising electron mobility and high doping concentrations were achievable for (001) oriented growth via MOCATAXY.

Deep acceptor doping allows for realization of potential barriers in β-Ga_2O_3, as well semi-insulating regions of the device, such as current blocking layers for vertical structures and an intentionally compensated film-substrate interface for lateral devices. Mg is investigated as an intentional dopant in conventional PAMBE growth of (010) β-Ga_2O_3.

While sharp doping profiles and a range of doping concentrations are achievable, annealing at high temperatures (≥ 925 °C) allows for diffusion of Mg, limiting its application to lower growth temperature epitaxial techniques and processing steps. A mechanism of Mg diffusion via the mobile Mg interstitial species is proposed, involving interactions of point defects in the film during annealing. Additionally, Fe incorporation into β-Ga_2O_3 films grown on Fe doped substrates is shown to be the result of surface segregation, rather than diffusion. This incorporation can be limited using a low temperature Fe trapping buffer layer prior to growth of critical regions of the film structure.

Finally, growth of heterostructures with β-$(Al_xGa_{1-x})_2O_3$ via MOCATAXY is investigated. Maximum Al contents for (010) β-$(Al_xGa_{1-x})_2O_3$ of 22% are achieved with high quality, coherently strained films. (001) β-$(Al_xGa_{1-x})_2O_3$ films with Al contents up to 15% are also grown with smooth surface morphology and no evidence of extended defects or relaxation. A relationship between out of plane lattice parameter is derived using the fundamental stiffness tensor and stress and strain expressions for (001) β-$(Al_xGa_{1-x})_2O_3$ coherently strained to the β-Ga_2O_3. Confirmation of the Al content in the films confirms the validity of the derived relationship. This demonstration of high quality (001) β-$(Al_xGa_{1-x})_2O_3$ shows promise for future heterostructure based devices in this orientation.

Table of Contents

Chapter 1: Introduction to β-Ga_2O_3 and Molecular Beam Epitaxy

1.1 Semiconductors Materials for Power Electronics

The world's ever growing electrical power consumption necessitates semiconductor power switches to service various applications from logic to high power conversion. Converting between alternating current (AC) used to transport electricity over long distances and direct current (DC) more commonly used by devices or outputted from batteries requires electrical switches. There are many steps between AC and DC and even DC-DC and AC-AC required to convert electrical power from the form of generation to the final power requirements of the end use device, and the modern applications need higher voltage and frequency switching. As environmental and cost considerations require higher efficiency switching at these high powers, novel device designs and new materials must be investigated.

Silicon-based devices have dominated power electronics for many decades for these applications with innovations in device architecture pushing power limits higher between generations from metal-oxide field effect transistors (MOSFETs) to insulated gate bipolar transistors (IGBTs) and superjunction transistors. As the demand for higher frequency and higher voltage switching increases, the fundamental materials limits of Si are reached. Wide bandgap semiconductors such as SiC and GaN, with bandgaps of 3.3 eV and 3.4 eV respectively, have entered the power electronics market in the past couple of decades. Their ability to sustain a higher electric field within the material before breakdown allows for them to achieve higher voltage and ultra-scaled device designs with efficient power conversion relative to Si. SiC devices such as diodes, MOSFETs, and junction-gate field effect transistors (JFETs) have entered the market and grown in application over the past decade. Alternative devices based on GaN, as well as AlGaN/GaN high electron mobility transistors (HEMTs) have also entered the market over the past decade, with nitride rf devices for microwave applications showing particular success. For high voltage switching, wide bandgap semiconductors have allowed for smaller resistive losses in the on-state than conventional semiconductors for a given voltage rating of a device. For high frequency applications, wide bandgap semiconductors can reduce switching losses in the device and the higher frequency switching achievable also allows for the size reduction of passive components in power electronic circuits.[1]

Looking to future power device applications, a number of ultra-wide bandgap semiconductor materials systems show promise. Diamond and AlN both have large bandgaps, high theoretical critical electric fields, and good mobility, however lack of high quality bulk substrates and inefficient ionization of dopants provide challenges for those materials systems. Gallium oxide has gained much interest over the past decade as an ultra-wide bandgap (4.8 eV)[2] semiconductor due to its high critical electrical field (6-8 MV/cm)[3-4], availability of high-quality melt grown bulk substrates[5-6], and n-type[7-12] and deep acceptor[13-15] doping possibilities. Investigation of the materials system is still in a relatively early stage, but demonstration of growth, doping, and device applications, as well as investigation into the materials limits of gallium oxide has already begun to show its promise for power electronics.[16]

1.2 Power Device Figures of Merit

Many figures of merit (FOMs) have been derived for various semiconductor devices to forecast the ability of a materials system to produce efficient devices and meet the requirements of those applications based on its fundamental materials properties. While they often don’t encompass all the requirements for the development of a materials system into optimized, commercially competitive devices, they can guide material selection and incentivize investigation into a materials system. For power electronics, the Baliga FOM is used to describe the trade-off between breakdown voltage and on resistance for an optimally designed device in a materials system.[17-18] This on-resistance (R_{on}) depends on dielectric constant of the material (ε), mobility (μ), breakdown field (F_{BR}), and the designed breakdown voltage of the device (V_{BR}) via the relationships below:

$$R_{ON} = \frac{4{V_{BR}}^2}{\mu\varepsilon {F_{BR}}^3} \text{ (eq. 1.1)}$$

Where the denominator of this equation is the Baliga FOM (BFOM):

$$BFOM = \mu\varepsilon {F_{BR}}^3 \text{ (eqn. 1.2)}$$

This expression for on-resistance assumes a triangular field profile in a drift layer across which the voltage is dropped in the off state. The peak field in this drift layer near the junction of the device is assumed to be the breakdown field of the materials system, and the drift layer thickness and net doping concentration to achieve a given breakdown voltage of an optimally designed device would be chosen such that this field approaches zero at the drain contact. This electric field profile is shown in Fig. 1.1.[19] One major assumption applied to this BFOM is the existence of a shallow, hydrogenic dopant in the materials system. While this is common for many conventional semiconductors, inefficient ionization limits certain ultrawide bandgap semiconductors like AlN and diamond, limiting carrier concentration in the drift region and therefore increasing on-state resistance. To account for this, Zhang et al. derived a modified BFOM reflecting the lower on-resistance for materials systems with lower ionization efficiency in the drift region.[19] An ionization efficiency term, calculated as the ratio of fully ionized dopants (n) to donor concentration (N_D), is added as shown in the equations below:

$$R_{ON} = \frac{N_D}{n}\frac{4{V_{BR}}^2}{\mu\varepsilon {F_{BR}}^3} \quad \text{(eq. 1.3)}$$

$$modified\ BFOM = \frac{n}{N_D}\mu\varepsilon {F_{BR}}^3 \quad \text{(eqn. 1.4)}$$

Additionally, for a device of a given materials system to hold the larger range of voltages before breakdown, a low net carrier concentration in the drift region is desired. This allows for a thicker drift layer to be depleted, leading to a higher voltage held in reverse bias. Background impurities introduced into a material during growth can limit the minimum carrier concentration achieved in this drift region, thus limiting the breakdown voltages attainable for a device. Zhang et al.[19] plotted the theoretical on resistance vs. breakdown voltage for various materials systems based on demonstrated materials properties, ionization efficiencies, and state of the art background impurity limits as shown in Fig. 1.2. β-Ga_2O_3 shows the lowest on-resistance for the high range of breakdown voltages plotted, suggesting it could be an intriguing material choice for future high power switching applications. One thing to note is that these FOMs demonstrate the ability to minimize the on resistance of a drift region, but other series resistances exist in the device, such as contact resistances. The fundamental material properties for the semiconductors demonstrated in

Fig. 1.2 are shown in Table 1.1. Additionally, BFOMs and modified BFOMs are shown, normalized to Si. Furthermore, processing and growth constraints, and compatibility with other materials like dielectrics can play a role in ultimately realizing efficient devices for commercialization.

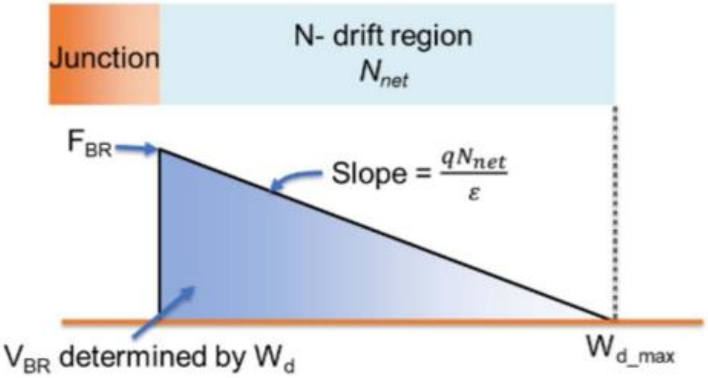

Figure 1.1: Example of triangular electric field profile in depleted n- region of a junction for maximum breakdown voltage from Zhang et al.[19]

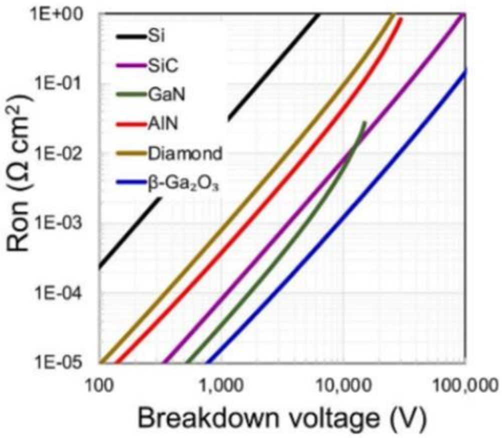

Figure 1.2: Comparison of theoretical minimum R_{on} for n- drift regions with thickness and doping corresponding to different breakdown voltages based on state of the art material purity that limits the minimum doping concentrations achievable, and using the revised figure of merit that considers doping ionization efficiency and demonstrated material mobility.[19]

Table 1.1: Material Properties of various semiconductors that contribute to revised Baliga Figure of Merit (relative to Si).[19-20]

	Si	**4 H-SiC**	**GaN**	**β-Ga_2O_3**	**AlN**	**Diamond**
E_g (eV)	1.12	3.23	3.39	4.8	6.2	5.5
ε_r	11.7	9.7	8.9	10	9	5.7
μ (cm^2/Vs)	1350	900	1500	200	426	2200
F_{BR} (MV/cm)	0.3	2.5	3	8	15.4	13
E_D (meV)	45	60	20	30	280	370 (E_A)
BFOM	1	320	1400	2400	32834	64600
Modified BFOM (5 kV)	1	317	1368	2161	508	450

1.3 β-Ga_2O_3: Materials Properties and Device Designs

Ga_2O_3 has several polytypes, but the monoclinic β-gallia structure is the stable phase of Ga_2O_3 and single crystal β-Ga_2O_3 can be congruently grown from a melt. This β-phase is the most researched polytype of Ga_2O_3, however the α-phase and ε-phase also show some interesting properties. The rhombohedral structure of the α-phase is the same as α-Al_2O_3, giving it potential for heteroepitaxy on sapphire substrates and interesting alloying applications with Al. The hexagonal ε-phase has a large predicted spontaneous polarization, suggesting that heterostructures created by alloying with Al could allow for formation of a two-dimensional electron gas (2DEG) without intentional doping, similar to the AlGaN/GaN materials system. Still, the demonstrated high breakdown fields, doping possibilities, and high-quality bulk substrates make the β-phase extremely promising for power electronics, and therefore the main focus of this work.

Figure 1.3 shows the monoclinic β-Ga_2O_3 crystal structure (space group $C\frac{2}{m}$) with the unique b-axis and a β angle of 103.7°. The conventional unit cell contains 20 atoms while the primitive cell contains 10 atoms. The three O sites are inequivalent, with two having threefold coordination and one having fourfold coordination. The two Ga sites are the tetrahedrally coordinated Ga(I) and octahedrally coordinated Ga(II). The anisotropy of the monoclinic structure leads to significant differences in the properties of its principal planes. Cleavage planes in the [010] zone such as the (100) and ($\bar{2}$01) planes can provide some limitations on bulk substrate growth, while epitaxial growth on these orientations can be affected by weak out of plane bonding.

One of the primary bulk substrate growth methods is edge defined film-fed growth (EFG), which involves pulling a slab of β-Ga_2O_3 congruently from a melt. Due to the cleavage planes in the [010] zone, the [010] is typically used as the pulling direction, limiting the area of the (010) oriented substrates grown via this method, but allowing orientations like (100), (001), and ($\bar{2}$01) to be scalable to larger areas, with 6" substrates already demonstrated. Czochralski is also being developed for β-Ga_2O_3 with 2" substrates already demonstrated in the (010) orientation. Bulk substrates provide an excellent template for epitaxial growth of β-Ga_2O_3, and extended defects in β-Ga_2O_3 bulk substrates are already lower than 10^3 cm^{-2}, which is significantly lower than alternative wide bandgap and ultra-wide bandgap semiconductors.[5-6]

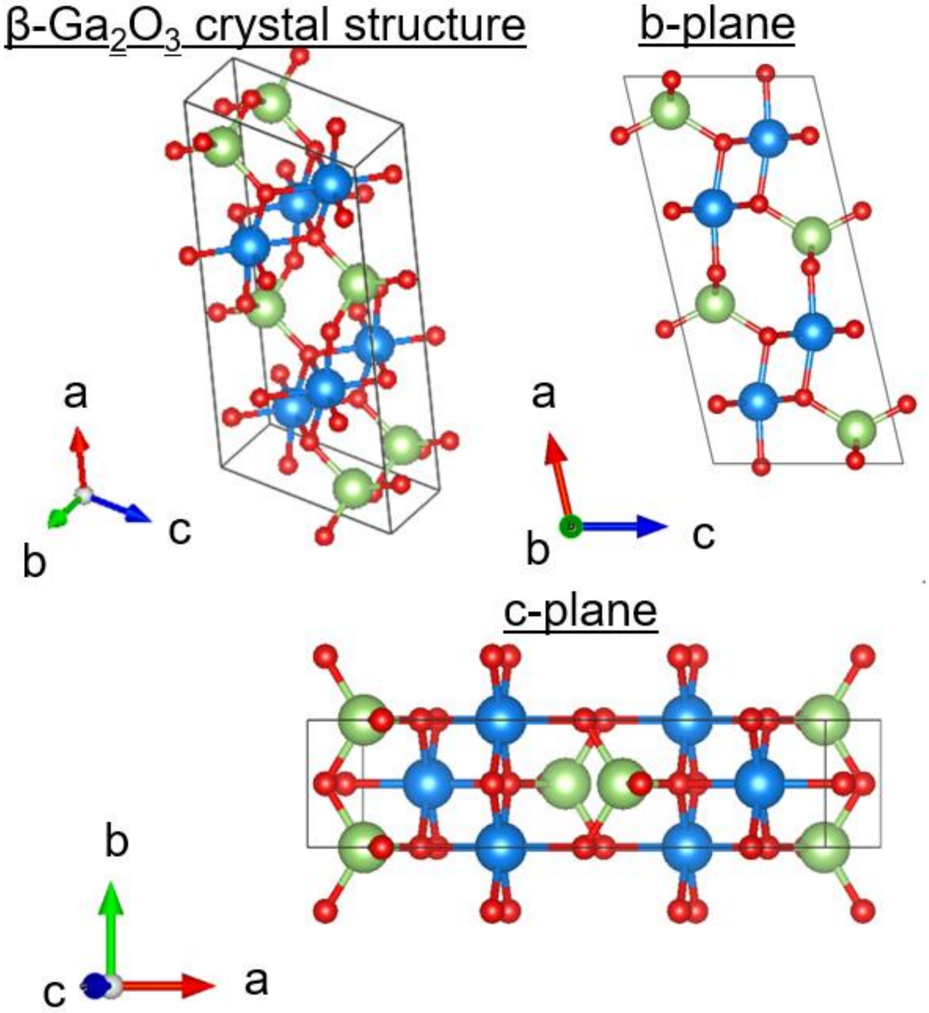

Figure 1.3: β-Ga_2O_3 monoclinic crystal structure along with b-plane and c-plane orientations. The blue and green atoms represent the Ga (I) and (II) sites respectively and the red atoms represent the O sites. This structure was produced via VESTA Software.

The ability to dope a semiconductor is necessary to achieve various device designs. β-Ga_2O_3 has demonstrated n-type doping with Si, Ge, and Sn giving it the potential for electron devices.[20] Additionally, the availability of shallow dopants allows for the efficient ionization needed to minimize on resistance as described by the modified Baliga figure of merit in eqn. 1.4. P-type doping has not been demonstrated due to negligible valence band dispersion, strong hole self-localization, and large acceptor ionization energies.[21] Still, deep acceptor dopants provide the ability to create large barriers in the material, as well as semi-insulating regions in unipolar devices. Deep acceptor dopants like Fe, Mg, and N have been used in β-Ga_2O_3. Doping with donors and deep acceptors will be discussed in detail more in Chapters 3 and 4.

In addition to doping, utilization of alloys can allow for bandgap engineering to produce different classes of devices in semiconductors. Alloying β-Ga_2O_3 with Al or In can change the bandgap, with the β-$(Al_xGa_{1-x})_2O_3$ alloy of particular interest for heterostructure based transistors. The β-$(Al_xGa_{1-x})_2O_3$ / β-Ga_2O_3 heterostructure is similar to the AlGaAs/GaAs heterostructure and can be used for modulation doped field effect transistors (MODFETs). Still, there are many materials considerations in producing this β-$(Al_xGa_{1-x})_2O_3$, which will be discussed in more detail in Chapter 5.[22-23]

There are various devices designs for application of β-Ga_2O_3. One of the simplest devices that utilizes voltage dropped over a thick n- layer is a Schottky barrier diode (SBD). As described earlier, efficient low doping in the drift region can allow for larger voltages to be held across this layer in the off-state, with efficient conduction in the on-state. Figure 1.4a shows a schematic of this device structure. Doping with a deep acceptor under the metal source contact can allow for higher barriers at the junction and less likelihood for tunneling at higher voltages, however there would be a trade-off with on-resistance.[24-25]

Another vertical device that could also be applicable to β-Ga_2O_3 is a vertical FET. Figure 1.4b shows a schematic of a vertical FET based on a current aperture similar to the one demonstrated by Wong et al.[26] Voltage is similarly dropped across a thick drift layer, but this device has three terminals, and is turned on an off via the gate. In the on state, current flows from the source contacts down through the aperture and drift region, and through the n+ substrate and drain contact. The aperture in the n- region is surrounded by semi-insulating current blocking layers which can be deep acceptor doped. The peak field in such a device would be just beneath these at the junction between the drift region and acceptor doped region. A similar vertical FET could use a vertical fin instead of an aperture through which current flows. This structure would require etching of the fin region, but would not need acceptor doped current blocking layers.[27]

A third device design that has been demonstrated is a modulation doped field effect transistor based on the β-$(Al_xGa_{1-x})_2O_3$ / β-Ga_2O_3 heterostructure. This device does not rely on dropping a large voltage across an n- layer. It involves lateral conduction through a two-dimensional electron gas channel (2DEG) formed just below the heterostructure interface. A schematic of this device is shown in Fig. 1.4c, with the 2DEG charge controlled by the conduction band offset between the β-$(Al_xGa_{1-x})_2O_3$ and β-Ga_2O_3, as well as the intentional doping of the β-$(Al_xGa_{1-x})_2O_3$ film and thicknesses of the UID and doped β-$(Al_xGa_{1-x})_2O_3$ layers. This channel is turned on and off with a gate voltage. Scaling of the device can take advantage of the high critical field in β-Ga_2O_3 by allowing for shorter channels with reduced on-resistance.[22-23]

These device architectures shown in Fig. 1.4 will be referenced throughout this dissertation as applications ultimately determine the materials requirements of a semiconductor system. Much progress in β-Ga_2O_3 growth and processing is still needed to produce optimized devices that can be commercialized. Various epitaxial growth techniques have been demonstrated for β-Ga_2O_3. Hydride vapor phase epitaxy (HVPE) and metal organic chemical vapor deposition (MOCVD) have both shown the potential to grow low net doping, high mobility films of β-Ga_2O_3 with relatively fast growth rates, already providing a pathway towards future commercialization.[28-29] Molecular beam epitaxy (MBE) is a growth technique that allows for growth high quality film structures of β-Ga_2O_3 and its alloys with precise control of film interfaces and doping. MBE is used for growth of all the thin films in the studies of this dissertation.

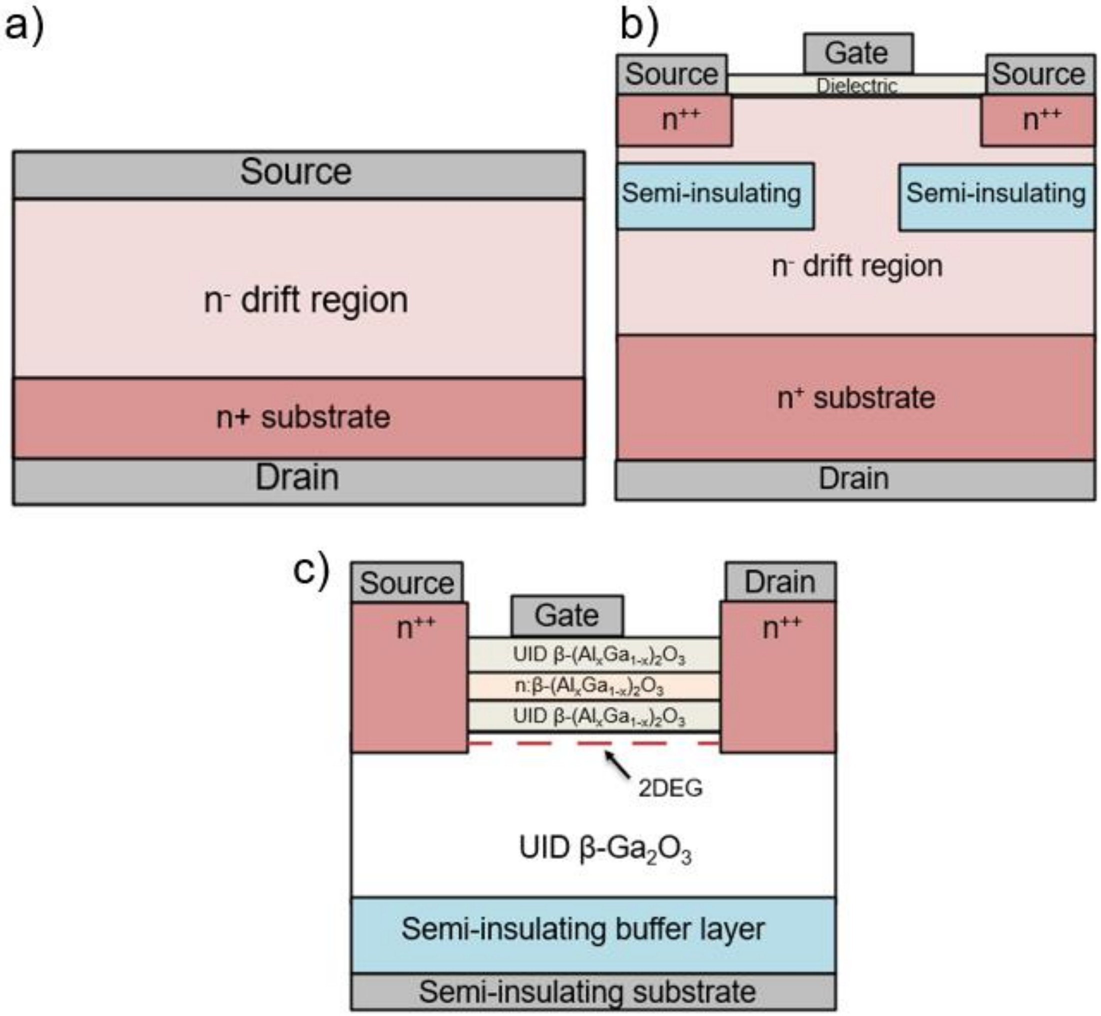

Figure 1.4: Various β-Ga_2O_3 devices structures including a Schottky barrier diode (a), vertical field effect transistor similar to one from Wong et al.[26] (b), and a modulation doped field effect transistor (c).

1.4 Basics of Molecular Beam Epitaxy

Molecular Beam Epitaxy (MBE) is an ultra-high vacuum technique in which thin films are slowly grown on a substrate via sublimated, evaporated, or gas sources. MBE has been used for growth a variety of semiconductor systems, with much of the technique’s development due to its use in growth of III-Vs. The clean environment and controllable deposition possible via MBE have allowed for some of the highest quality thin films and devices structures to be grown for various materials systems, making it an excellent technique for researching semiconductor materials systems.

During MBE growth, the substrate is held at temperatures that are high enough for surface diffusion of adatoms, allowing them to attach to their sites in the crystal structure, while being low enough to limit bulk diffusion and maintain abrupt interfaces in the film. Both high purity sources and the ultra-high vacuum environment are necessary to produce controlled deposition with limited unintentional impurity incorporation into the thin films. The use of cryopumps, turbo pumps, and a liquid nitrogen cooled shroud during growth allow for this ultra-high vacuum to be maintained. Additionally, following maintenances or source material loading involving exposure of the MBE chamber to the atmospheric environment, baking the system to remove water and other impurities from the chamber walls combined with leak checking all ports is necessary. Intro and buffer chambers are used for sample loading, baking, and cleaning, so as not to contaminate the clean environment of the growth chamber.

In addition to cleanliness and controlled deposition, the ability to perform in-situ characterization of films during growth provides an advantage for MBE growth. Reflection high energy electron diffraction (RHEED) is one such technique that uses an electron beam incident upon the sample at a small angle to produce a diffraction pattern on a phosphorescent screen. Analysis of the RHEED diffraction pattern yields information on surface structure including features such as roughness, reconstructions, and faceting. The time evolution of the RHEED pattern also provides information on the growth mode. Spotty RHEED patterns are indicative of a rough surface while smooth, two-dimensional film growth produces a "streaky" pattern. Growth rates can also be determined from oscillations in spot intensity in the RHEED patterns over time during layer-by-layer growth.

For MBE of β-Ga_2O_3 and its heterostructures, group III fluxes come from evaporation of liquid Ga, In, or Al at elevated temperatures in effusion cells. The absolute fluxes of these elements can be measured via a nude ion gage in the MBE chamber in terms of beam equivalent pressure (BEP). Commonly fluxes for growth of the binary compound or its alloys range from 10^{-8} torr to mid 10^{-7} torr with some dependence on the experimental set up and growth rate. Dopants such as Sn, Ge, Si, and Mg have been used to produce n-type or semi-insulating β-Ga_2O_3 via evaporation or sublimation of source material in effusion cells. While dopant fluxes are typically too low to measure in the MBE via the nude ion gage, they can be correlated with cell temperatures after calibration using ex-situ secondary ion mass spectroscopy (SIMS) or electrical measurements to determine doping concentrations in the films. Metal sources for MBE must be extremely pure, with 7N purity (99.99999%) typical for semiconductor growth that requires high purity and minimal background doping. The system used in the work presented is a Veeco 620 MBE with a vertical orientation, allowing for the sample to face down towards the vertically oriented source material. A schematic of our MBE setup is shown in Fig. 1.5.

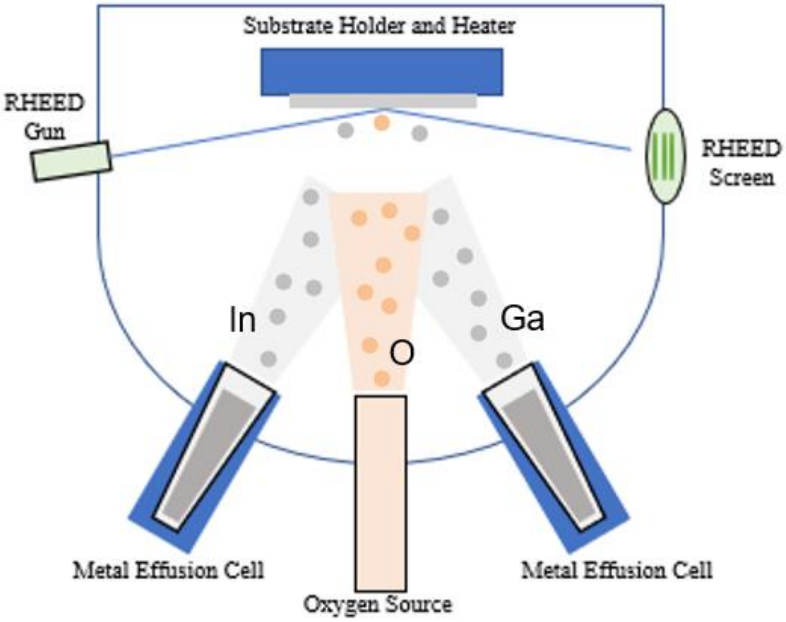

Figure 1.5: Schematic of molecular beam epitaxy chamber used for PAMBE of β-Ga_2O_3.

Introduction of oxygen to the growth environment via gas lines and mass flow controllers can provide an oxygen flux, however molecular oxygen (O_2) is not reactive enough at growth temperatures for conventional MBE growth of β-Ga_2O_3. Atomic oxygen (O) or ozone (O_3) can be used as the reactive species for oxide MBE growth. In plasma-assisted molecular beam epitaxy (PAMBE), a radio frequency plasma source can produce atomic O from molecular O_2 to create an active O flux towards the substrate.[30-31] This atomic O can react with Ga or other group III elements to grow β-Ga_2O_3 and its alloys. The growth rate of β-Ga_2O_3 is limited by the concentration of O that can be produced from O_2 with 1-2% O typical of modern rf plasma sources. Growth rates for PAMBE of β-Ga_2O_3

are therefore limited to 1-5 nm/min with chamber pressures around 10^{-5} torr due to the abundance of O_2 in the growth environment. [8,10,32]

1.5 β-Ga_2O_3 Molecular Beam Epitaxy

Early MBE β-Ga_2O_3 growth studies involved $(\bar{2}01)$ β-Ga_2O_3 on c-plane sapphire due to the widespread availability and low cost of sapphire substrates. $(\bar{2}01)$ β-Ga_2O_3 grows on c-plane sapphire due to the similar arrangement of oxygen atoms on both planes. Still, the lattice mismatch and rotational domains present lead to more defects in heteroepitaxial β-Ga_2O_3.[32] The growing availability of high-quality melt grown substrates via techniques like Czochralski and Edge-defined film fed growth (EFG) have allowed for a focus on homoepitaxy of β-Ga_2O_3.[5-6] Because homoepitaxy allows for no lattice mismatch and the ability to create relatively defect free interfaces between substrate and film, it is preferable for epitaxial films with the high structural quality and excellent electronic properties needed for electron devices. (100) β-Ga_2O_3 was one of the first investigated via homoepitaxy, showing significant smoother surface morphology and lower mosaic than heteroepitaxy. Tsai et al. demonstrated slightly O-rich growth at a growth temperature of 700 °C.[32]

The work of Tsai et al. showed the impact of the Ga_2O suboxide formation during growth. For constant effective oxygen flux, for Ga-rich growth, the growth rate decreased as Ga flux increased. This phenomenon is due to the suboxide formation limiting maximum growth rate via the following reaction:

$$Ga_2O_3 + 4Ga \rightarrow 3Ga_2O \quad \text{eq. 1.1}$$

This suboxide forms more readily at higher growth temperatures, limiting the maximum growth temperatures at which β-Ga_2O_3 growth occurs. At extremely high Ga/O flux ratios, etching of the Ga_2O_3 occurs.[32-33] The effect of this suboxide formation has also been observed in MBE of other oxides like SnO_2 and In_2O_3.[34-35] Typical growth temperatures for MBE to maintain high quality growth and sufficient growth rates are around 500 °C to 750 °C, depending on orientation and film structure requirements. Additionally, Ga/O flux ratios near stoichiometry allow for the highest quality growth and highest growth rates.

Vogt et al. studied the nature of desorbing and adsorbing fluxes during PAMBE growth of $(\bar{2}01)$ β-Ga_2O_3 on sapphire substrates using quadrupole mass spectroscopy (QMS). The Ga_2O suboxide was confirmed to be the primary desorbing flux from the substrate during Ga rich growth, with almost all the supplied Ga flux either contributing to growth or desorbing via this suboxide. Lower growth temperatures and more O-rich conditions limit this suboxide desorption as more of the supplied Ga flux incorporates into the film.[36]

This suboxide desorption defines the growth regimes for typical PAMBE growth. Figure 1.6 from Oshima et al. shows the dependence of growth rate on Ga flux for different orientations.[33] For a fixed active O flux, at lower Ga fluxes, the growth rate was proportional to the Ga flux. At higher Ga fluxes near stoichiometry, the growth rate saturated at the maximum growth rate in the Plateau regime. At very high Ga flux, growth rate decreased due to sufficiently high suboxide desorption. In the absence of any active O flux, a supplied Ga flux etched the Ga_2O_3. This etch has been used to clean the surface of the substrate prior to growth, reducing impurities like Si that can accumulate at the growth interface. Another in-situ polish used in PAMBE involves an incident atomic O flux in the absence of Ga at an elevated temperature. This can also help clean the substrate surface prior to growth, potentially due to oxidation followed by desorption of similar impurities.[22]

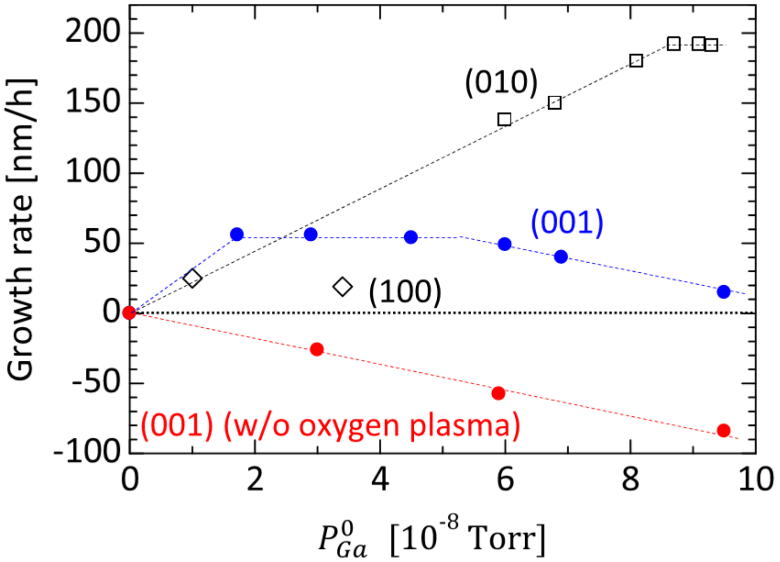

Figure 1.6: Comparison of growth rate vs. Ga flux for constant O flux across various orientations of β-Ga_2O_3 PAMBE growth.[33]

1.6 Orientation Dependence of MBE Growth of β-Ga_2O_3

The monoclinic crystal structure of β-Ga_2O_3 leads to anisotropy in materials properties for different crystallographic planes. As can be seen in Fig. 1.6, the maximum growth rate achievable for the same active O flux varies based on the orientation of the β-Ga_2O_3 substrate.[33] Orientations like (100), ($\bar{2}$01), and (001) show higher suboxide desorption than the (010) orientation, leading to poorer film quality and lower maximum growth rates on these orientations than (010).[7,33] While melt-grown substrates are available for all of these orientations, (100), ($\bar{2}$01), (001), and other planes in the [010] zone are scalable via EFG growth, a melt growth technique that involves pulling a slab of crystal β-Ga_2O_3 along the [010] direction. Limitations of cleavage during melt growth have led to difficulty scaling the (010) plane, however improvements on EFG and Czochralski growth have shown promise with 2" (010) β-Ga_2O_3 substrates now available. [5-6]

Sasaki et al. first demonstrated the importance of crystallographic orientation on growth rates and film quality via ozone MBE. It was shown that growth on the (100) cleavage plane had extremely low growth rates less than 0.1 µm/h while the (001) and ($\bar{2}$01) orientations showed moderate growth rates around 0.5 µm/h and (010) growth rates exceeded 0.7 µm/h. Additionally, extremely smooth surface morphology was achieved on the (010) orientation, while ($\bar{2}$01) showed a rough surface morphology in atomic force microscopy (AFM) and twin defects in transmission electron microscopy (TEM). (010) β-Ga_2O_3 films grown via ozone MBE demonstrated a relatively high electron mobility (> 100 cm^2/Vs) showing promise for future devices based on films grown in this orientation. This identification of (010) as the orientation with the highest growth rates and best film quality for MBE by Sasaki et al. led to its investigation as the primary orientation for future MBE growth studies.[7]

Development of (010) β-Ga_2O_3 growth via PAMBE also yielded promising film quality and devices. Okumura et al. and Ahmadi et al. demonstrated (010) growth in the O-rich and Plateau regime of growth.[8,37] (001) and ($\bar{2}$01) β-Ga_2O_3 films have also been grown via PAMBE, demonstrating significantly lower growth rates and rougher surface morphologies than (010) β-Ga_2O_3. Figure 1.7 shows a comparison of maximum growth rates for β-Ga_2O_3 grown via conventional PAMBE for different orientations and growth temperatures, represented by the red data points. For the same oxygen plasma conditions, the maximum growth rate of 2.4 nm/min was possible for the (010) orientation, while growth on (001) and ($\bar{2}$01) β-Ga_2O_3 yielded maximum growth rates less than 1 nm/min.[10,33] Similar to ozone MBE, the higher suboxide decomposition planes showed lower maximum growth rates. Additionally, maximum room temperature electron Hall mobility in continuously doped PAMBE grown films for (001) β-Ga_2O_3 (39 cm^2/Vs) is significantly lower than those achieved for (010) β-Ga_2O_3 (120 cm^2/Vs).[8-10] Typical growth temperatures of 600 to 700 °C were optimal for (010) β-Ga_2O_3 while temperatures around 750 °C were optimal for smooth (001) β-Ga_2O_3 films.[33] Even under their best growth conditions, (001) and ($\bar{2}$01) β-Ga_2O_3 films grown via PAMBE showed significantly rougher surface morphologies than the (010) orientation as shown in the AFM images in Fig. 1.8.[10]

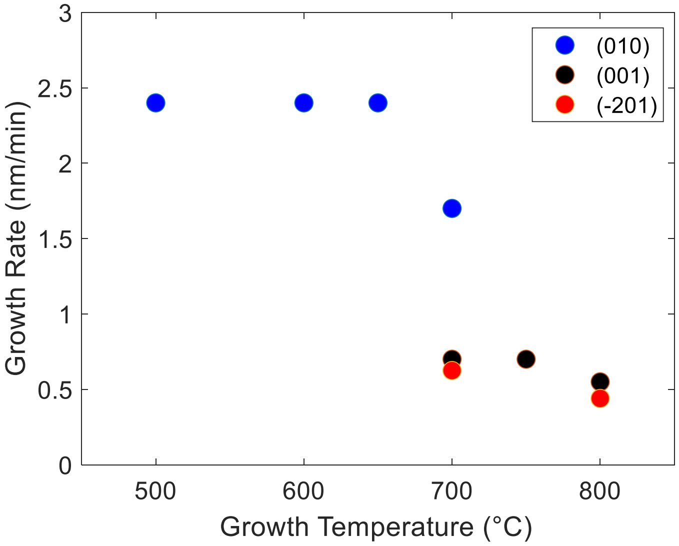

Figure 1.7: Maximum growth rate vs. growth temperature for various orientations of PAMBE growth of β-Ga_2O_3.

Despite having different growth rates and surface roughness, surface morphologies for PAMBE grown films across different orientations show similar features, with optimal growth conditions producing elongated grooves. For the (001) and ($\bar{2}01$) growth, these grooves are oriented along the [010] direction while (010) film morphologies have grooves oriented along the [001] direction as seen in Fig. 4. Mazzolini et al. characterized these grooves in (010) growth via RHEED and AFM to identify the (110) and ($1\bar{1}0$) facets on this surface.[38] Itoh et al. grew homoepitaxial films on (110) β-Ga_2O_3 to reveal similar growth characteristics to the (010) orientation.[39]

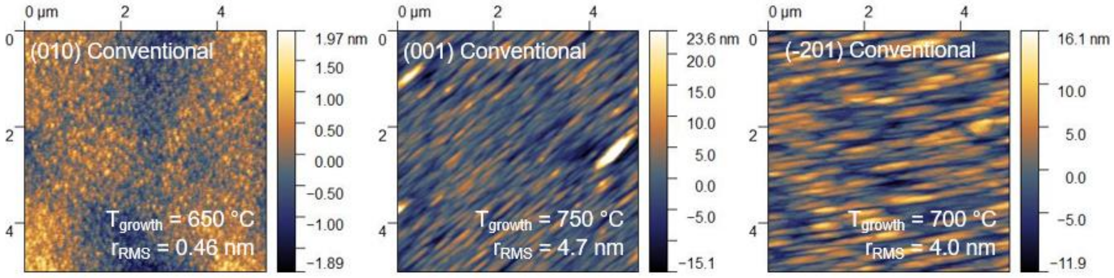

Figure 1.8: Surface morphologies of PAMBE grown β-Ga_2O_3 thin films measured via Atomic Force Microscopy for various crystallographic orientations.[10]
Reproduced from Ref. 10 with the permission from AIP Publishing.

1.7 Summary

β-Ga_2O_3's fundamental materials properties demonstrate its promise as an ultrawide bandgap semiconductor for high power switching applications. The availability of bulk substrates, heterostructure possibilities, and n-type and deep acceptor doping candidates give it the potential to realize various device designs such as SBDs, vertical FETs, and MODFETs. Epitaxial growth of β-Ga_2O_3 has been demonstrated via HVPE, MOCVD, and MBE, with MBE showing early device demonstrate and the ability to grow high quality, abrupt, controllable films. While MBE of β-Ga_2O_3 can achieve high quality (010) oriented films, other orientations suffer from suboxide desorption during growth, limiting film quality and growth rates. In Chapter 2, research on a novel growth mechanism in MBE growth called metal oxide catalyzed epitaxy (MOCATAXY) will be discussed, showing the ability to improve film quality and growth rates across various orientations. To ultimately achieve the conductive and semi-insulating regions of the device designs mentioned earlier, investigation of donor dopants and deep acceptors in MBE growth was performed and will be discussed in Chapters 3 and 4. Finally growth and characterization of β-$(Al_xGa_{1-x})_2O_3$ for heterostructures similar to those used in MODFETs will be discussed in Chapter 5.

References:

1. J. Y. Tsao, S. Chowdhury, M. A. Hollis, D. Jena, N. M. Johnson, K. A. Jones, R. J. Kaplar, S. Rajan, C. G. Van de Walle, E. Belloti, C. L. Chua, R. Collazo, M. E. Coltrin, J. A. Cooper, K. R. Evans, S. Graham, T. A. Grotjohn, E. R. Heller, M. Higashiwaki, M. S. Islam, P. W. Juodawlkis, M. A. Khan, A. D. Koehler, L. H. Leach, U. K. Mishra, R. J. Nemanich, R. C. N. Pilawa-Podgurski, J. B. Shealy, Z. Sitar, M. J. Tadger, A. F. Witulski, M. Wraback, and J. A. Simmons. Adv. Electron. Mat. **4**, 1600501 (2018).
2. M. Orita, H. Ohta, M. Hirano, and H. Hosono, App. Phys. Lett. **77** (25), 4166 (2000).
3. M. Higashiwaki, K. Sasaki, A. Kuramata, T. Masui, and S. Yamakoshi, Appl. Phys. Lett. **100**, 013504 (2012).
4. Z. Xia, H. Chandrasekar, W. Moore, C. Wang, A. J. Lee, J. McGlone, N. K. Kalarickal, A. Arehart, S. Ringel, F. Yang, and S. Rajan, Appl. Phys. Lett. **115**, 252104 (2019).
5. Y. Tomm, J. M. Ko, A. Yoshikawa, and T. Fukuda, Solar Energy Materials and Solar Cells **66** (1-4), 369 (2001).
6. A. Kuramata, K. Koshi, S. Watanabe, Y. Yamaoka, T. Masui, and S. Yamakoshi, Jpn. J. of App. Phys. **55** 1202A2 (2016).
7. K. Sasaki, M. Higashiwaki, A. Kuramata, T. Masui, and S. Yamakoshi, J. of Crystal Growth **378**, 591 (2013).
8. E. Ahmadi, O. S. Koksaldi, S. W. Kaun, Y. Oshima, D. B. Short, U. K. Mishra, and J. S. Speck, App. Phys. Exp. **10**, 041102 (2017).
9. S. H. Han, A. Mauze, E. Ahmadi, T. Mates, Y. Oshima, and J. S. Speck, Semicond. Sci. Tech. **33,** 045001 (2018).
10. A. Mauze, Y. Zhang, T. Itoh, F. Wu, and J. S. Speck, APL Materials **8**, 021104 (2020).
11. M. Baldini, M. Albrecht, A. Fielder, K. Irmscher, R. Schewski, and G. Wagner. ECS J. Solid State Sci. and Tech. **6 (**2), Q3040 (2017).
12. A. Mauze, Y. Zhang, T. Itoh, E. Ahmadi, and J. S. Speck. Appl. Phys. Lett. **117**, 222102 (2020).
13. M. H. Wong, C. H. Lin, A. Kuramata, S. Yamakoshi, H. Murakami, Y. Kumagai, and M. Higashiwaki, Appl. Phys. Lett. **113**, 102103 (2018).
14. F. Alema, Y. Zhang, A. Osinsky, N. Orischin, N. Valente, A. Mauze, and J. S. Speck, APL Materials **8**, 021110 (2020).
15. A. Mauze, Y. Zhang, T. Mates, F. Wu, and J. S. Speck, Appl. Phys. Lett. **115** (5), 052102 (2019).
16. M. Higashiwaki, A. Kuramata, M. Murakami, and Y. Kumagai. J. Phys. D.: Appl. Phys. **50,** 333002 (2017).
17. B. J. Baliga. J. Phys. D: Appl. Phys. **53**, 1759 (1982).
18. B. J. Baliga. IEEE Electron Dev. Lett. **10**, 455 (1989).
19. Y. Zhang and J. S. Speck. Semicond. Sci. Tech. **35,** 125018 (2020).

20. A. T. Neal, S. Mou, S. Rafique, H. Zhao, E. Ahmadi, J. S. Speck, K. T. Stevens, J. D. Blevins, D. B. Thomson, N. Moser, K. D. Chabak, and G. H. Jessen, Appl. Phys. Lett. **113**, 062101 (2018).
21. H. Peelaers, and C. G. Van de Walle. Phys. Status Solidi B. **252**, 4 828 (2015).
22. E. Ahmadi, O. S. Koksaldi, X. Zheng, T. Mates, Y. Oshima, U. K. Mishra, and J. S. Speck. Applied Physics Express **10**, 071101 (2017).
23. S. Krishnamoorthy, Z. Xia, C. Joishi, Y. Zhang, J. McGlone, J. M. Johnson, M. Brenner, A. R. Arehart, J. Hwang, S. Lodha, and S. Rajan. Applied Physics Letters **111** 023502 (2017).
24. T. Oshima, T. Okuno, N. Arai, N. Suzuki, S. Ohira, and S. Fujita, App. Phys. Exp. **1**, 011202 (2008).
25. Y. Zhang, A. Mauze, F. Alema, A. Osinsky, and J. S. Speck. App. Phys. Exp. **12** (4), 044005 (2019).
26. M. H. Wong, K. Goto, Y. Morikawa, A. Kuramata, S. Yamakoshi, H. Murakami, Y. Kumagai, and M. Higashiwaki. Applied Physics Express **11**, 064102 (2018).
27. Z. Hu, K. Nomoto, W. Li, L. J. Zhang, J. H. Shin, N. Tanen, T. Nakamura, D. Jena, and H. G. Xing. Proc. 75th Dev. Res. Conf. (DRC) pp. 1-2 (2017).
28. Y. Zhang, F. Alema, A. Mauze, O. S. Koksaldi, R. Miller, A. Osinsky, and J. S. Speck. APL Materials **7**, 022506 (2019).
29. H. Murakami, K. Nomura, K. Goto, K. Sasaki, K. Kawara, Q. T. Thieu, R. Togashi, Y. Kumagai, M. Higashiwaki, A. Kuramata, S. Yamakoshi, B. Monemar, and A. Koukito. Applied Physics Express **8**, 015503 (2015).
30. M.A. Liebermann and A.J. Lichtenberg. *Principles of Plasma Discharges and Materials Processing* (Wiley, New York, 2005).
31. E. Stoffels, W.W. Stoffels, D. Vender, M. Kando, G.M.W. Kroesen, and F.J. de Hoog. Phys. Rev. E. **51**, 032425 (1995).
32. M. Y. Tsai, O. Bierwagen, M. E. White, and J. S. Speck. Journal of Vacuum Science and Technology A: Vacuum, Surfaces, and Films **28**, 354 (2010).
33. Y. Oshima, E. Ahmadi, S. Kaun, F. Wu, and J. S. Speck. Semiconductor Science and Technology **33**, 015013 (2018).
34. M. E. White, M. Y. Tsai, F. Wu, and J. S. Speck. J. Vac. Sci. Tech. A: Vac. Surfaces and Films. **26,** 051300 (2008).
35. P. Vogt and O. Bierwagen. Appl. Phys. Lett. **109**, 062103 (2016).
36. P. Vogt and O. Bierwagen. Appl. Phys. Lett. **108,** 072101 (2016).
37. H. Okumura, M. Kita, K. Sasaki, A. Kuramata, M. Higashiwaki, and J. S. Speck. Appl. Phys. Exp. **7,** 095501 (2014).
38. P. Mazzolini, P. Vogt, R. Schewski, C. Wouters, M. Albrecht, and O. Bierwagen. APL Materials **7,** 022511 (2019).
39. T. Itoh, A. Mauze, Y. Zhang, and J. S. Speck. Appl. Phys. Lett. **117,** 152105 (2020).

Chapter 2: Metal Oxide Catalyzed Epitaxy of β-Ga_2O_3

2.1 Introduction

β-Ga_2O_3 PAMBE growth is limited by the active O flux that can be produced from an rf plasma source as well as the effect of Ga_2O suboxide desorption that limits growth rates at higher Ga fluxes and growth temperatures.[1-2] This desorbing suboxide readily forms in growth on cleavage planes like the (001), (100), and ($\bar{2}$01) orientations, leading to both decreased growth rates and poor film quality.[1-4] In this chapter, a catalytic growth mechanism using a supplied indium flux during PAMBE growth of β-Ga_2O_3 is demonstrated. This metal oxide catalyzed epitaxy (MOCATAXY) allows for higher growth rates, and improved material quality across various orientations.[3]

Previous studies from Vogt et al. focused on binary growth of In_2O_3 and Ga_2O_3 separately in the same oxide MBE. Using the same oxygen plasma conditions, resulting in the same atomic O flux and background molecular O_2 in the growth environment, In_2O_3 and Ga_2O_3 growth rates were compared with varying In and Ga fluxes respectively. For these experiments (111) cubic In_2O_3 and ($\bar{2}$01) β-Ga_2O_3 were grown on c-plane sapphire substrates. Growth was performed at low temperatures at which full metal incorporation was expected for O-rich growth until the stoichiometric point. In_2O_3 was shown to have approximately three times the maximum growth rate of Ga_2O_3 at its stoichiometric point (corresponding to three times the metal incorporation). This was attributed to a higher oxidation efficiency for In_2O_3 than Ga_2O_3, which could also be due to In_2O_3 accessing more oxygen in the growth environment.[5]

As described in Chapter 1, β-Ga_2O_3 is expected to grow from the atomic O flux produced via the rf plasma source and does not grow in the absence of this atomic O.[6-7] It could be the case that In_2O_3 is able to access some of the O_2 in the growth environment, resulting in an effectively higher oxygen flux, and therefore higher maximum growth rates. In addition to comparing growth rates at varying metal fluxes, Vogt et al. performed a growth temperature series for growth of both binaries on c-plane sapphire. Ga_2O_3 growth rate significantly decreased at higher growth temperatures due to Ga_2O suboxide desorption, with minimal growth at temperatures higher than 800 °C. In_2O_3 however demonstrated near maximum growth rates for temperatures up to 900 °C before In_2O suboxide desorption limited growth rates.[5]

In growth studies with both supplied In and Ga fluxes Vogt et al. observed desorbing fluxes of elements and compounds coming from the substrate in the MBE environment via quadrupole mass spectrometry (QMS). At high growth temperatures and Ga fluxes at which Ga_2O_3 does not grow, the desorbing Ga_2O suboxide was measured corresponding to the supplied Ga flux. When an In flux was added to the Ga flux at these same growth conditions, a desorbing In flux was measured corresponding to the full supplied In flux, suggesting no incorporation into the film. Additionally, the measured desorbing Ga_2O flux decreased, suggesting more Ga was incorporating into the film. X-ray diffraction confirmed the growth of ε-phase Ga_2O_3 on c-plane sapphire at growth conditions for which no Ga_2O_3 was observed in the absence of the In flux. The application of a similar catalytic effect to homoepitaxial growth of β-Ga_2O_3 on various orientations will be discussed in this chapter.[8] Much of the data and figures in this chapter are reproduced from Mauze et al.[3] with the permission of AIP Publishing.

2.2 Metal Oxide Catalyzed Epitaxy of (010) β-Ga_2O_3

Conventional PAMBE growth of (010) β-Ga_2O_3, without a suppled In flux, is limited to growth temperatures of 500 °C to 700 °C for high quality films. Maximum growth rates at these conditions range from 2-3 nm/min for the rf plasma conditions used in these studies, with typical a Ga flux of 0.8×10^{-7} to 1.0×10^{-7} torr corresponding to growth near stoichiometry in the Plateau regime. At growth temperatures greater than 800 °C, little to no growth is observed and even etching occurs at sufficiently high Ga fluxes for (010) β-Ga_2O_3.

To first study the nature of β-Ga_2O_3 growth with a supplied In flux, films were grown on thin (010) β-$(Al_xGa_{1-x})_2O_3$ spacers to spatially separate them from the β-Ga_2O_3 substrate. This structure allows for thickness, and therefore growth rates, to be measured from fringe spacing in 2θ-ω HRXRD scans of the high quality, coherently diffracting films grown on these spacers. Films were also Sn doped to produce Hall structures for transport studies to be discussed in detail in Chapter 3. Prior to growth, both Ga and O polishing was performed at 800 °C, similar to the in-situ cleaning process used prior to conventional PAMBE growth.

A Ga flux of 9×10^{-8} torr and an In flux of 1.0×10^{-7} torr were used for growth at a temperature of 900 °C, conditions for which no growth would be observed in the absence of an In flux (conventional PAMBE). The HRXRD 2θ-ω profile is shown in blue in Fig.

2.1, with the high intensity (020) β-Ga_2O_3 substrate peak and the lower intensity spread out peak at lower 2θ values indicative of a $(In_xGa_{1-x})_2O_3$ layer, with a larger out of plane lattice spacing. For successive growths, similar structures were grown with higher Ga fluxes. At a Ga flux of 1.5×10^{-7} torr, In incorporation into the $(In_xGa_{1-x})_2O_3$ layer is suppressed, as indicated by the shifting of the $(In_xGa_{1-x})_2O_3$ peak to higher 2θ values in the orange profile in Fig 2.1.

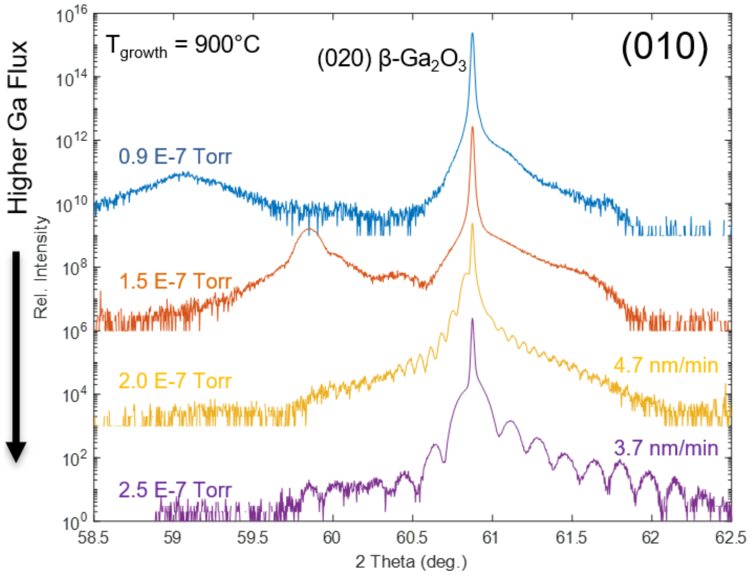

Figure 2.1: HRXRD 2θ-ω scans of the (020) β-Ga_2O_3 peaks for films grown with a constant In flux of 10^{-7} torr and varying Ga fluxes.[3]

At sufficiently high Ga fluxes, In incorporation was nearly completely suppressed and no $(In_xGa_{1-x})_2O_3$ peak is observed in HRXRD. Pendellösung fringes can be seen in this yellow HRXRD scan, indicative of a high quality coherently grown β-Ga_2O_3 at a Ga flux of 2.0×10^{-7} torr. Thickness can be calculated from the fringe spacing to determine a growth rate of 4.7 nm/min, about twice that of the maximum conventional PAMBE growth rate for (010) β-Ga_2O_3. For an even higher Ga flux of 2.5×10^{-7} torr, growth rate decreased to

3.7 nm/min, showing that at sufficiently high Ga fluxes, suboxide desorption can further decrease growth rates.

Additionally, the effect of growth temperature on suppression of In incorporation can be seen by the HRXRD profile in Fig. 2.2 for a Ga flux of 1.5×10^{-7} torr, by the shifting of the $(In_xGa_{1-x})_2O_3$ peak to higher 2θ values as growth temperature increases to 950 °C. For a higher Ga flux of 2.0×10^{-7} torr with the same In flux, the growth rate of (010) β-Ga_2O_3 decreased from 4.7 nm/min at 900 °C to 3.9 nm/min at 950 °C as shown in Fig. 2.3. This demonstrated the decrease in growth rates due to increased suboxide desorption at higher temperatures, however these growth temperatures are still much higher than those that can be used for (010) β-Ga_2O_3 PAMBE growth in the absence of an In flux. Figure 2.4 shows the AFM surface morphologies of an $(In_xGa_{1-x})_2O_3$ film grown with the suppression of facets and increased roughness when In is incorporated into the film. (010) β-Ga_2O_3 growth at sufficiently high Ga fluxes with this supplied In flux, on the other hand, demonstrated surface morphologies with grooves revealing the (110) facets, consistent with conventional PAMBE growth.

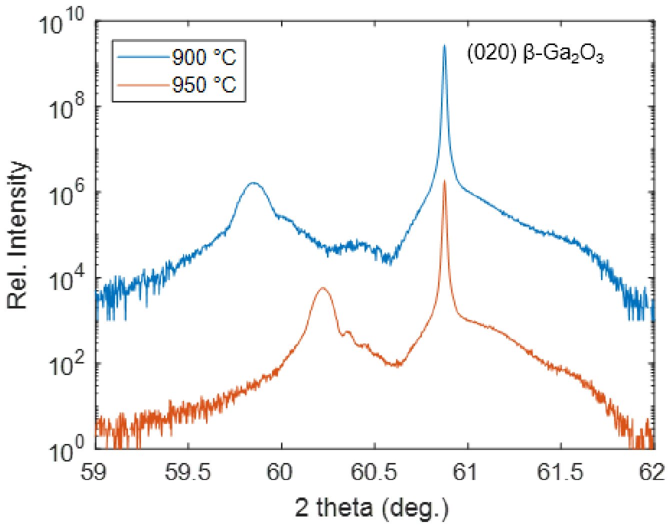

Figure 2.2: HRXRD 2θ-ω scans showing suppressed In incorporation into the film at higher growth temperatures for constant In and Ga fluxes.

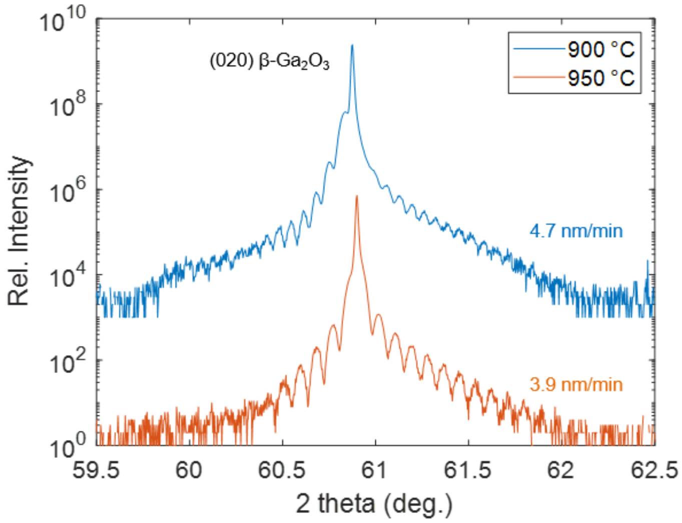

Figure 2.3: HRXRD 2θ-ω scans showing lower growth rate at higher MOCATAXY growth temperatures for (010) β-Ga_2O_3.

The ability to grow (010) β-Ga_2O_3 at higher maximum growth rates and temperatures in the presence of an In flux suggests that this In allows for more oxygen to be accessed in the growth environment, similar to the case of In_2O_3 growth in comparison to Ga_2O_3.[9-10] While the exact interaction of this indium flux with the surface of the film is difficult to characterize directly, it could form an indium or indium oxide catalyst layer at the surface of the film. This layer could play a role in interacting with the supplied oxygen flux as well as suppressing the Ga_2O suboxide desorption. Ga then exchanges with In at surface, to incorporate into the film. Ga preferentially incorporates over In due to the stronger Ga-O bond. At sufficiently high Ga fluxes (~2.0×10^{-7} torr or higher), In incorporation into the film was almost completely suppressed, despite the relatively high In flux (1.0×10^{-7} torr). Even at higher In fluxes of 6.0×10^{-7} torr for similar Ga flux, no In incorporation was observed via either an $(In_xGa_{1-x})_2O_3$ peak in HRXRD or the different surface morphology of $(In_xGa_{1-x})_2O_3$ seen in AFM in Fig. 2.4.

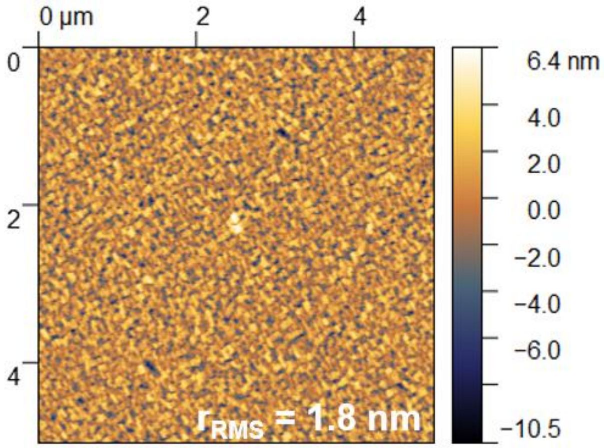

Fig 2.4: AFM Surface morphology of (010) β-$(In_xGa_{1-x})_2O_3$ film showing suppression of faceting for films with In incorporation.

Fig. 2.5 shows a schematic of the potential role of this catalyst layer at the surface of the film during MOCATAXY (010) β-Ga_2O_3. Both the molecular O_2 and atomic O species in the MOCATAXY growth environment can be seen, along with the incident and desorbing In flux that contributes to the catalyst layer but does not incorporate into the film. Wang et al. studied the formation energies of various configurations of (010) β-Ga_2O_3 surfaces with both In and Ga present. A co-adsorbed surface with both In and Ga adatoms present was found to have the lowest formation energy, suggesting this could comprise of the adlayer at the surface of the film during MOCATAXY growth, however kinetic considerations and growth conditions may play also play a role in this surface layer. Wang et al. also predicted that the presence of this co-adsorbed adlayer allows Ga atoms to adsorb more strongly to the β-Ga_2O_3 surface. Additionally, the presence of In on this surface was shown to suppress suboxide desorption, consistent with our MOCATAXY growth studies.[11]

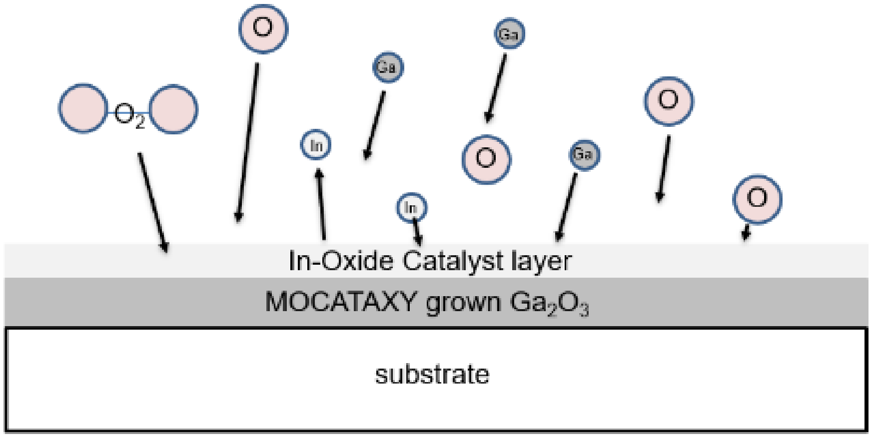

Figure 2.5: Schematic show impinging fluxes and potential catalyst layer on surface of film during MOCATAXY growth.

2.3 Metal Oxide Catalyzed Epitaxy on Various Orientations of β-Ga_2O_3

The benefits of MOCATAXY growth demonstrated for (010) β-Ga_2O_3 would be particularly promising if applied to the cleavage plane orientations of β-Ga_2O_3. As mentioned in Chapter 1, the (001), (100), and ($\bar{2}$01) orientations in the [010] zone have substrates that are more easily scalable via melt growth techniques. These orientations suffer from increased suboxide desorption limiting growth rates and material quality, making (010) β-Ga_2O_3 the optimal orientation for conventional PAMBE growth.

Initial attempts to grow β-Ga_2O_3 on scalable orientations were performed for the (001) and ($\bar{2}$01) β-Ga_2O_3. Film structures similar to those grown for the (010) growth rate studies were used for (001) and ($\bar{2}$01) studies, with unintentionally doped (UID) films grown followed by a β-$(Al_xGa_{1-x})_2O_3$ spacer layer, and a β-Ga_2O_3 layer on top. First a series was grown on (001) substrates at a growth temperature of 800 °C, an In flux of 4×10^{-7} torr, and varying Ga fluxes similar to the series used for Fig. 2.1. Films were also Sn doped to produce Hall structures for transport measurements to be discussed in Chapter 3.

Figure 2.6 shows the HRXRD 2θ-ω scans for the MOCATAXY (001) β-Ga_2O_3 growth series with varying Ga flux. At a lower Ga flux of 1.0×10^{-7} torr, some In incorporated into the film as demonstrated by the spread out $(In_xGa_{1-x})_2O_3$ peak in the blue profile. At a higher Ga flux of 1.5×10^{-7} torr, the $(In_xGa_{1-x})_2O_3$ peak shifted to higher 2θ values, indicative of smaller out of plane spacing of the layer due to less In incorporation. For higher Ga fluxes, no $(In_xGa_{1-x})_2O_3$ peak was observed in HRXRD, and thickness fringes indicative of an even thickness, high quality film were seen. For a Ga flux of 2.5×10^{-7} torr, a maximum growth rate of 5.0 nm/min was achieved. This growth rate is more than 5 times that of conventional (001) PAMBE growth (without In) and is similar to the maximum growth rate of (010) via MOCATAXY. At a higher Ga flux of 3.8×10^{-7} torr, growth rate decreased to 3.8 nm/min, again likely due to increase suboxide desorption at excess Ga fluxes.

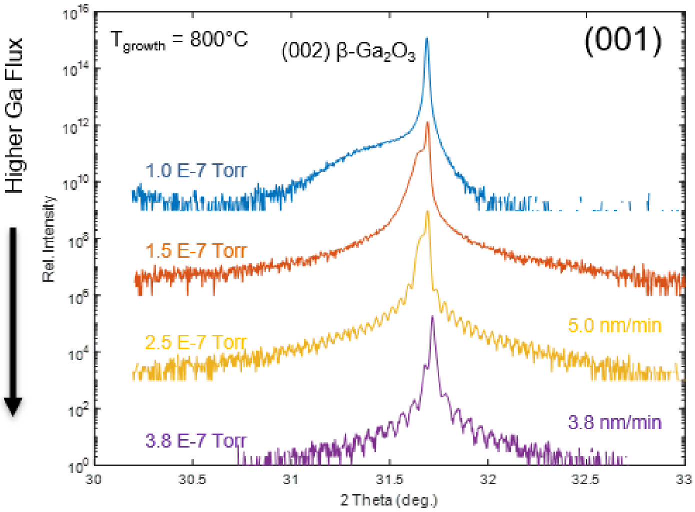

Figure 2.6: HRXRD 2θ-ω scans of the (002) β-Ga_2O_3 peaks for films grown with a constant In flux of 10^{-7} torr and varying Ga fluxes.[3]

This markedly improved growth rate at high growth temperatures and Ga fluxes suggests that MOCATAXY growth on the (001) orientation is not as limited by the heavy suboxide desorption as conventional PAMBE. Interestingly, while maximum growth rate on the (001) and (010) differ significantly for conventional PAMBE, they converge to the same rate for MOCATAXY growth. Similar structures were also grown on the ($\bar{2}01$) orientated growth, however no $(In_xGa_{1-x})_2O_3$ or thickness fringes were observed in HRXRD, so similar growth rate effects or In incorporation could not be confirmed via this technique, however further characterization confirming a similar growth rate of Sn doped

($\bar{2}01$) films to the (001) and (010) MOCATAXY growth via SIMS will be discussed in Chapter 3.

A comparison of MOCATAXY and conventional PAMBE growth rates across various orientations for different growth temperatures at the same O plasma conditions is shown in Fig. 2.7. Film structures were the same as those used for Figs. 2.1 and 2.6. Maximum conventional PAMBE growth rates are shown by the red data points, with (010) growth achieving a maximum growth rate of 2.4 nm/min at temperatures of 500 to 650 °C, before dropping at higher temperatures. Maximum ($\bar{2}01$) and (001) conventional PAMBE growth rates are also shown to be less than 1 nm/min for a range of 700 to 800 °C. Maximum growth rates were achieved at Ga fluxes near stoichiometry, the transition between O-rich and Plateau regime growth.

MOCATAXY growth rates are shown in blue in Fig 2.7, with the dark blue data points corresponding to the similar growth rates between (001) and (010) β-Ga_2O_3 films for a Ga flux of 2.5×10^{-7} torr. Growth rates of around 5 nm/min were achievable at this Ga flux for growth temperatures up to 800 °C, with growth rates dropping at higher growth temperatures due to increased suboxide desorption. At these higher temperatures, suboxide desorption could be limited by using lower Ga fluxes, as demonstrated by the light blue data points, which show the ability to still achieve a growth rate of 4.9 nm/min at 900 °C.

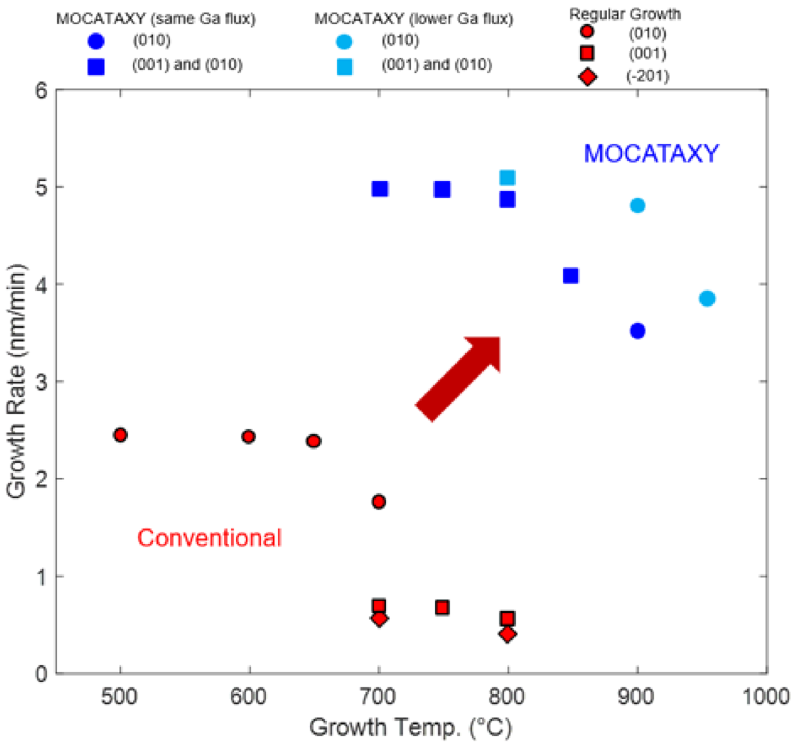

Figure 2.7: Maximum growth rates achieved via conventional PAMBE and MOCATAXY growth across various orientations.[3]

Optimal growth conditions for β-Ga_2O_3 growth with the highest growth rates and smoothest surface morphologies across orientations used an In flux of 4.0×10^{-7} torr and Ga fluxes sufficient to suppress In incorporation while not too high to lead to reduced growth rates. Growth temperatures of 700 to 800 °C were ideal for smooth morphologies and high electron mobility, which will be discussed in Chapter 3.

A comparison for AFM surface morphologies for various orientations for both conventional PAMBE and MOCATAXY growth is shown in Fig. 2.8. Similar surface features with grooves revealing facets were observed for both growth mechanisms, however smoother surface morphologies were demonstrated via MOCATAXY growth. Smooth surfaces with root mean squared roughness less than 0.5 nm were typical of optimized (010) β-Ga_2O_3 across both growth mechanisms. Grooves orientation along the [001] direction revealing the (110) and $(1\bar{1}0)$ facets were shown in the (010) β-Ga_2O_3 surface morphologies.[6] (001) β-Ga_2O_3 showed significantly improved surface morphologies, with root mean squared (RMS) roughness of 4.7 nm and 0.47 nm for conventional PAMBE and MOCATAXY growth respectively. Grooves oriented along the [010] direction were observed for both growth mechanisms for (001) β-Ga_2O_3 growth. Similarly, grooves for $(\bar{2}01)$ growth were oriented along the [010] direction. Smooth morphologies were not achieved in this orientation, with RMS roughness of 3.3 nm for the best MOCATAXY growth conditions.

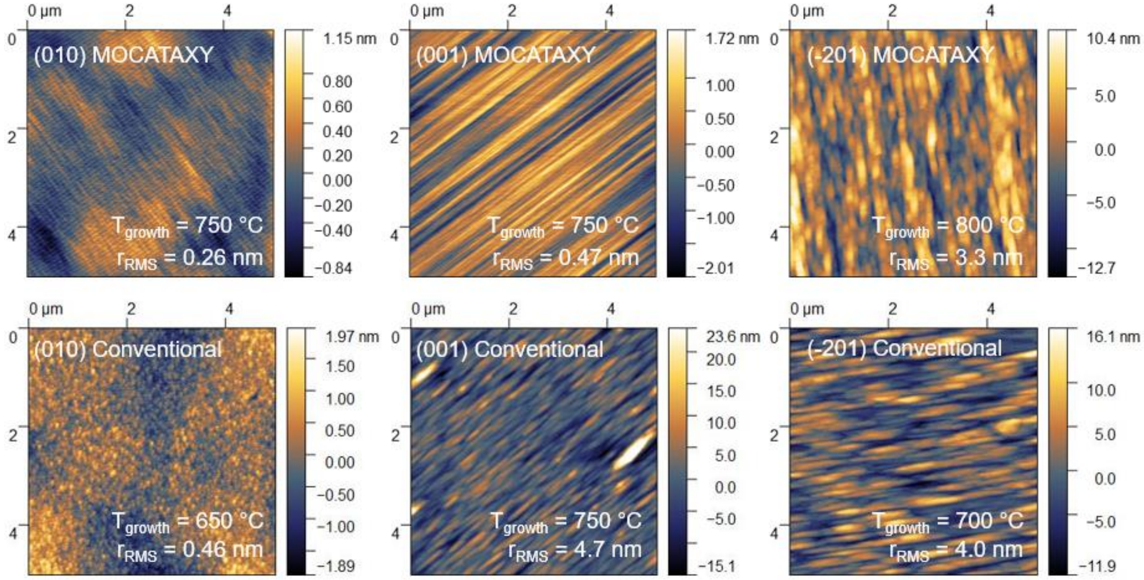

Figure 2.8: AFM surface morphologies for β-Ga_2O_3 films grown via MOCATAXY and conventional PAMBE across various orientations.[3]

To further characterize the crystal quality of the (001) and $(\bar{2}01)$ films grown via MOCATAXY, cross-sectional TEM was performed as shown in Fig. 2.9. These structures show a ~300 nm UID β-Ga_2O_3 / 10 nm β-$(Al_xGa_{1-x})_2O_3$/ 200 nm Sn doped β-Ga_2O_3 film stack. In the case of the (001) film, minimal no defects were observed in the UID film, and one extended defect was seen in the Sn doped layer, that appears to initiate at the β-(Al$_x$Ga$_{1-x}$)$_2$O$_3$ spacer. The ($\bar{2}$01) film structures show a high density of extended defects initiating at the β-(Al$_x$Ga$_{1-x}$)$_2$O$_3$ spacer as well. This could be the cause for the lack of thickness fringes seen in HRXRD of these ($\bar{2}$01) structures. The thickness of the ($\bar{2}$01) Sn doped film was similar to that of the (001) film for identical growth conditions, suggesting similar growth rates in this orientation for MOCATAXY growth. Still, improving the crystal quality of films in this orientation is necessary if it is to be used for devices structures grown by MBE.

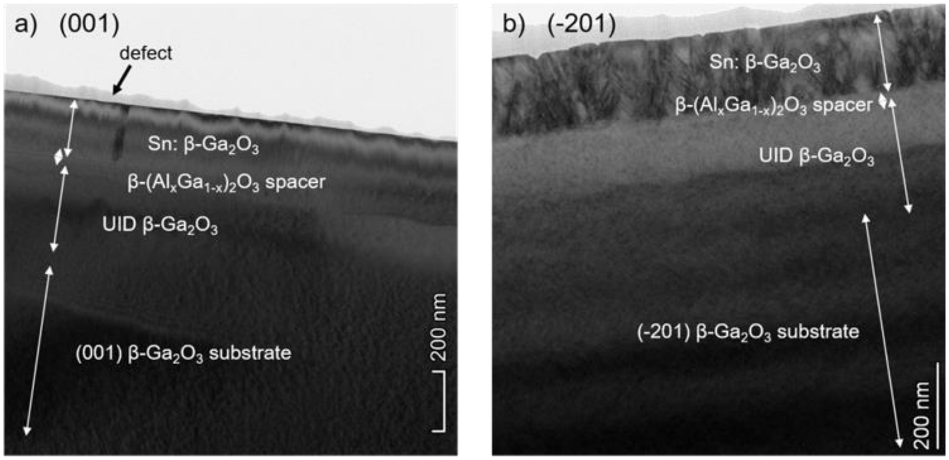

Figure 2.9: Cross section TEM of MOCATAXY grown β-Ga$_2$O$_3$ film stack structure on (001) (a) and ($\bar{2}$01) orientated substrates (b).[3]

2.4 Summary

PAMBE growth of β-Ga$_2$O$_3$ with a supplied In flux showed the potential to markedly expand the growth window to higher growth temperatures and growth rates across various crystallographic orientations. The In flux was shown to incorporate into the film at lower Ga fluxes, producing $(In_xGa_{1-x})_2O_3$ films, while higher Ga fluxes suppressed In incorporation yielding smooth, high quality β-Ga_2O_3 films in the (001) and (010) orientations. The fact that this supplied In flux allowed for β-Ga_2O_3 growth to access more oxygen in the growth environment and limit the suboxide desorption, despite the In not incorporating into the film, suggests this In acts as a catalyst for β-Ga_2O_3 growth. This metal oxide catalyzed epitaxy in the (001) orientation in particular showed a 5x improvement in growth rate and much smoother surface morphologies in MOCATAXY growth than conventional PAMBE.[3]

To apply MOCATAXY to growth of different devices structures in β-Ga_2O_3, realization of doping, high electron mobility, and heterostructures are necessary. The following chapters will investigate the nature of dopants, electron transport, and growth of the β-$(Al_xGa_{1-x})_2O_3$ / β-Ga_2O_3 heterostructure. Further characterization of MOCATAXY growth on (010) and (001) β-Ga_2O_3 in these chapters will show promise for application to device structures in these orientations.

References:

1. Y. Oshima, E. Ahmadi, S. Kaun, F. Wu, and J. S. Speck. Semiconductor Science and Technology **33**, 015013 (2018).
2. M. Y. Tsai, O. Bierwagen, M. E. White, and J. S. Speck. Journal of Vacuum Science and Technology A: Vacuum, Surfaces, and Films **28**, 354 (2010).
3. A. Mauze, Y. Zhang, T. Itoh, F. Wu, and J. S. Speck, APL Materials **8**, 021104 (2020).
4. K. Sasaki, M. Higashiwaki, A. Kuramata, T. Masui, and S. Yamakoshi, Journal of Crystal Growth **378**, 591 (2013).
5. P. Vogt and O. Bierwagen. Applied Physics Letters **108**, 072101 (2016).
6. M.A. Liebermann and A.J. Lichtenberg. *Principles of Plasma Discharges and Materials Processing* (Wiley, New York, 2005).
7. E. Stoffels, W.W. Stoffels, D. Vender, M. Kando, G.M.W. Kroesen, and F.J. de Hoog. Phys. Rev. E. **51**, 032425 (1995).
8. P. Vogt, O. Brandt, H. Riechert, J. Lähnemann, and O. Bierwagen. Phys. Rev. Lett. **119**, 196001 (2017).
9. P. Mazzolini, P. Vogt, R. Schewski, C. Wouters, M. Albrecht, and O. Bierwagen. APL Materials **7,** 022511 (2019).
10. P. Vogt, A. Mauze, F. Wu, B. Bonef, and J. S. Speck. Applied Physics Express **11**, 115503 (2018).
11. M. Wang, S. Mu, and C. G. Van de Walle. Phys. Rev. B. **102**, 035303 (2020).

Chapter 3: Donor Doping of β-Ga_2O_3

3.1 Introduction

The ability to dope a semiconductor is an important feature for its viability in switching devices. In particular, unipolar electron device applications for β-Ga_2O_3 require donor doping for conductive regions of the film. As mentioned in the Chapter 1, device structures ultimately determine the requirements of the films, like the donor concentrations, electron mobility, and doping profiles required. The device structures in Fig. 1.4 show examples of lateral and vertical device structures that could be used for β-Ga_2O_3 switching.[1-4] The lateral structure shows both heavily donor doped contacts and a delta doped thin β-$(Al_xGa_{1-x})_2O_3$ layer in the modulation doped field effect transistor.[1-3] The vertical field effect transistor also shows heavily doped contacts for both the film and substrate, as well as a thick n- drift region.[4]

To achieve these various regions of devices, an ideal donor would be able to achieve a wide range of doping concentrations controllably. For donor doped contacts, reaching high donor concentrations, without significantly degrading crystal quality or reducing mobility to the point where the contacts layers become non-conductive, is desired. For the n-drift region, maximum mobility, with the ability to achieve low donor and net carrier concentration is desired. Additionally, a shallow dopant with a high ionization efficiency is desirable for minimum R_{on} while maximizing the breakdown voltage in these structures. Furthermore, the ability to achieve low background doping and minimal compensation allows for these low doping concentrations to be produced controllably and allows for maximum electron mobility. For modulation doped field effect transistors (MODFETs), a sharp, heavily doped β-$(Al_xGa_{1-x})_2O_3$ film is needed to produce donors that contribute to the 2DEG channel. Again, high ionization efficiency and shallow donor doping is ideal for these devices.[5]

For all doping applications, controllable profiles with minimal surface riding or diffusion of the dopants should be achievable. In the case of surface riding, dopants at the surface of the film do not incorporate entirely into the atomic layer of the film being grown, leading to these dopants remaining on the surface of the film during growth and sometimes slowly incorporating into the film even after the intentional dopant flux is removed. Diffusion, on the other hand, can lead to the dopant incorporating into other layers of the film structure or substrate at high temperatures either during growth or during post-growth processes. These phenomena lead to unintentional donor incorporation into critical regions of the device, which can reduce device efficiency. Increased excess donor concentration in the drift region would limit the depletion width in the off state of the device, thereby limiting the voltage held before breakdown. Additionally, unintentional donor incorporation into acceptor doped current blocking layers in vertical structures could lead to off state leakage or poor switching performance. In lateral structures, unintentional donor incorporation into the UID film could result in a parasitic channel making it difficult to turn off the device, limiting switching performance. Additionally, excess ionized donors in the 2DEG region would increase ionized impurity scattering and reduce electron mobility.

Finally, the features and requirements of the growth technique also impact the viability of a donor doping candidate. In the case of oxide MBE of β-Ga_2O_3, source material that is compatible with the oxygen containing growth environment is necessary. The availability of a metal source that can produce fluxes of dopant atoms that can be controlled through variation in source temperature is ideal for a dopant candidate in MBE. Metal sources can oxidize over time, limiting the longevity of growth campaigns if completely oxidized charge does not produce a flux that can contribute to doping. Gas sources could also be used, provided they can also contribute to controllable and variable dopant incorporation into the films. For both types of source material, high purity of sources is necessary to avoid introduction of unintentional defects or dopants into the films. Finally, as the growth conditions required for a given device structure may vary, an ideal dopant would be controllable over a wide variety of concentrations for a range of growth temperatures and Ga/O flux ratios. Some of the doping studies and figures presented in this chapter are reproduced from Mauze et al.[6] and Mauze et al.[7] with permission of AIP publishing. Conventional PAMBE (001) β-Ga_2O_3 Sn and Ge doping figures are reproduced from Han et al.[8]

3.2 (010) Ge vs. Sn Doping via Conventional PAMBE

Early attempts to dope (010) β-Ga_2O_3 with Ge across a range of PAMBE growth conditions were performed by Ahmadi et al.[9] For a growth temperature of 650 °C, at stoichiometric growth conditions, the dependence of Ge concentration on cell temperature was measured. While Ge incorporation into the film increased for increasing Ge cell temperature from 500 to 650 °C, it saturated at a Ge concentration of 3×10^{18} cm^{-3} for a range of 650 to 800 °C, and demonstrated decreased incorporation at a higher Ge cell temperatures. This decrease in Ge incorporation at higher Ge fluxes was attributed to a Ge suboxide desorption.

Sn is also a donor dopant with a metal source that can be used in MBE. At similar growth conditions, variation of Sn cell temperatures up to 600 °C allowed Sn concentrations up to 2×10^{20} cm^{-3}, demonstrating an advantage over Ge for reaching high doping concentrations at conventional PAMBE growth conditions with a growth temperature of 650 °C and Ga flux near stoichiometry (10^{-7} torr). Figure 3.1 shows the Sn doping concentrations that can be reached through variation of the Sn cell temperature.[7]

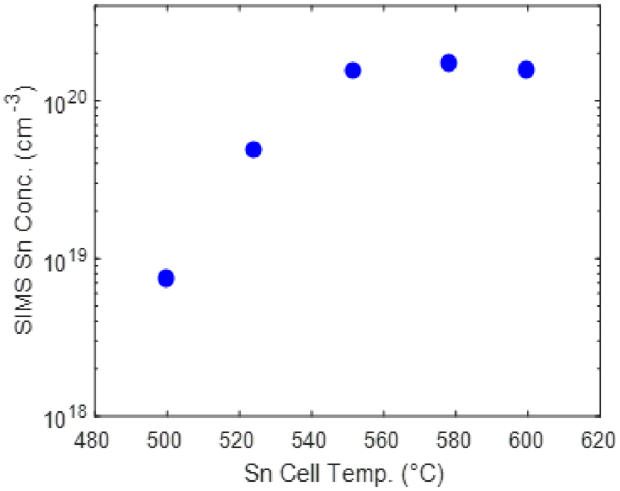

Figure 3.1: Sn doping concentration measured by SIMS vs. Sn cell temperature for conventional (010) β-Ga_2O_3 growth.[6]

To investigate the dependence of growth conditions on Sn incorporation, growth temperature was varied from 600 to 700 °C for a constant Sn cell temperature of 550 °C. Figure 3.2a shows the relatively constant Sn incorporation for this range of growth temperatures.[6] For comparison, Ge incorporation across this range from Ahmadi et al. is also shown in Fig. 3.2a, which shows a significant decrease in Ge incorporation at higher growth temperatures.[9] This limits high doping for Ge to lower growth temperatures. In addition, for the same dopant cell temperature and the same O Plasma conditions, and therefore active O flux, Ga flux was varied across a range from 2×10^{-8} torr to 2.2×10^{-7} torr. Figure 3.2b shows the resulting Sn incorporation into (010) β-Ga_2O_3 for these varying Ga/O flux ratios, demonstrating no significant change with increase Ga flux. For comparison, Ge doping from Ahmadi et al. is also shown, with Ge incorporation significantly suppressed at higher Ga/O flux ratios, particularly as Ga flux increased from the O-rich to Plateau regime growth. This could be indicative of Ga outcompeting Ge for the group III sites. While high doping concentrations are difficult to achieve for Ge at higher growth temperatures and Ga/O flux ratios, Sn doping is less dependent on growth conditions, allowing its incorporation to be controlled by dopant cell temperature for this higher doping range.[6,9]

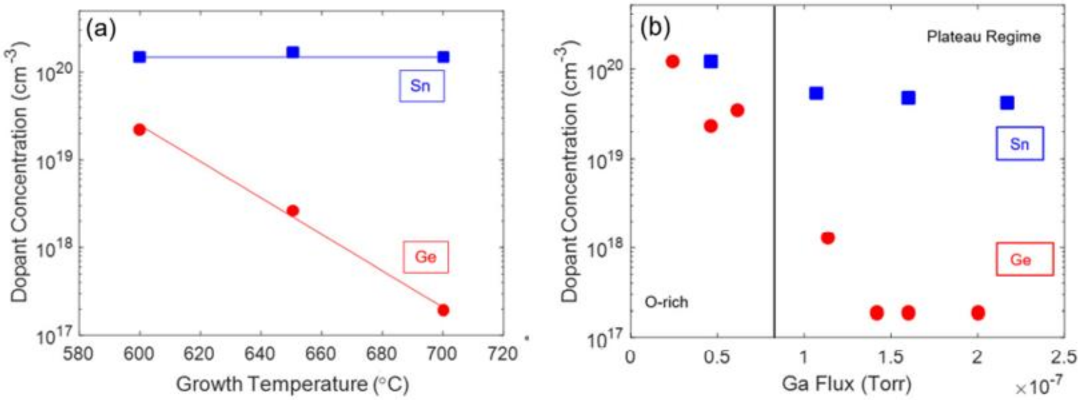

Figure 3.2: Sn doping dependence on growth temperature (a) and Ga flux (b) for a constant cell temperature for (010) β-Ga_2O_3 grown via conventional PAMBE.[6] Ge doping data from Ahmadi et al. is also shown for comparison.[9]

Consistently achieving lower Sn doping concentrations in (010) β-Ga_2O_3 via conventional PAMBE is more difficult. To investigate, the nature of doping at these lower concentrations, a SIMS stack structure was grown with Sn doped layers separated by unintentionally doped (UID) layers. Sn cell temperature for these Sn doped layers varied from 470 to 510 °C in steps of 10 °C. The SIMS profile for this structure is shown in Fig. 3.3. For higher cell temperatures, near the film surface, the doping profile was relatively flat when the Sn shutter was open, with a sharp turn on in the profile, relative to the doping concentration, after the shutter was opened and sharp turn off after the shutter was closed. At the lower Sn cell temperatures required to achieve lower doping concentrations, the Sn profiles measured by SIMS were not constant for a constant cell temperature, and did not resemble an ideal top hat profile. When the shutter was open, a significant doping delay was observed with Sn concentration rising gradually throughout the intentionally doped layer. Furthermore, after the shutter was closed, Sn continued to incorporate in the film, as indicated by the tail in the Sn profile from the Sn doped layer into the subsequently grown UID layer. This doping delay and surface segregation effect, rather than sharp turn on and turn off of the Sn profiles, limits the ability to control Sn concentration for the lower doping range. The physical origin of these effects is a still a topic of ongoing study, however it could be related to the oxidized nature of the Sn source material, and the resulting Sn and SnO fluxes coming from the cell, or it could be linked to the surface coverage of Sn containing species at the surface of the film during growth. Lamoreaux et al. demonstrated a high SnO flux during vaporization of Sn-SnO_2 mixtures.[10] Hoffman et al. showed the high SnO fluxes from SnO_2 and Sn-SnO_2 mixture PAMBE sources in-situ via quadrupole mass-spectroscopy.[11] While our source material is Sn, oxidation after exposure to the oxygen containing growth environment is possible.

Ahmadi et al. showed much sharper turn on and off for doping profiles with Ge doping in (010) β-Ga2O3 as well as the ability to controllably achieve lower doping concentrations, suggesting an advantage for Ge doping in this range for the (010) orientation via conventional PAMBE.[9]

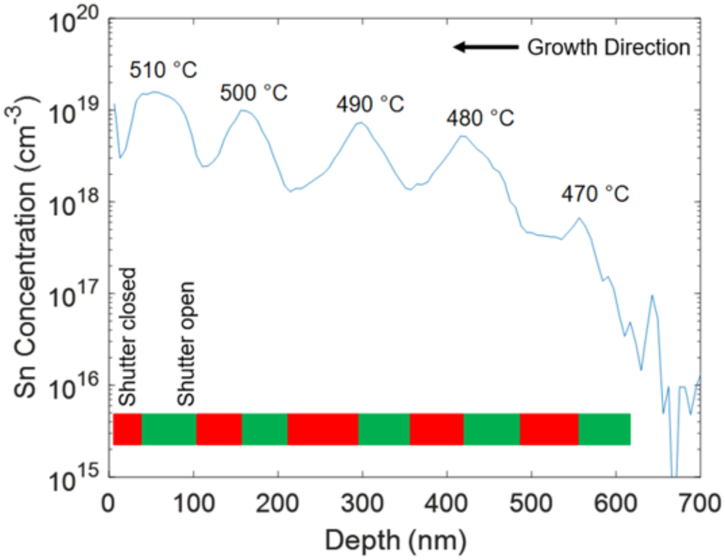

Figure 3.3: SIMS Sn doping profiles for Sn doped layers with various Sn cell temperatures separated by unintentionally doped spacers.[6]

To further investigate donor doping with Sn, room temperature Hall measurements were performed on 100-300 nm Sn doped films grown on a 200 nm UID buffer layer on Fe doped semi-insulating substrates with Ti/Au contacts deposited in the corners of 5×5 mm^2 samples. Figure 3.4 shows the measured Hall carrier concentration and mobility for films grown with Sn cell temperatures ranging from 500 to 650 °C. Maximum carrier concentration achieved was around 10^{20} cm^{-3} at a cell temperature of 550 °C. Additionally, the increase in carrier concentration from 3×10^{17} cm^{-3} to 10^{19} cm^{-3} for a variation in cell temperature of just 25 °C, shows further difficulty in controlling Sn doping for the lower concentration range. The maximum mobility achieved was 100 cm^2/Vs for the film with a carrier concentration of 3×10^{17} cm^{-3}, which is similar to that achieved by Ahmadi et al. for Ge doping of (010) β-Ga_2O_3 via conventional PAMBE.[9]

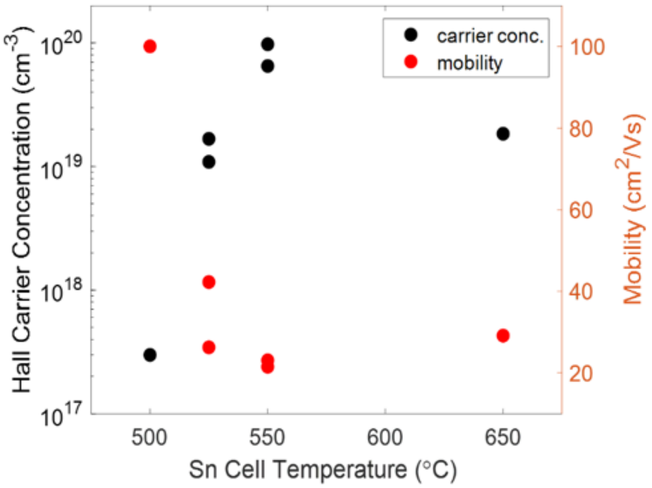

Figure 3.4: Room Temperature Hall carrier concentration and mobility for films grown with varying Sn cell temperatures.[6]

3.3 (001) Ge vs. Sn Doping via Conventional PAMBE

Donor doping of (001) β-Ga_2O_3 grown via conventional PAMBE was also investigated using both Ge and Sn.[7-8] For these studies, a Ga flux of 3.3×10^{-8} torr was used for growth near the transition between O-rich and Plateau regime growth. These growth conditions typically corresponded to a growth rate of about 1 nm/min.[12] First, a comparison of Ge and Sn doping for constant cell temperatures (800 and 560 °C respectively) was performed across the typical growth temperature range of (001) β-Ga_2O_3 growth (675 to 800 °C). Figure 3.5 shows this data, revealing that Sn incorporation depended little on growth temperature in this range, while Ge incorporation was significantly suppressed at higher growth temperatures. These trends are similar to those observed for (010) oriented growth.

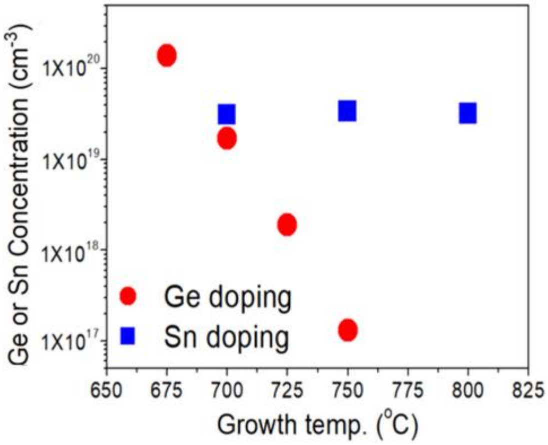

Figure 3.5: Ge and Sn doping concentration dependence on growth temperature for constant cell temperatures for (001) β-Ga_2O_3 conventional PAMBE growth.[8]

Next, the dependence of Ge and Sn incorporation on cell temperature was investigated for (001) β-Ga_2O_3. Figure 3.6a shows an Arrhenius plot of Ge concentration for varying cell temperatures. Growth temperatures of 675 °C and 750 °C were investigated, with Ge incorporating more at lower growth temperatures for all cell temperatures. At lower cell temperatures, an Arrhenius relationship is observed between Ge cell temperature and Ge concentration in the films with an apparent activation energy of 2.3 eV. This is similar to the activation energy calculated for the relationship between Ge temperature and vapor pressure, suggesting incorporation is proportional to flux for this range of cell temperatures.[13] At higher cell temperatures, the slope of this relationship significantly decreases, suggesting surface reactions limit further incorporation. The maximum Ge incorporation also shows dependence on growth temperature, with a lower growth temperature of 675 °C allowing for higher Ge incorporation up to 10^{20} cm^{-3}, and a higher growth temperature of 750 °C resulting in Ge incorporation less than 3×10^{18} cm^{-3}, limiting higher Ge doping applications to the lower growth temperatures.

Figure 3.6b shows the Arrhenius relationship between Sn doping concentration and cell temperature, yielding an apparent activation energy of 2.9 eV, similar to that of liquid Sn vaporization.[14] Sn concentrations ranging from 4×10^{17} cm^{-3} to 10^{21} cm^{-3} were achievable through variation of cell temperature at a growth temperature of 750 °C.

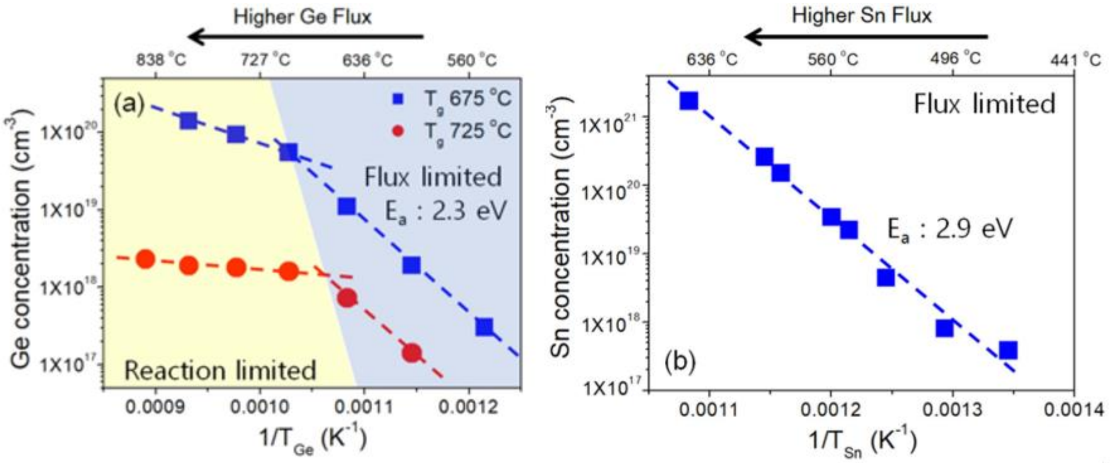

Figure 3.6: Dopant incorporation dependence on cell temperature for Ge (a) and Sn (b) doping in (001) β-Ga_2O_3 conventional PAMBE growth.[8]

As mentioned in Chapter 1, the higher growth temperatures in this range yield smoother surface morphologies for (001) growth. This is re-iterated in Fig. 3.7 which shows the surface morphologies for a Ge doped film grown at 675 °C, along with a Sn doped film grown at 750 °C. Grooves oriented along the [010] direction were observed in both surface morphologies, similar to UID (001) films, however the RMS roughness was 6.0 nm for the 675 °C film and 2.0 nm for the 750 °C film.

SIMS measurements of the Ge doped and Sn doped layers were performed to determine whether sharp doping profiles could be obtained. Figure 3.8a shows the Ge doping profile of a sample grown at 675 °C, demonstrating a significant delay in turn on of the Ge doping profile for (001) β-Ga_2O_3. This effect was not observed by Ahmadi et al. for (010) growth, suggesting the nature of Ge incorporation is different across these different orientations.[9] The Sn doped profile shown in Fig. 3.8b for (001) β-Ga_2O_3 does not demonstrate a significant delay for a similar dopant concentration, also suggesting a difference in the nature of dopant incorporation between Sn and Ge.

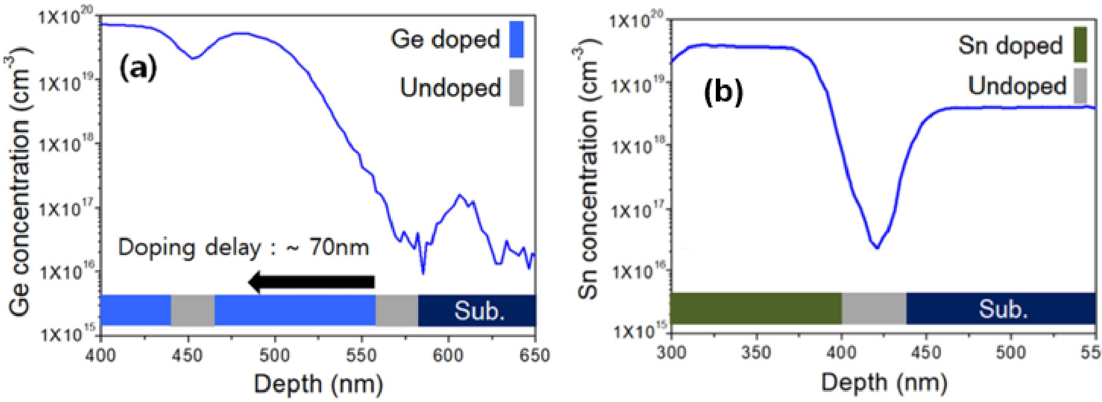

Figure 3.8: Ge and Sn doping profiles measured by SIMS for (001) β-Ga_2O_3 films demonstrating doping delay for Ge doping (a) and sharper turn on profile for Sn doping (b).[8]

To further investigate the doping delay, a lower temperature growth with high Ge incorporation was performed and the SIMS profile is shown in Fig. 3.9a. The film structure consisted of a 220 nm Ge doped layer on top of a UID layer all grown at a growth temperature of 650 °C. This lower growth temperature corresponds to both a rougher surface morphology and higher Ge incorporation and does not result in a significant delay. One mechanism for this delay could be that Ge requires sufficient Ge surface coverage before incorporation, that could build up faster at the lower growth temperatures due to limited Ge suboxide desorption. Ge could also have difficulty incorporating into the (001) plane, however other facets that appear during rougher growth could more readily incorporate Ge. This would be consistent with the fact that no doping delay is observed in (010) growth, and the fact that lower temperature, rougher (001) growth seems to show less of a doping delay.

To test this, two Ge doped films were grown at identical growth conditions with a growth temperature of 675 °C and a Ge cell temperature of 700 °C, one on top of a rougher UID 100 nm layer and one on top of a smooth 100 nm UID layer. The smooth UID layer was grown at 750 °C and the rougher layer was grown at 675 °C. The SIMS profiles are show in Fig. 3.9b, demonstrating a larger doping delay for the Ge doped film grown on a smoother layer than the one grown on a rougher layer. This further suggested that the roughness of the (001) film, and therefore the other facets present in the (001) β-Ga_2O_3, contributes to Ge incorporation. This nature of Ge doping delay is unideal for achieving both smooth surfaces and controllable Ge doping profiles.

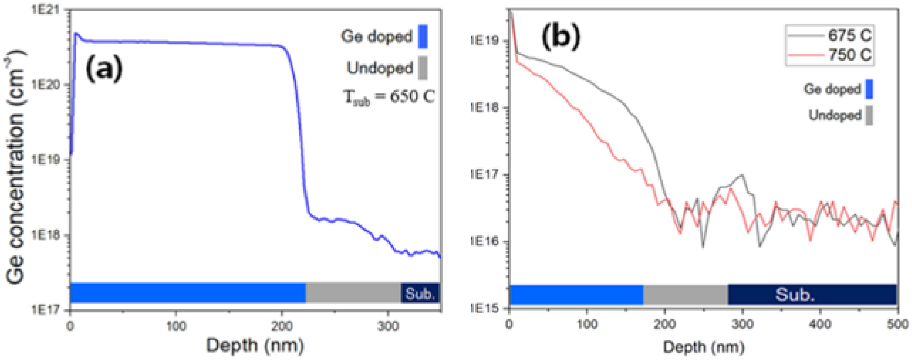

Figure 3.9: Ge doping profile in Ge doped (001) β-Ga_2O_3 film grown at 650 °C (a) and Ge doping profiles for Ge doped (001) β-Ga_2O_3 films grown at 675 °C on unintentionally doped buffers grown at various temperatures (b).[8]

Finally, analysis of the electronic quality of (001) β-Ga_2O_3 was performed via room temperature Hall measurements in the van der Pauw geometry. Films with ~300 nm doped layers were grown on Fe doped substrates and In dot contacts were placed in the corners of the 5×5 mm^2 samples. Table 3.1 shows a summary of the measured Hall carrier concentrations and mobility for various Sn and Ge doped samples. Hall mobilities in the range of 20 to 26 cm^2/Vs were typical for carrier concentrations around 10^{18} cm^{-3}, which is much lower than (010) films.[10] The highest room temperature mobility for conventional PAMBE growth of (001) β-Ga_2O_3 was 39 cm^2/Vs at a carrier concentration of 3.0×10^{17} cm^{-3}, while (010) β-Ga_2O_3 demonstrated a mobility of 100 cm^2/Vs for the same carrier concentration, showing another advantage of the (010) growth over (001) β-Ga_2O_3.[7]

Table 3.1: Comparison of various Hall carrier concentrations and mobilities for Ge and Sn doped (001) β-Ga_2O_3 grown via conventional PAMBE.[7-8]

Dopant	Ge	Ge	Ge	Sn	Sn
Growth Temperature (°C)	650	675	675	750	750
Carrier Conc. (cm^{-3})	9.5×10^{18}	4.3×10^{18}	6.7×10^{17}	1.1×10^{18}	3.0×10^{17}
Mobility (cm^2/Vs)	21.0	20.3	26.3	25.3	39.0

Both Ge and Sn doping over a range of concentrations were realized for (001) β-Ga_2O_3 grown via conventional PAMBE. Ge doping demonstrated a significant delay in incorporation and a growth temperature dependent incorporation, limiting high doping at the higher growth temperatures. Sn doping revealed sharper profiles than Ge, as well the ability to n-type dope at the higher growth temperature of 750 °C, at which surface morphologies are significantly smoother. For both Ge and Sn doping, Hall mobilities were significantly lower in (001) β-Ga_2O_3 than those measured for similar carrier concentrations for (010) β-Ga_2O_3. Both the surface morphology and electron mobility of PAMBE grown (001) β-Ga_2O_3 films need significant improvement for the eventual realization of (001) β-Ga_2O_3 based devices.

3.4 MOCATAXY (010) Sn Doping

In Chapter 2, the growth of β-Ga_2O_3 via metal oxide catalyzed epitaxy (MOCATAXY) was discussed, showing markedly improved growth rates and film quality. This use of an In flux during PAMBE growth particularly allows for improved surface morphologies and structural quality of (010) and (001) oriented β-Ga_2O_3 films, while expanding growth conditions to higher temperatures and Ga fluxes, at which almost no In incorporates into the films. Because of the limitations of Ge doping at higher Ga fluxes and growth temperatures for conventional PAMBE mentioned earlier in this chapter, Sn was chosen as the dopant of choice for initial donor doping of β-Ga_2O_3 grown via MOCATAXY.

To first investigate the nature of Sn doping in MOCATAXY grown (010) β-Ga_2O_3, a SIMS stack was grown with Sn doped layers separated by UID spacers layers. Optimal growth conditions for surface morphology and highest growth rates of (010) β-Ga_2O_3, with a temperature of 800 °C, Ga flux of 2.5×10^{-7} torr, and In flux of 4×10^{-7} torr were used. Sn cell temperatures were varied from 600 to 900 °C for the doping profile shown in Fig. 3.10a. A range of Sn concentrations from 10^{16} cm^{-3} to 4×10^{18} cm^{-3} were obtained for these cell temperatures, despite using significantly higher cell temperatures than those used to achieve >10^{20} cm^{-3} in conventional PAMBE doping. Additionally, the doping profiles for the Sn doped layers grown by MOCATAXY were significantly sharper than those achieved by conventional PAMBE. Ideal top hat profiles were obtained with a constant Sn doping level when the shutter was open and almost no incorporation after the Sn shutter was closed, leading to no clear surface segregation or doping delay effects.

The controllable profiles and higher range of Sn cell temperatures suggest the nature and mechanism of Sn doping for MOCATAXY is different than for conventional growth. The large flux of Sn, in the form of either elemental Sn or the oxide SnO that incorporates heavily into conventional PAMBE grown films does not incorporate into the MOCATAXY grown films. This could be due to the doping species differing between growth techniques. SnO, which is expected to demonstrate higher fluxes at lower cell temperatures in an oxygen containing environment, may incorporate into the conventional PAMBE grown films and also lead to the doping delay and surface segregation observed in Sn doping profiles in Fig. 3.3. This SnO may not undergo the same metal exchange mechanism that Ga does, thus suppressing Sn incorporation from SnO into MOCATAXY grown films. At higher cell temperatures, the flux of elemental Sn increases, allowing for incorporation of Sn into the film. The difference in the effective dopant species could lead to the smooth profiles seen in MOCATAXY growth, as well as the high cell temperatures required, compared to conventional PAMBE of (010) β-Ga_2O_3.

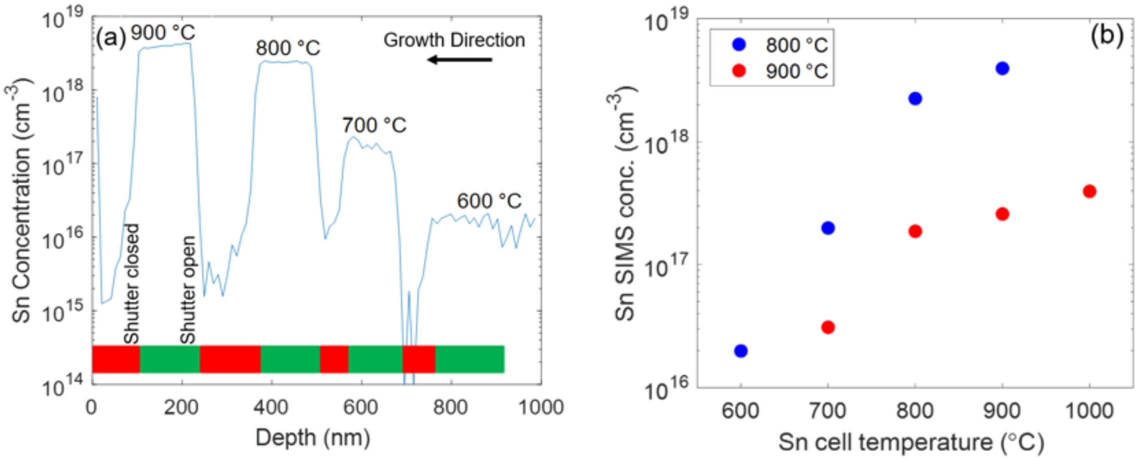

Figure 3.10: SIMS Sn doping profile for Sn doped films grown via MOCATAXY with different Sn cell temperatures separated by UID spacer layers for (010) β-Ga_2O_3 (a). Sn SIMS concentration vs. Sn cell temperature plotted for 800 °C and 900 °C growth temperatures for MOCATAXY (010) β-Ga_2O_3 growth (b).[6]

Comparison of Sn doping concentrations for various cell temperatures at growth temperatures of 800 °C and 900 °C are shown in Fig. 3.10b. Unlike in the case of conventional PAMBE, Sn doping incorporation via MOCATAXY decreased at higher growth temperatures. This further suggests a difference in the Sn incorporation mechanism between MOCATAXY and conventional PAMBE of (010) β-Ga_2O_3. Still, through variation of cell temperatures up to 1200 °C (high temperature limit of the cell used for Sn doping), and growth temperatures in the range of 700 °C to 950 °C (range of MOCATAXY growth for high quality films), Sn doping concentrations ranging from 10^{16} cm^{-3} to 3×10^{20} cm^{-3} could be achieved.

Ultimately, various carrier concentrations need to be achieved via Sn doping to fulfill the various applications within devices grown via MBE, such as n+ contacts or low doped drift regions. 200 to 300 nm thick layers were grown on 200 nm UID buffers on Fe doped substrates to characterize carrier concentration and electron mobility via Hall measurements. Figure 3.11a shows a summary of the Hall data demonstrating a range of carrier concentrations up to 2×10^{19} cm^{-3}. Figure 3.11b shows a comparison between the carrier concentrations for these films and the Sn doping concentration measured via SIMS. A consistent trend between the two was observed until very high Sn concentrations at which either incomplete ionization or compensation led to a significant drop in carrier concentration. Many films grown with Sn concentrations greater than 10^{20} cm^{-3} were not conductive in Hall measurement. For reference, a line is shown in Fig. 3.11b representing complete ionization where the donor concentration equals the SIMS Sn concentration. The consistently lower donor concentration than actual Sn concentrations suggest incomplete ionization for most films.[6]

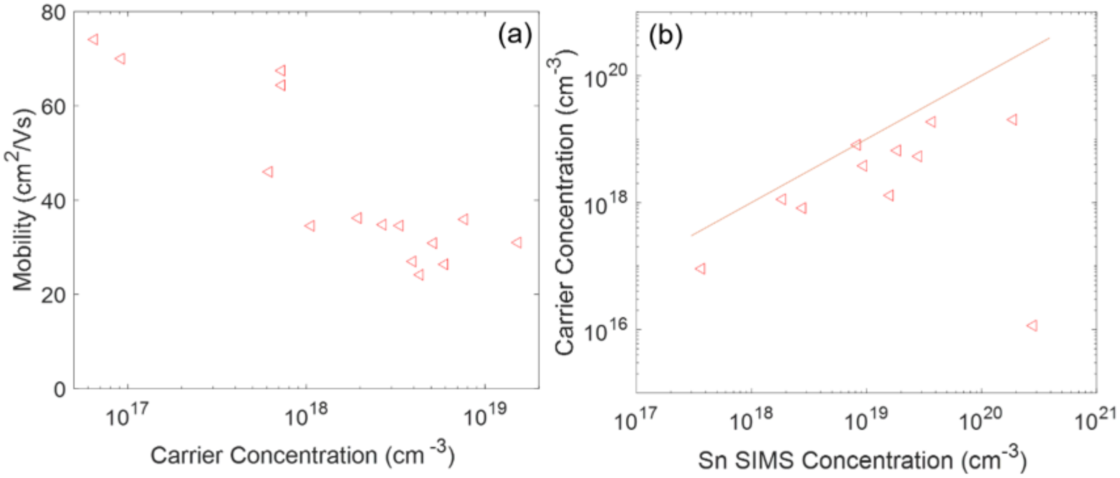

Figure 3.11: Hall carrier concentration vs. mobility for various Sn doped (010) β-Ga_2O_3 films grown via MOCATAXY (a) along with comparison of Hall carrier concentration vs. Sn concentration measured via SIMS (b).[6] A line is shown as a guide representing complete ionization of Sn dopants.

3.5 MOCATAXY (001) Sn Doping

MOCATAXY growth has shown significant improvement in surface morphology and structural quality of (001) β-Ga_2O_3, however higher electron mobility in films grown in this orientation are necessary for device applications. Conventional PAMBE has demonstrated significantly better electron mobility in (010) films than (001), leading to further motivation for investigating doping via MOCATAXY for (001) β-Ga_2O_3.

As mentioned in Chapter 2, similar growth rates for identical growth conditions were observed for the (010) and (001) orientations during Sn doped β-Ga_2O_3 growth. To characterize and compare Sn doping across orientations, (001), ($\bar{2}$01), ad (001) substrates were coloaded for MOCATAXY growth of Sn doped films separated by UID spacers for SIMS measurements. Growth temperature and Sn cell temperature varied across different layers of the stack. Figure 3.12 shows the Sn SIMS profiles for all three of these orientations, demonstrating similar trends across orientations. The profiles also confirm similar growth rates across all three orientations. Interestingly, the ($\bar{2}$01) orientation incorporated more Sn consistently for the same growth conditions for MOCATAXY growth. Relatively sharp doping profiles were observed, particularly for the (001) and (010) orientations. Additionally, the range of cell temperatures required for MOCATAXY growth of (001) was significantly higher than conventional PAMBE to achieve the same Sn doping concentrations. This further suggests the difference in the mechanism of Sn doping via MOCATAXY, potentially due to the different Sn containing species that contributes to this Sn doping.[7]

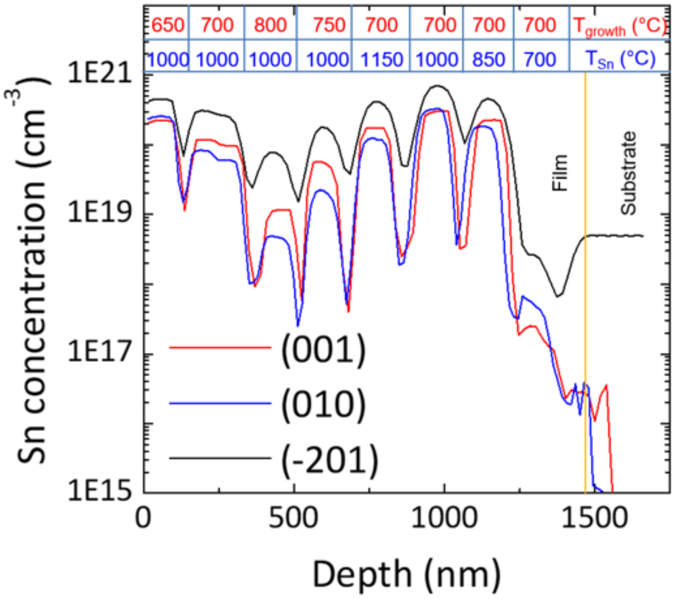

Figure 3.12: Sn doping concentration measured via SIMS for MOCATAXY grown films with Sn doped layers separated by UID spacers for different orientations.[7]

Summaries of Sn doping concentrations across orientations for constant growth temperature and constant cell temperature are shown in Fig. 3.13a and 3.13b respectively. For a growth temperature of 700 °C, the lowest growth temperature for which smooth surface morphologies were maintained via MOCATAXY growth, Sn concentrations up to mid-10^{20} cm^{-3} could be achieved across all orientations. For a constant Sn cell temperature of 1000 °C, increasing growth temperature from 650 to 800 °C resulted in decreased Sn incorporation across orientations. This effect of Sn incorporation dependence on growth temperature is observed for MOCATAXY growth but not conventional PAMBE for these orientations.

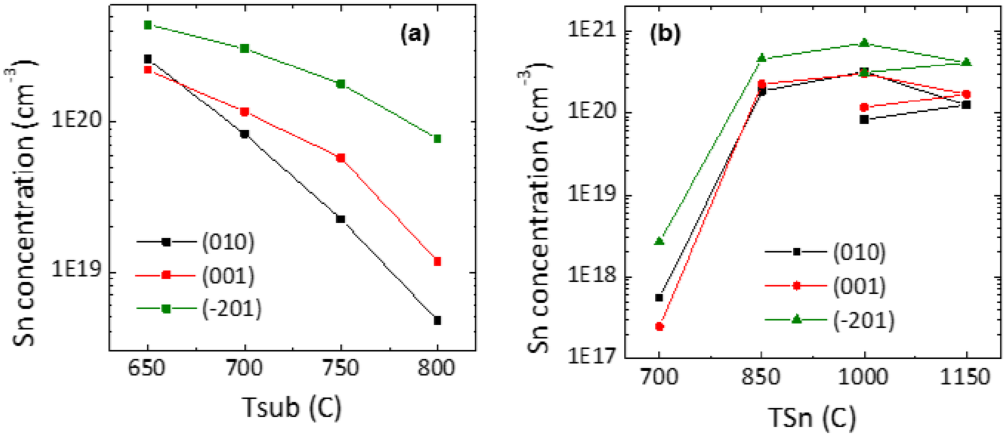

Figure 3.13: Comparison of Sn concentration vs. growth temperature (a) and vs. Sn cell temperature (b) for various growth orientations, based on growths in 3.12.

Next, 200-300 nm Sn doped films were grown on UID Buffers with a β-$(Al_xGa_{1-x})_2O_3$ spacer, so that film thicknesses could be characterized via HRXRD. These structures were used for the MOCATAXY growth rate studies discussed in Chapter 2, as well as Hall measurements. A series of films were grown on (010), (001), and ($\bar{2}01$) substrates coloaded for the same growths. Ga and In fluxes of 2.5×10^{-7} torr and 4×10^{-7} torr were used respectively with a Sn cell temperature of 750 °C. Growth temperatures for this series varied from 700 to 850 °C, with the resulting Hall carrier concentrations and mobilities shown in Fig. 3.14. All of the ($\bar{2}01$) β-Ga_2O_3 were non-conductive in Hall measurement, consistent with the poorer film quality demonstrated in growth on this orientation shown in Chapter 2.

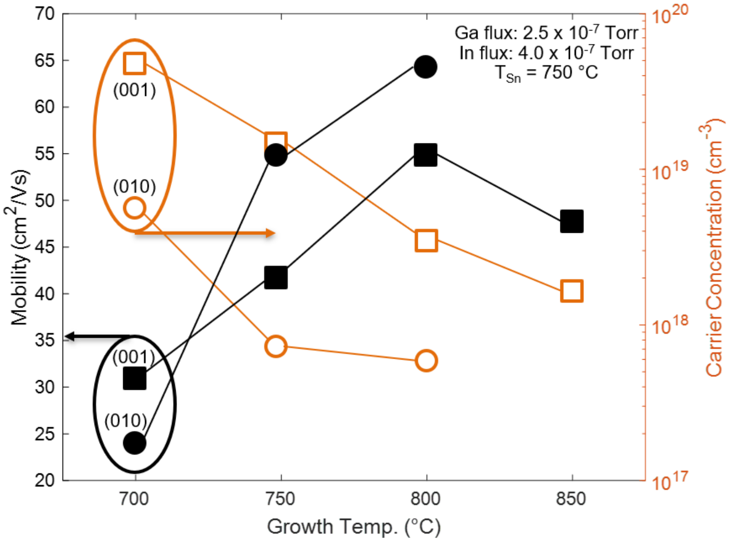

Figure 3.14: Hall carrier concentration vs. mobility for constant Sn cell temperature and various growth temperatures for MOCATAXY grown films on (001) and (010) β-Ga_2O_3.[7]

For both the (010) and (001) Sn doped films, carrier concentration decreased with higher growth temperatures, consistent with the trends seen from the SIMS results in Fig. 3.13b. Furthermore, carrier concentration measured in the (001) films were higher than the (010) films for the same growth conditions, consistent with the trend in Fig. 3.13a showing higher Sn incorporation into (001) films. Hall mobilities for the (001) orientated films were similar to those for the same carrier concentrations in the (010) orientation. Maximum Hall mobility in this series was 55 cm^2/Vs at a carrier concentration around 3×10^{18} cm^{-3}, which was significantly higher than the Hall mobility around 20-30 cm^2/Vs for similar concentrations for (001) conventional PAMBE growth. Additionally, maximum Hall mobility for growth via MOCATAXY for a similar thickness Sn doped (001) β-Ga_2O_3 film with a carrier concentration of 7.2×10^{17} cm^{-3} was 65 cm^2/Vs.

3.6 Si Doping

In addition to Sn doping, Si doping via MOCATAXY growth has been investigated. Kalarickal et al. investigated δ-doping of (010) β-Ga_2O_3 grown via conventional PAMBE and noticed that the Si source oxidized rapidly in the oxide MBE environment, limiting the ability to produce continuously Si doped β-Ga_2O_3. δ-doping, however, could still achieve degenerately doped layers or be used to dope β-$(Al_xGa_{1-x})_2O_3$ for modulation doped heterostructures.[15]

For our studies, to first determine the Si doping dependence on Si cell temperature and valve position, a stack of Si doped layers separated by UID spacers was grown via MOCATAXY on (010) β-Ga_2O_3. A valved effusion cell from E-Science Inc. was used for Si doping. This allows for closing of a valve near the lip of the effusion cell to limit exposure of the Si the oxygen environment. Additionally, the valve can be opened to different positions to control dopant flux in conjunction with Si cell temperature. Figure 3.15 shows the Si doping profile for this stack grown on an Fe doped substrate. A spike of Si due to impurities at the film-substrate interface was observed in SIMS even after Ga and O polishing prior to growth.[2] Continuous doping with relatively flat doping profiles was realized with Si, with a sharp turn on, but some surface segregation effect seen in the 100 nm/dec turn off in the Si doping profile. The ability to control dopant flux by closing the valve position is also demonstrated by the difference in doping concentration between a valve position of 100% (fully open) and 20%.

Next films grown with varying doping concentrations were grown on β-$(Al_xGa_{1-x})_2O_3$ spacer layers on (010) β-Ga_2O_3 via both conventional PAMBE and MOCATAXY.

Figure 3.16 shows the HRXRD 2θ-ω scans for some of these films. At minimal Si doping concentrations, thickness fringes were observed, similar to UID films grown on β-$(Al_xGa_{1-x})_2O_3$ spacer layers. For higher Si doping levels no thickness fringes were seen, and a peak appeared at higher 2θ values than the (020) β-Ga_2O_3 peak. This trend is consistent for Si doping levels of 6×10^{17} cm^{-3} or higher for both MOCATAXY and conventional PAMBE growth. Surface morphologies measured via AFM are also shown in Fig. 3.16 for these films, showing significant roughening of the films at higher Si doping concentrations, suggesting that Si acts as an anti-surfactant during growth of (010) β-Ga_2O_3. Additionally, room temperature Hall measurements were performed on these samples with none demonstrating conductivity. This could be due to degradation of film quality and introduction of defects during growth of (010) β-Ga_2O_3 with a constant Si flux or due to the Si filling electrically inactive sites or self-compensating. A (010) β-Ga_2O_3 film was grown via MOCATAXY with both Sn and Si doping to better understand the nature of the Si dopants in the film. Interestingly, thickness fringes were observed in HRXRD and Hall measurement revealed a Hall mobility and carrier concentration of 71 cm^2/Vs and 2.2×10^{18} cm^{-3}. The Sn and Si doping concentrations measured via SIMS were 2.5×10^{18} cm^{-3} and 2×10^{18} cm^{-3} respectively. This could suggest that while Si may act as an anti-surfactant, Sn could act as a surfactant improving the film quality. Furthermore, because the mobility and carrier concentration were consistent with the trends of Sn doping via MOCATAXY of (010) β-Ga_2O_3, the Si may be mostly inactive electronically (un-ionized dopants). Much work including defect characterization is still needed to understand the nature of Si in the

(010) β-Ga_2O_3 films, however continuous doping with Si in MBE growth of (010) β-Ga_2O_3 seems less promising than Sn doping.

Next, Si doping of (001) β-Ga_2O_3 films grown via MOCATAXY was investigated. Film structures with Si doped layers on β-$(Al_xGa_{1-x})_2O_3$ spacers on Fe doped substrates were grown with typical HRXRD 2θ-ω scans of the films shown in Fig. 3.17. Some fringes were observed despite relatively high Si concentrations > 10^{18} cm^{-3}. Still, these fringe peaks seemed less defined than those observed for Sn doped films, already indicating a rougher or less uniform film. Surface morphology measured via AFM is shown in Fig. 3.17 as well with RMS roughness of 1.2 nm. This is rougher than the typical Sn doped (001) films grown via MOCATAXY. Hall measurement was performed on two films yielding Hall mobilities of 67 and 49 cm^2/Vs for carrier concentrations of 3×10^{18} cm^{-3} and 9×10^{18} cm^{-3} respectively. The similar Hall mobility for the same carrier concentrations as Sn doped films shows promise for continuous Si doping of (001) β-Ga_2O_3 grown via MOCATAXY. Additionally, a Si concentration of 8.3×10^{18} cm^{-3} was measured via SIMS for the film with a Hall carrier concentration of 9×10^{18} cm^{-3}, suggesting a high dopant ionization efficiency, consistent with the shallow donor level of Si demonstrated in previous studies. Ultimately, continuous Si doping of (001) β-Ga_2O_3 shows more promise than the (010) β-Ga_2O_3 after these initial studies.

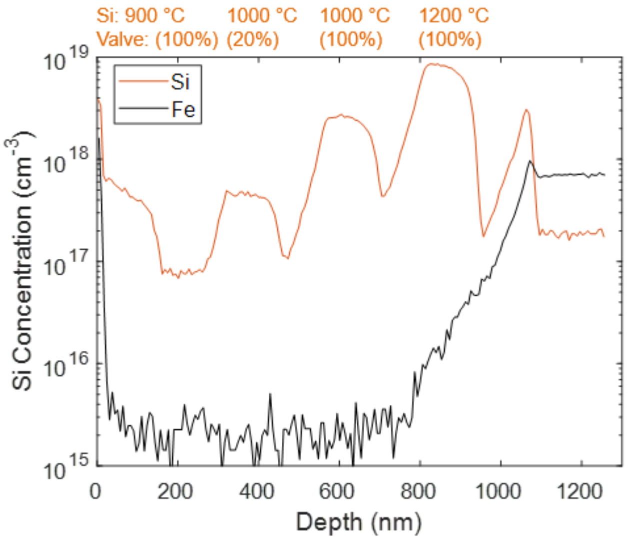

Figure 3.15: Si doping profile measured via SIMS for MOCATAXY grown (010) β-Ga_2O_3 with Si doped layers separated by UID profiles. Si cell temperature and valve position are also shown.

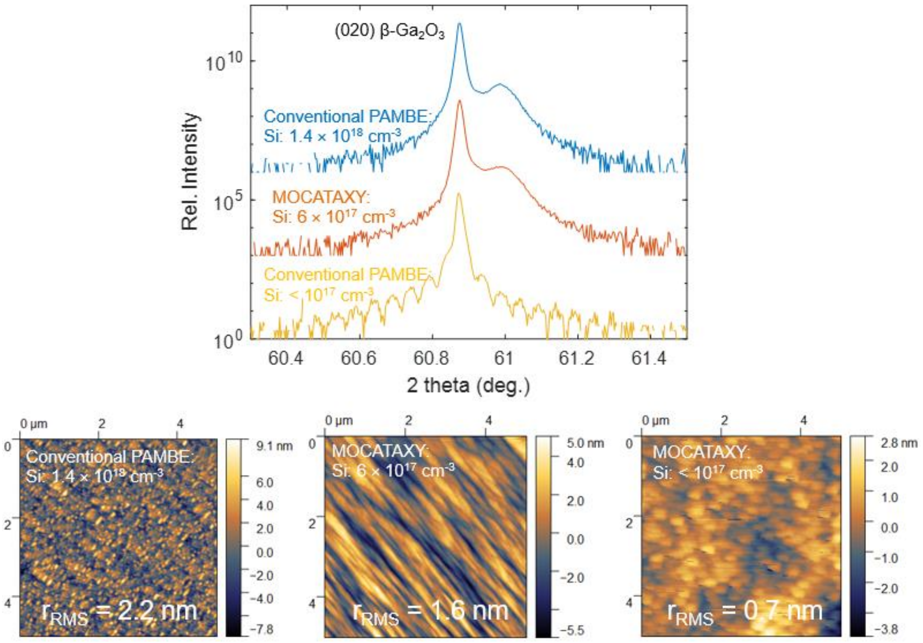

Figure 3.16: HRXRD 2θ-ω scans of Si doped (010) β-Ga_2O_3 films with varying doping concentrations grown on β-$(Al_xGa_{1-x})_2O_3$ spacers for both conventional PAMBE and MOCATAXY growth. Surface morphologies for the same films measured by AFM show the rougher films with higher Si doping.

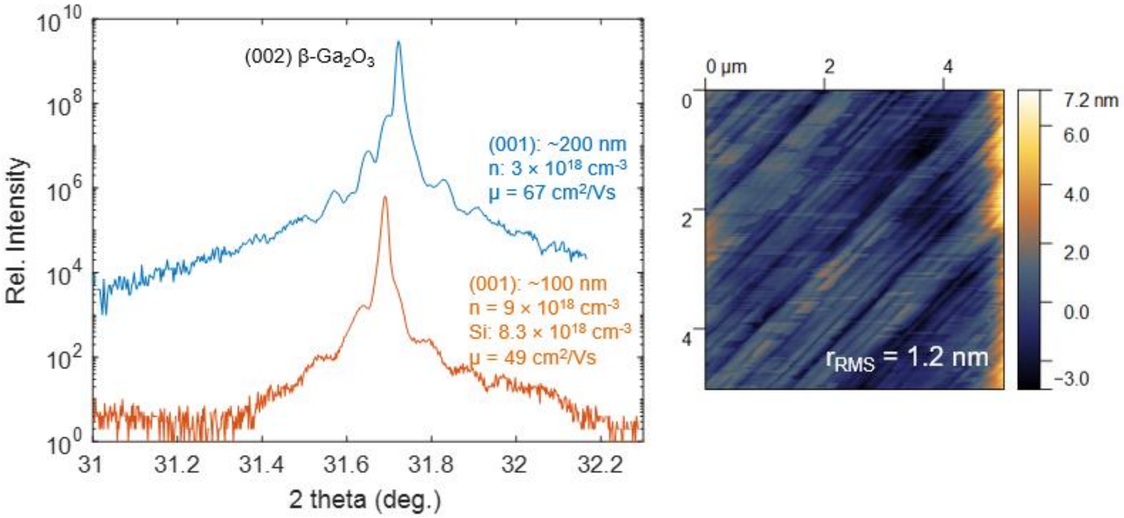

Figure 3.17: HRXRD 2θ-ω scans of Si doped (001) β-Ga_2O_3 films on β-$(Al_xGa_{1-x})_2O_3$ spacers along with surface morphology measured via AFM.

3.7 Temperature Dependent Hall Measurement

To further investigate the nature of Sn doping in the (010) β-Ga_2O_3 films, temperature dependent Hall measurement was performed on films with lower net doping concentrations. Here, two ~1 μm thick Sn doped films were grown on UID β-Ga_2O_3 buffer layers at a growth temperature of 700 °C and Sn cell temperatures of 675 °C and 625 °C. Figure 3.18 shows the surface morphology of one of these films with a total thickness of 1.6 μm. The RMS roughness is 0.12 nm for a 20×20 μm^2 area, demonstrating the ability to grow thick doped films (by MBE standards) while maintaining a smooth surface morphology. Ultimately thickness of 1 to 10 μm is necessary for high breakdown voltage applications.

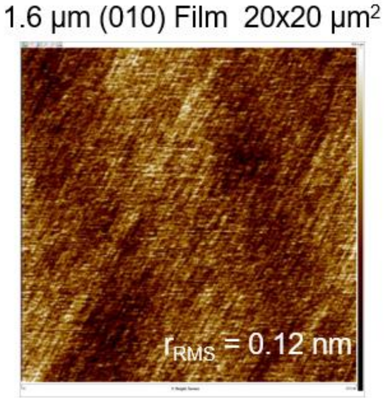

Figure 3.18: Surface morphology of 1.6µm thick (010) β-Ga_2O_3 film grown via MOCATAXY.

Room temperature Hall measurements yielded carrier concentration and mobility of 2.4×10^{17} cm^{-3} and 122 cm^2/Vs for the Sn cell temperature of 675 °C (sample A) and 3.9×10^{16} cm^{-3} and 136 cm^2/Vs for the Sn cell temperature of 625 °C (sample B). This higher room temperature mobility is the highest achieved for a continuously doped β-Ga_2O_3 film grown via MBE to our knowledge. Temperature dependent Hall measurement was performed on sample A as shown in Fig. 3.19. The mobility peaked at a value of 168 cm^2/Vs at a temperature of 165 K. This low peak mobility and the fast mobility roll-off observed at lower temperatures is a signature of strong ionized impurity scattering.

Fitting the temperature dependent carrier concentration to the charge neutrality equation shown in eqn. 3.1 with one primary donor concentration N_D and fully ionized compensating acceptors N_A can be used to extract donor concentration and donor level (E_D). Here k_B is the Boltzmann constant, T is the measurement temperature in Kelvin, E_F is the Fermi level and n is the net carrier concentration.

$$n + N_A = \frac{N_D}{1+2\exp\left(-\frac{E_D-E_F}{k_BT}\right)} \text{ (eqn. 3.1)}$$

The Fermi level can be estimated via the following equation where N_C is the conduction band density of states estimated using an electron effective mass of $0.313m_0$.[16-17]

$$n = N_C e^{\frac{-(E_C-E_F)}{k_BT}} (\text{eqn. } 3.2)$$

Fitting to the experimental data in Fig. 3.17 yields a donor level (E_D) of 77 meV and a donor concentration (N_D) of 8.2×10^{17} cm^{-3}. This corresponds to the sharp slope in the temperature dependent carrier concentration at temperatures above 100 K. The shallower slope below 100 K could be indicative of a degenerate charge at the substrate film interface, due to impurities like Si. This has been observed in previous MBE growth studies. The corresponding sheet charge at this interface would be ~9.9×10^{10} cm^{-2}. The Sn donor level is significantly deeper than those for Si and Ge.[18]

The temperature dependent mobility was fit with the polar optical phonon scattering components similar to methods from Zhang et al.[16] This was fit iteratively with the temperature dependent carrier concentration to yield a net ionized impurity concentration ($N_D^+ + N_A$) from the ionized impurity scattering component of the mobility. N_A was determined to be approximately 2.5×10^{17} cm^{-3}. This relatively high background acceptor concentration contributes to the difficulty in consistently achieving net low donor concentrations in MBE grown β-Ga_2O_3.

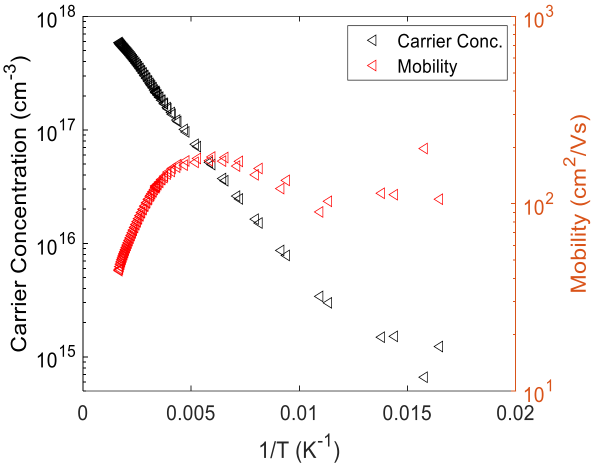

Figure 3.19: Temperature dependent Hall mobility and carrier concentration for Sn doped (010 β-Ga_2O_3 film grown via MOCATAXY (sample A).[6]

Sample B with room temperature carrier concentration of 3.9×10^{16} cm^{-3} and mobility of 136 cm^{2}/Vs showed some similar features in temperature dependent Hall. Figure 3.20 shows the temperature dependent carrier concentration and mobility for this sample. Again, significant mobility roll off at lower temperatures was observed, indicative of high ionized impurity scattering with an estimated N_A of 1.1×10^{17} cm^{-3}. A Sn donor level of 85 meV was extracted from this Hall data, again showing a deeper level than for Si or Ge. More details of the temperature dependent Hall analysis are shown in Appendix A.

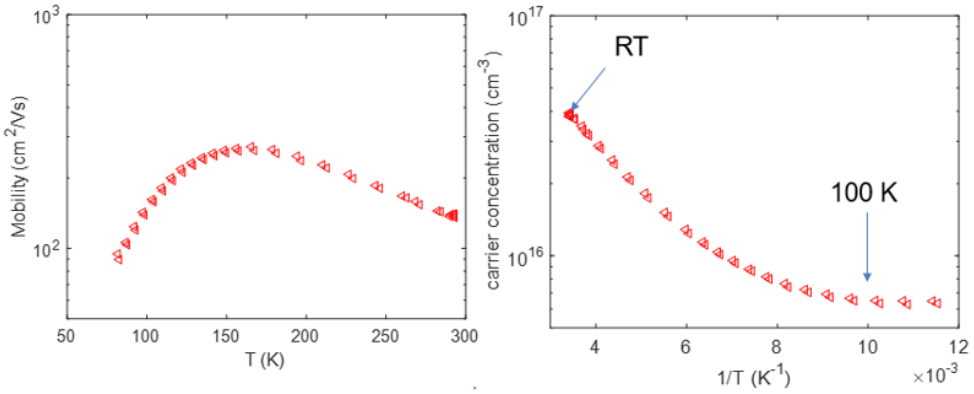

Figure 3.20: Temperature dependent Hall mobility and carrier concentration for Sn doped (010) β-Ga_2O_3 film grown via MOCATAXY (sample B).

3.8 Summary

Investigation of donor candidates in MBE growth of β-Ga_2O_3 across different orientations reveals benefits and challenges with each dopant. Ge doping showed the ability to achieve sharp doping profiles in the (010) orientation during conventional PAMBE growth, however a doping delay was observed at the onset of the intentional doping in (001) β-Ga_2O_3. Both orientations showed a wide range of concentrations achievable in conventional PAMBE, however higher growth temperatures and Ga/O flux ratios showed limited Ge incorporation.

Sn doping via conventional PAMBE showed limitations in controllably reaching lower doping concentrations due to surface segregation and a doping delay effect. Growth via metal oxide catalyzed epitaxy (MOCATAXY) allowed for a wide range of Sn concentrations with sharp doping profiles across the (010) and (001) crystallographic orientations of β-Ga_2O_3. Hall measurements revealed the ability to achieve various net carrier concentrations for applications from low doped channels and drift layers to highly doped n+ contacts. Furthermore, electron mobility in Sn doped β-Ga_2O_3 grown via MOCATAXY was the highest for a continuously doped β-Ga_2O_3 film grown via MBE. (001) β-Ga_2O_3 showed significantly improved electron mobility in MOCATAXY growth vs. conventional PAMBE, suggesting it is the preferred growth mechanism for (001) β-Ga_2O_3 devices grown via MBE. Additionally, Si doped (001) β-Ga_2O_3 showed similar electron mobility to Sn doping.

Temperature dependent Hall measurement revealed the ~80 meV donor level for Sn. It also demonstrated a significant mobility roll-off, suggesting significant ionized impurity scattering in the MBE grown films. The background acceptor concentrations were estimated to be on the order of 10^{17} cm^{-3} in these films. Further investigation into reducing this background acceptor concentration is necessary for growth of low doped, high mobility films necessary for future power electronic devices rated for high voltages.

References:

1. M. Higashiwaki, K. Sasaki, T. Kamimura, M. H. Wong, D. Krishnamurthy, A. Kuramata, T. Masui, and S. Yamakoshi. Applied Physics Letters. **103**, 123511 (2013).
2. E. Ahmadi, O. S. Koksaldi, X. Zheng, T. Mates, Y. Oshima, U. K. Mishra, and J. S. Speck. Applied Physics Express **10**, 071101 (2017).
3. S. Krishnamoorthy, Z. Xia, C. Joishi, Y. Zhang, J. McGlone, J. M. Johnson, M. Brenner, A. R. Arehart, J. Hwang, S. Lodha, and S. Rajan. Applied Physics Letters **111** 023502 (2017).
4. M. H. Wong, K. Goto, Y. Morikawa, A. Kuramata, S. Yamakoshi, H. Murakami, Y. Kumagai, and M. Higashiwaki. Applied Physics Express **11**, 064102 (2018).
5. Y. Zhang and J. S. Speck. Semicond. Sci. Tech. **35** 125018 (2020).
6. A. Mauze, Y. Zhang, T. Itoh, E. Ahmadi, and J. S. Speck. Appl. Phys. Lett. **117**, 222102 (2020).
7. A. Mauze, Y. Zhang, T. Itoh, F. Wu, and J. S. Speck, APL Materials **8**, 021104 (2020).
8. S. H. Han, A. Mauze, E. Ahmadi, T. Mates, Y. Oshima, and J. S. Speck, Semiconductor Science and Technology **33,** 045001 (2018).
9. E. Ahmadi, O. S. Koksaldi, S. W. Kaun, Y. Oshima, D. B. Short, U. K. Mishra, and J. S. Speck, Applied Physics Express **10** (4), 041102 (2017).
10. R. H. Lamoreaux and D. L. Hildenbrand. J. of Phys, and Chem. Ref. Data **16**, 419 (1987).
11. G. Hoffman, M. Budde, P. Mazzolini, and Oliver Bierwagen. APL Materials **8**, 031110 (2020).
12. Y. Oshima, E. Ahmadi, S. Kaun, F. Wu, and J. S. Speck. Semiconductor Science and Technology **33**, 015013 (2018).
13. K. Benz, E. Bauser, K. Gillessen, A. Marshall, J. Hesse, and K. Ploog. Crystals; Growth, Properties and Applications. (Berlin: Springer) (2012).
14. C. Alcock. V. P. Itkin, and M. K. Horrigan. Can. Metall. Q. **23**, 309 (1984).
15. N. K. Kalarickal, Z. Xia, J. McGlone, S. Krishnamoorthy, W. Moore, M. Brenner, A. R. Arehart, S. A. Ringel, and S. Rajan, Appl. Phys. Lett. **115**, 152106 (2019).
16. Y. Zhang, F. Alema, A. Mauze, O. S. Koksaldi, R. Miller, A. Osinsky, and J. S. Speck. APL Materials **7**, 022506 (2019).
17. Y. Zhang, A. Neal, Z. Xia, C. Joishi, J. Johnson. Y. Zheng, S. Bajaj, M. Brenner, D. Dorsey, K. Chabak, G. Jessen, J. Hwang, S. Mou, J. Heremans, and S. Rajan. Appl. Phys. Lett. **112**, 173502 (2018).
18. A. T. Neal, S. Mou, S. Rafique, H. Zhao, E. Ahmadi, J. S. Speck, K. T. Stevens, J. D. Blevins, D. B. Thomson, N. Moser, K. D. Chabak, and G. H. Jessen, Appl. Phys. Lett. **113**, 062101 (2018).

Chapter 4: Acceptors in PAMBE grown β-Ga_2O_3

4.1 Introduction

To achieve the variety of unipolar device structures for β-Ga_2O_3, controllable acceptor doping is necessary. While p-type doping in β-Ga_2O_3 hasn't been demonstrated due to negligible valence band dispersion, large acceptor ionization energies, and strong hole self-localization, deep acceptors can be used to produce semi-insulating regions of devices and substrates to create high potential barriers and current blocking layers.[1-3]

N, Mg, and Fe are acceptor dopant candidates in β-Ga_2O_3, but each has its own benefits and challenges. N as an acceptor has been used in MOCVD β-Ga_2O_3[4] and ion implantation[5] but its lack of a solid source makes it relatively unexplored in MBE. Mg has a solid source that has been used for MBE growth of materials systems like nitrides in past. Its use in intentional doping of PAMBE grown (010) β-Ga_2O_3, as well as diffusion observed after high temperature anneals are demonstrated in this chapter. Fe has been used to produce semi-insulating substrates for lateral device structures, however Fe incorporation into thin films grown on Fe doped substrates has been demonstrated across epitaxial growth techniques.[6] Analysis and quantification of this behavior will be discussed further in this chapter. The Mg doping and diffusion data and Fe incorporation data of this chapter have been reproduced from Mauze et al.[7] and Mauze et al.[8] with the permission of AIP Publishing.

4.2 Mg Doping and Diffusion

For the Mg doping and diffusion studies, all β-Ga_2O_3 films were grown on Fe doped (010) β-Ga_2O_3 bulk substrates at our conventional PAMBE growth conditions. A typical Ga flux of 0.8×10^{-7} torr to 1.1×10^{-7} torr at a growth temperature of 600 to 700 °C resulted in growth near stoichiometry (Plateau regime)[7], allowing for a maximum growth rate of 2.4 nm/min. Doping concentrations were measured via secondary ion mass spectroscopy (SIMS) using a CAMECA IMS 7f tool with the absolute Mg concentration calibrated to an implant standard.

To determine the range of Mg doping concentrations achievable in PAMBE, the Mg cell temperature was varied from 140 °C to 200 °C for typical (010) β-Ga_2O_3 growth conditions at a growth temperature of 650 °C. The relationship between Mg cell temperatures in this range and resulting doping concentrations from 2×10^{16} cm^{-3} to 8×10^{20} cm^{-3} demonstrates an Arrhenius behavior with an apparent activation energy of 3.0 eV as shown in Fig. 4.1. This wide range of Mg concentrations measured by SIMS is ideal to achieve varying compensation levels in β-Ga_2O_3. The higher range of deep acceptor doping could allow for very resistive regions of the film structures such as current blocking layers, whereas lower Mg doping has applications in further partial compensation studies with co-doping or to create n-type / acceptor doped junctions with various barrier heights.

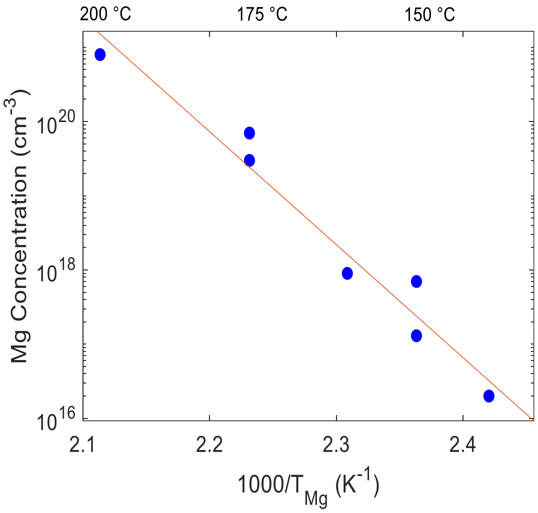

Figure 4.1: Arrhenius relationship between Mg cell temperature and doping concentration achieved in (010) β-Ga_2O_3 films.[7]

Figure 4.2 shows a SIMS depth profile of a sample grown with alternating Mg-doped and unintentionally doped (UID) β-Ga_2O_3 layers. The Mg cell temperatures were varied between Mg-doped layer, via cooling of the Mg cell while the shutter was closed, to achieve the different concentrations demonstrated. The SIMS profile reveals sharp top hat doping profiles. The turn-on and turn-off slope of 8 nm/dec and 11 nm/dec respectively demonstrate little diffusion or surface riding at these conventional PAMBE conditions. This is ideal for application to lateral structures for heavily acceptor-doped buffer films to compensate the parasitic channel at the film-substrate interface or for sharply defined current blocking layers used in vertical devices. Unintentional acceptor incorporation into active regions of devices, like channels or drift regions, can lead to unwanted compensation as well as increased ionized impurity scattering thus reducing device efficiency.[8,9]

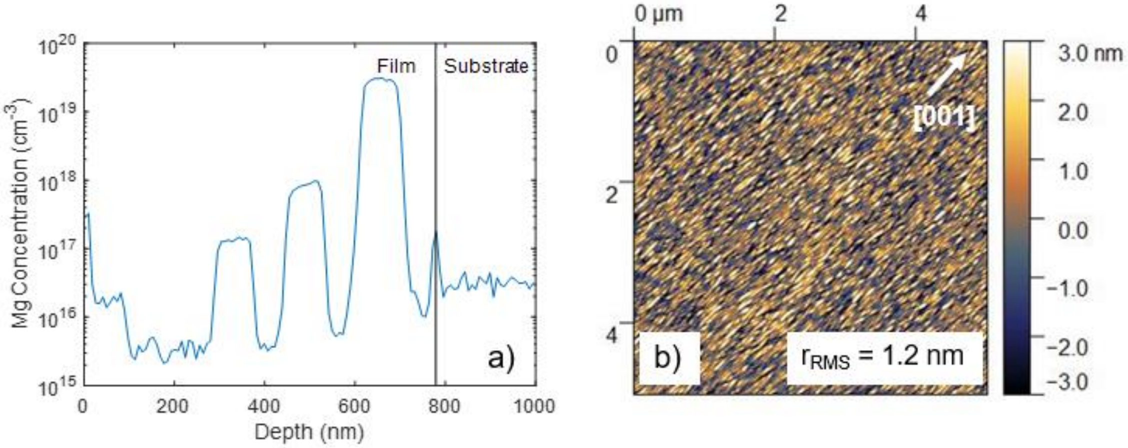

Figure 4.2: Doping profile for various Mg doped β-Ga_2O_3 layers separated by unintentionally doped spacers measured by secondary ion mass spectroscopy (a) along with surface morphology of Mg doped film measured by atomic force microscopy (b).[7]

To further investigate the dependence of Mg doping concentration on conventional PAMBE growth conditions, the growth temperature and Ga flux were varied for constant Mg cell temperatures. At a Ga flux near stoichiometry (transition from O-rich to Plateau regime) and a constant Mg cell temperature of 200 °C, the Mg doping concentration remained at 3×10^{19} cm^{-3} for growth temperatures varying from 600 °C to 700 °C. Additionally, varying the Ga flux from the O-rich growth regime (3.8×10^{-8} torr) to the more Ga-rich Plateau regime (2.0×10^{-7} torr) demonstrated minimal change in Mg incorporation. This suggests that for conventional PAMBE, consistent Mg doping can be achieved across different growth conditions, allowing for these growth conditions to be determined by the requirements of other aspects of the device structure, rather than the limitations of the acceptor dopant. For comparison, Ahmadi et al. demonstrated that Ge incorporation in PAMBE decreased significantly at higher growth temperatures and Ga fluxes.[10] Both Ge and Mg doping dependence on growth conditions is shown in Fig. 4.3 for comparison. Sn doping, on the other hand, has shown similar behavior to Mg, with minimal dependence on growth temperature or Ga/O flux ratio in conventional PAMBE.[11-12]

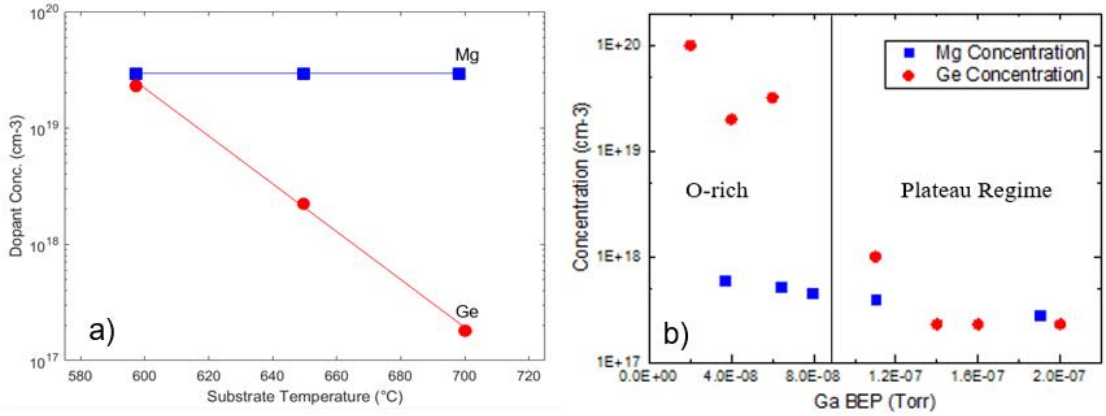

Figure 4.3: Mg doping dependence on growth temperature (a) and Ga flux measured by beam equivalent pressure (BEP) (b) with Ge data from Ahmadi et al. shown for comparison.[7,10]

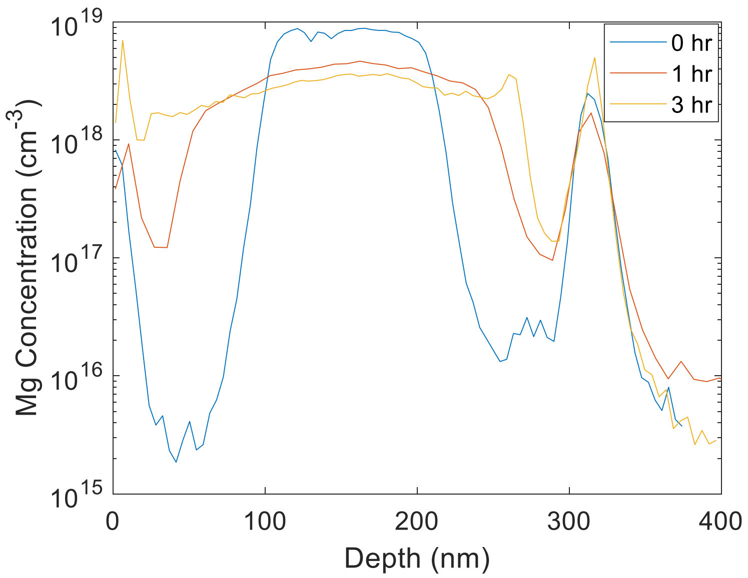

Figure 4.4: Mg diffusion observed after annealing in a vacuum (MBE) at 950 °C for varying times.

To investigate the nature of Mg diffusion in β-Ga_2O_3 at higher temperatures, three substrates were coloaded for growth at 650 °C of a Mg doped layer between two UID layers on an Fe doped (010) β-Ga_2O_3 substrate. Figure 4.4 shows the SIMS profile of the as-grown sample shown in blue, with a Mg concentration of 8×10^{18} cm^{-3}. The two other samples were annealed in the vacuum of the MBE chamber at 950 °C for 1 and 3 hours, demonstrating significant diffusion, as shown by the two other profiles in Fig. 4.4.

To further explore the nature of Mg diffusion in β-Ga_2O_3 films during post-growth annealing, an extensive diffusion series was explored. Annealing was performed in a tube furnace with atmospheric environment and an O_2 (estimated purity 99.999%) supply of 0.2 liters per minute to suppress potential Ga_2O_3 decomposition in an oxygen deficient environment at high temperatures. For growth of the Mg doped films for this diffusion series, many samples were coloaded for PAMBE growth at 700 °C to ensure identical structures prior to annealing. Each sample was subject to a single annealing process at a temperature and time. The structure consisted of a 170 nm Mg doped layer with a Mg concentration of 4×10^{20} cm^{-3} between two 340 nm UID films, all on an Fe-doped substrate. Anneals were performed at temperatures of 925 °C, 1000 °C, and 1050 °C for either 75 minutes or 225 minutes and the Mg SIMS profiles were compared to that of the unannealed sample as shown in Fig. 4.5a. A ramp rate of 10 °C per minute was used for all heating and cooling in the tube furnace.

The as-grown sample had a relatively sharp profile with turn-on and turn-off slopes of 14 and 19 nm/dec, respectively, as seen by the blue profile depth profile in Fig. 4.5a going from the UID layer at the surface of the film, down into the Fe-doped substrate at a depth of about 850 nm. The spike of Mg between the UID layer and substrate is a result of atmospheric impurities that typically exist at the substrate surface and incorporate at the film-substrate interface, even in epitaxial films without Mg doping. A similar spike of Si at the substrate-film interface in SIMS of epitaxial β-Ga_2O_3 films.[13] The higher Mg concentration in the top 50 nm of the film in the as-grown sample is an artifact of SIMS measurements, similarly due to atmospheric impurities on the film surface rather than a result of the growth or diffusion. While the Mg concentration reaches a baseline of 10^{15} cm^{-3} in the UID layer near the surface of the as-grown film, which is near the noise level of the measurement, some Mg incorporation into the UID film on the substrate side can be seen by the tail of Mg to around 10^{17} cm^{-3}.

The Mg SIMS profiles following diffusion for various annealing temperatures and times are also plotted in Fig. 4.5a, showing increased diffusion at higher temperatures and times. This can be seen by the increased accumulation of Mg at the surface of the film with higher annealing temperature and time. Furthermore, the tail of Mg following diffusion from the Mg doped layer into the top UID layer was more pronounced for higher annealing temperatures and time, while the Mg level in the Mg-doped region was depleted. In particular, the Mg in the intentionally Mg-doped layer was depleted significantly after the 1050 °C anneal. Integrating the total concentration in the UID layer near the surface shows that most of this diffusing Mg concentration (2.6×10^{15} cm^{-2}) was in this region. The total Mg in the originally Mg-doped region was around 5×10^{15} cm^{-2} prior to diffusion, and about 10^{15} cm^{-2} in this same region after diffusion for the 1050 °C anneal. In the substrate, the Mg concentration diffuses to approximately 10^{18} cm^{-3} for all anneals performed.

Deeper SIMS profiles for the various diffusion temperatures and times are shown in Fig. 4.5b. All anneals performed showed significant Mg diffusion into the Fe-doped substrate. Anneals at the higher temperatures of 1000 °C and 1050 °C showed Mg diffusion through the entire depth of the SIMS scan, around 2 µm into the substrate. Two anneals were performed at a temperature of 925 °C for times of 75 min and 225 min. Both showed some Mg diffusion into the substrate before the Mg concentration drops off to less than 10^{16} cm^{-3}, which is the typical Mg concentration in the Fe doped substrate. A Mg bulk diffusion length of approximately 800 nm and 1200 nm for the times of 75 min and 225 min respectively could be seen after this 925 °C anneal.

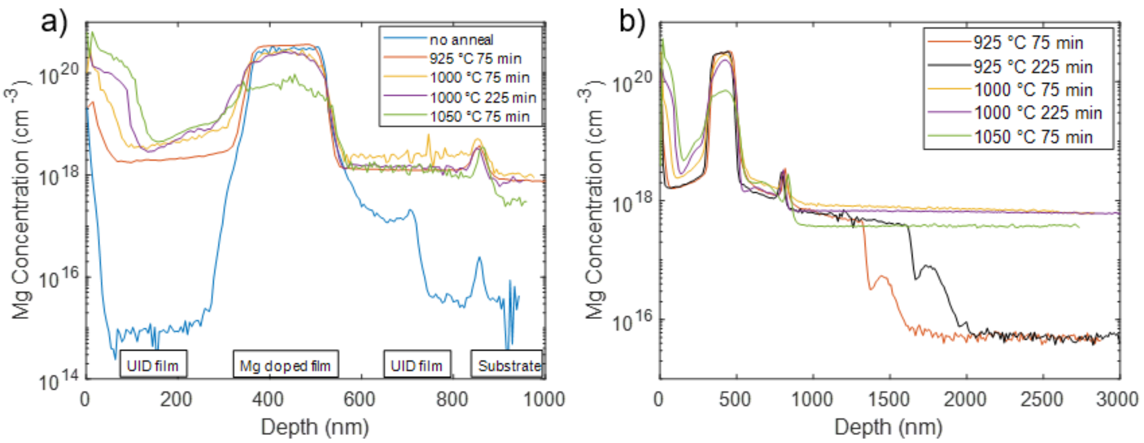

Figure 4.5: Mg profiles from short range (a) and long range (b) SIMS scans after annealing at various temperatures and times in tube furnace.[7]

Interestingly, the Mg concentration seems to diffuse to a concentration of ~10^{18} cm^{-3}. This diffusion level could be tied to a defect or impurity in the material. Wong et al. demonstrated that Mg in ion implanted samples diffused to the level of active donors such as Sn or Si in that sample, and suggested that this was due to Coulombic interaction between the Mg acceptor and donor.[5] This level is likely due to the Fe concentration in the substrates (3×10^{18} cm^{-3}), with the Fermi level pinned at 0.8 eV below the conduction band.[14] While Mg on the Ga site (Mg_{Ga}) acts as an acceptor, Mg was predicted to diffuse as a donor interstitial species (Mg_i) by Peelaers et al.[3] This interstitial species is extremely mobile, however for the interstitial to form from Mg on the Ga site in the absence of other point defects, it requires the formation of a Ga vacancy (V_{Ga}) via the following reaction: $Mg_{Ga} \rightarrow Mg_i + V_{Ga}$, which is energetically unfavorable.[3] There could be a small fraction of the Mg forming on the interstitial site during growth, which could lead to the slight tail in Mg concentration towards the substrate as seen in the as-grown SIMS profile in Fig. 4.5a. Still, the remainder of the Mg_{Ga} would need to interact with a point defect to form the Mg_i. In the presence of an existing Ga interstitial (Ga_i), a Mg interstitial can form via the following reaction $Mg_{Ga} + Ga_i \rightarrow Mg_i + Ga_{Ga}$. Alternatively, Mg on the Ga site (Mg_{Ga}) could diffuse in the presence of an existing Ga vacancy (V_{Ga}), via a vacancy-assisted mechanism where the Mg remains on the Ga site. This, however, will be limited by the tendency of the negatively charged V_{Ga} and Mg_{Ga} to repel each other.

While the spontaneous formation after growth of the Ga vacancy or Ga interstitial in the Mg doped film is unlikely, either may be formed at the surface of the films during annealing and diffuse to the Mg-doped film and substrate. These point defects then assist the Mg diffusion. Furthermore, the high Mg concentration measured by SIMS near the surface of the film, particularly for the higher annealing temperature and times could be indicative of Mg interacting with point defects formed near the surface of the film. Figure 4.6 shows a schematic of potential point defect reactions that could be involved in the observed Mg diffusion. The Mg SIMS profile after the 1000 °C 225 minute anneal is also shown for reference with four regions of the film labeled corresponding to the regions shown in the schematic. Region I shows the surface of the film where Mg concentration is high, potentially due to the Mg_i reaction with V_{Ga} to form Mg_{Ga} near this surface. Mg_i could also exchange with a Ga atom to form Mg_{Ga} and a mobile Ga interstitial (Ga_i). The Ga_i formed near this surface then diffuses through region II to the Mg doped film as shown in the schematic. Additionally, any Mg_{Ga} in region I would move the Fermi level down in this region. This would set up an electric field that promotes drift of Mg_i donors to the surface, further contributing to this accumulation. Region III shows the intentionally Mg doped film, where Mg_{Ga} can react with Ga_i to form Mg_i that diffuses outwards to other regions.

For reference, the formation energy diagrams for various point defects involved in this diffusion process are shown in Fig. 4.7, with data from Peelaers et al.[3,7] Point defects with lower formation energies are more likely to form, with both Ga-rich and O-rich conditions showing the preference for Mg to occupy the Ga site for the higher range of Fermi levels. The slopes of the formation energy lines show the charge states of the defects. Presumably as more Mg_{Ga} is formed during growth and the Fermi level moves lower in the gap, donor oxygen vacancies (V_O) would form more readily, suggesting that for the as-grown, heavily Mg doped region of the film, the Fermi level would be near the intersection of the V_O and Mg_{Ga} lines. For Ga-rich conditions, this level is around 3.3 eV above the valence band and for O rich conditions this would be around 1.6 eV above the valence band. It is expected that the Fermi level is between these levels in the gap for the Mg doped film after growth. Aside from participating in compensation, the oxygen vacancies do not participate in Mg diffusion, as discussed in Ref. 3. During diffusion, Ga_i donors diffuse through the UID material and into the Mg doped film, and Mg_i donors diffuse outwards. Some proportion of the Mg_i diffusing towards the surface of the film and into the substrate exchanges with Ga atoms to form Mg_{Ga}, moving the Fermi level lower in the gap.

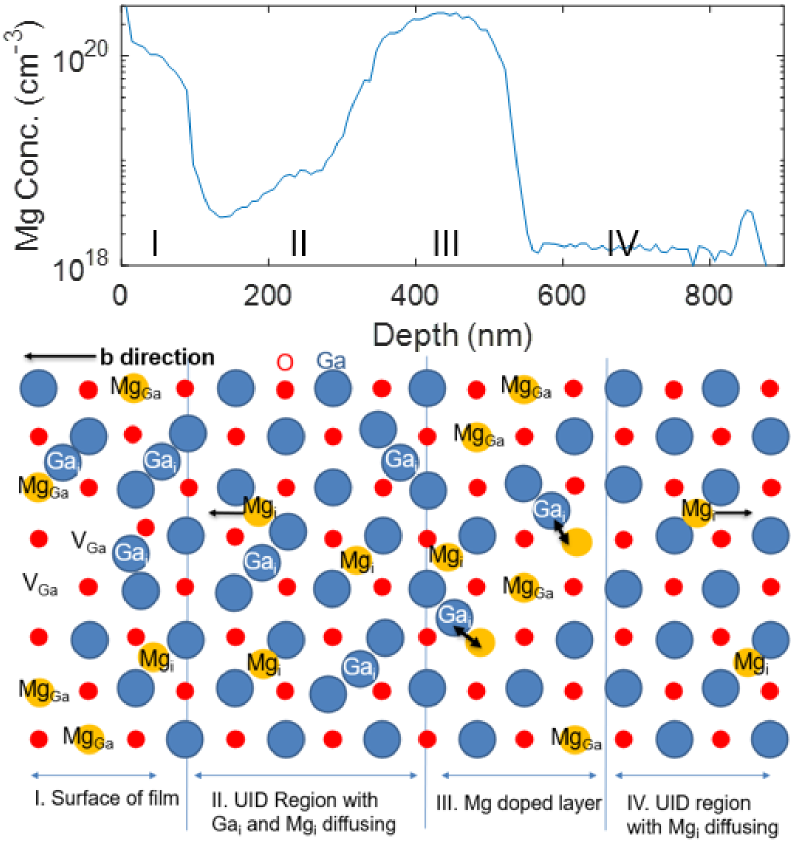

Figure 4.6: Schematic of point defect reactions in regions of film after annealing, along with a SIMS profile of an annealed Mg doped film. Region I shows the film surface where Mg accumulates and exists in the form of Mg_i and Mg_{Ga}. Regions II and IV show the two UID layers of the film with diffusing Mg_i and Ga_i. Region III shows the intentionally Mg doped layer where Mg_{Ga} exchanges with Ga_i to form Mg_i that then diffuses to the other regions of the film and into the substrate.[7]

This effect of Mg diffusion at higher temperatures limits the use of Mg as an acceptor to lower temperature growth and processing. As described in Chapter 2, the ability to grow β-Ga_2O_3 films at higher temperatures via indium catalyzed growth has shown promise for better film quality and heterostructures in MBE. However, the higher range of these temperatures for this metal oxide catalyzed epitaxy (MOCATAXY) could allow for similar Mg diffusion. Still, at the lower temperatures of conventional PAMBE, a wide range of Mg doping concentrations can be achieved with sharp doping profiles. Therefore, Mg can be utilized as a convenient, controllable deep acceptor dopant in β-Ga_2O_3 grown via conventional PAMBE.[7]

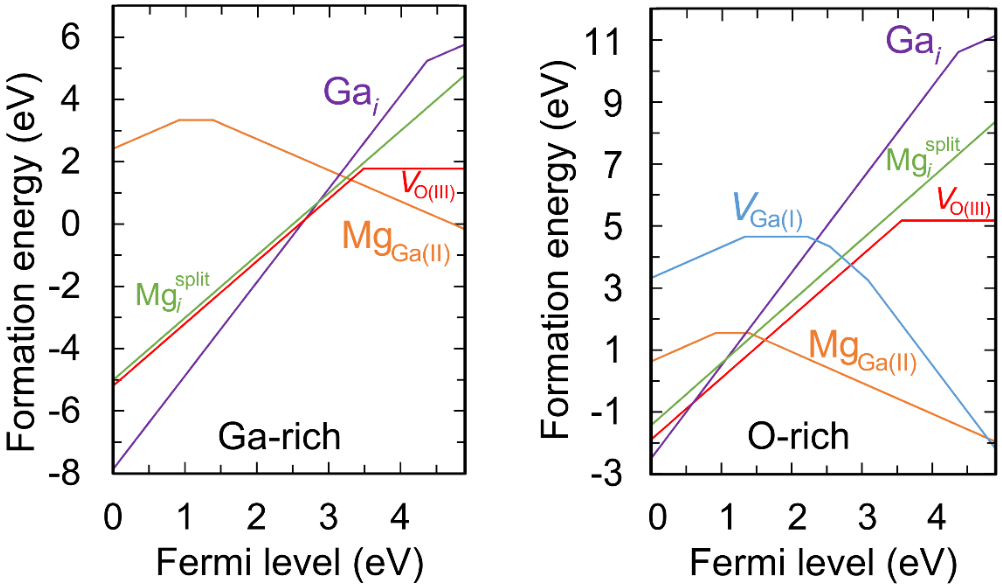

4.7: Formation energies of various point defect that may play a role in the Mg doping under the Ga-rich and O-rich approximations.[3,7]

4.3 Fe Surface Segregation

For investigation of unintentional Fe incorporation into β-Ga_2O_3 films, growth was performed on Fe doped (010) β-Ga_2O_3 substrates from Novel Crystal Technology. Substrates were produced via bulk crystal growth from an edge-defined film fed melt growth method (EFG), followed by wire sawing, grinding, and chemical mechanical polishing. Conventional PAMBE growth conditions were used with a typical Ga flux of 8×10^{-8} torr measured by beam equivalent pressure (BEP). This Ga and active O flux resulted in growth near stoichiometry in the Plateau regime, with growth rates around 2.3 nm/min for growth temperatures from 500 °C to 650 °C and 1.8 nm/min at 700 °C. The samples were O polished for 30 minutes at 800 °C before growth similar to growth described in previous chapters.

To determine the growth parameters affecting this Fe tail, three 300 nm films were grown at different temperatures (650 °C, 500 °C and 400 °C) and SIMS was performed to characterize the Fe profile. Figure 4.8a shows that the three Fe profiles clearly demonstrate a shorter length of the Fe tail for lower growth temperatures. The Fe concentration drops below the SIMS detection level around 10^{15} cm^{-3} for the lower growth temperatures while the Fe incorporates down to a level of 10^{16} cm^{-3} for the growth temperature of 650 °C resulting in tail that extends across the 200 nm of the film grown. For the samples grown at 400 °C and 500 °C the tail lengths are approximately 25 nm and 50 nm respectively. A decrease in growth temperature from 500 °C to 400 °C resulted in an increase in RMS roughness from 0.50 nm to 2.81 nm. Figure 4.8b shows the rougher surface morphology of the low temperature film while Fig. 4.8c shows the smooth surface morphology of a typical high quality (010) β-Ga_2O_3 film grown at 500 °C.

To determine whether or not the unintentional Fe tail in β-Ga_2O_3 is due to diffusion, films samples were grown together at 650 °C on different substrates and annealed separately at 900 °C for either 0, 1, or 3 hours. Figure 4.9 shows the Fe tails for the three samples with no significant observed effect of annealing time, despite the temperature being much higher than the 650 °C growth temperature of the sample demonstrating significant Fe tails in Fig. 4.8a. This lack of significant diffusion after annealing at a high temperature was also shown by Wong et al. for non-implanted epitaxial grown films on Fe doped substrates. For comparison, films with implant damage saw enhanced Fe diffusion after annealing at these temperatures.[5] This suggests that Fe could be riding the surface during high temperature growth with increased incorporation in the film for lower temperature layers. A temperature dependent dopant incorporation has been observed for intentional Ge doping of PAMBE β-Ga_2O_3.[9,11]

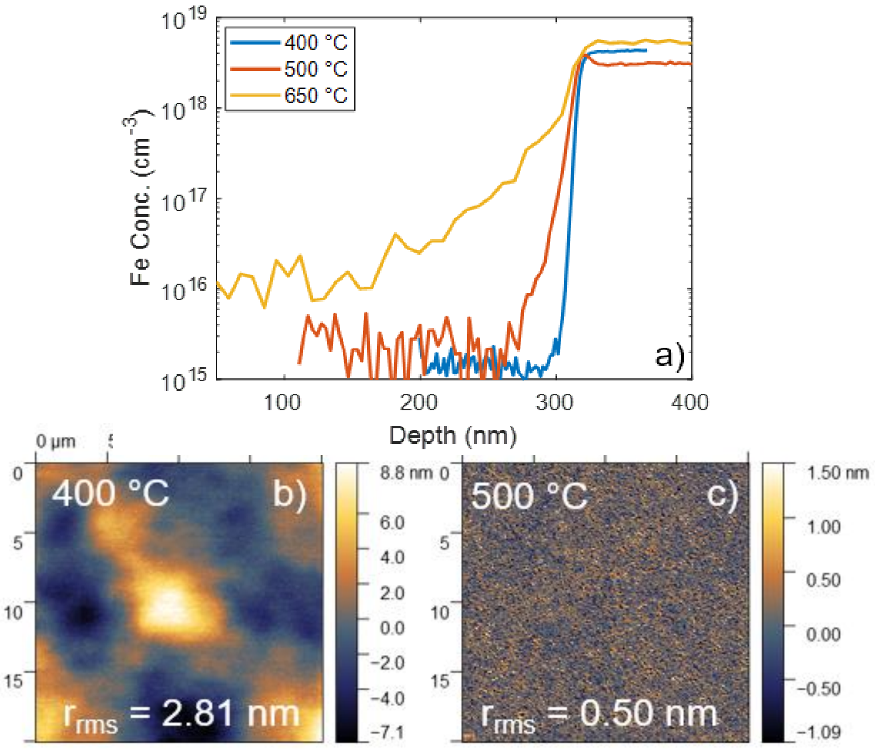

Figure 4.8: SIMS profiles of Fe incorporation into UID films grown on Fe doped (010) β-Ga_2O_3 at various growth temperatures (a). AFM surface morphologies of films grown at 400 °C (b) and 500 °C (c).[8]

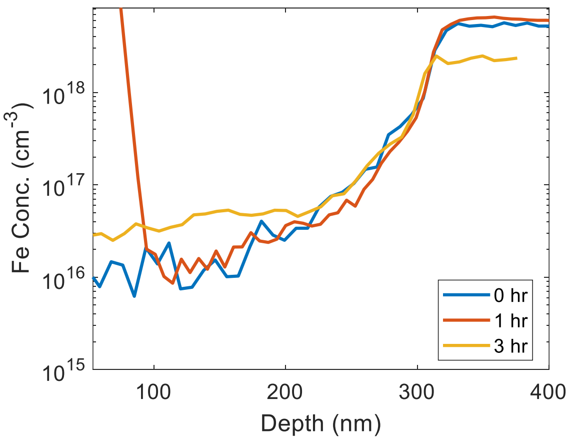

Figure 4.9: SIMS profile of Fe incorporation into UID films grown on Fe doped (010) β-Ga_2O_3 at 650°C after annealing at 900 °C for different times.[8]

To further confirm the surface riding nature of Fe in β-Ga_2O_3 grown by PAMBE, a high temperature (700 °C) / low temperature (500 °C) superlattice was grown with five 20 nm periods and a 120 nm high temperature capping layer. The SIMS profile and stack structure are shown in Fig. 4.10, demonstrating higher Fe incorporation into the low temperature layers. This profile suggests difference in segregation of Fe based on growth temperature rather than diffusion, with higher temperature growth allowing a larger proportion of Fe on the surface of the film to continue to surface ride than lower temperature growth.

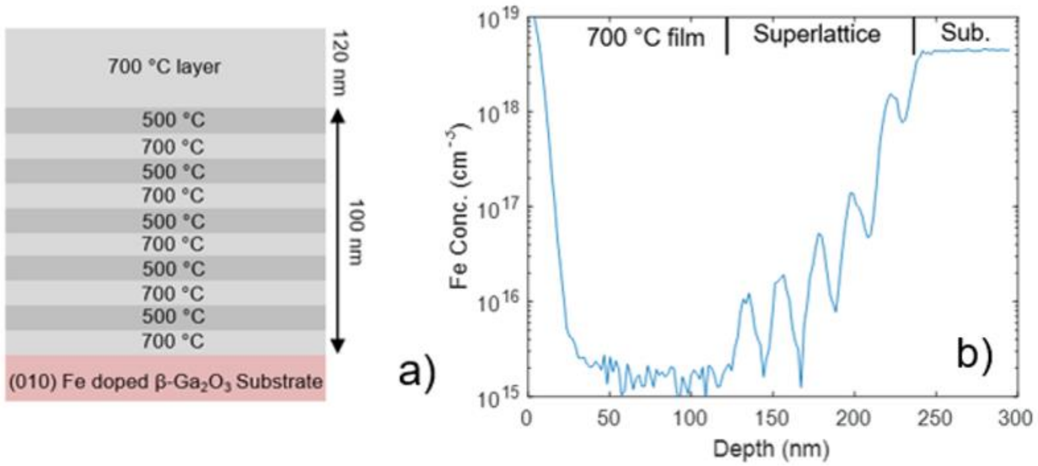

Figure 4.10: Schematic of layer stack of high temperature / low temperature superlattice structure grown on Fe doped (010) β-Ga_2O_3 (a). SIMS profile of Fe profile into superlattice structure showing higher incorporation into low temperature layers (b).[8]

A larger period (200 nm) high temperature / low temperature superlattice was grown with the same growth conditions to quantify the Fe segregation and surface riding. This SIMS profile is shown in Fig. 4.11a. Once again, higher Fe incorporation was realized in the layers grown at low temperature. Additionally, the Fe concentration at the end of the first low temperature layer grown was consistent with that at the beginning of the next low temperature layer, suggesting that most of the Fe surface rides through the higher temperature layer. This was also demonstrated by the clear difference in slope of the Fe tail in the SIMS profile for the two different growth temperatures. The increase in Fe concentration in the film at the beginning of the growth of low temperature layers was consistent with higher Fe incorporation at lower growth temperatures. When minimal Fe surface rides, Fe incorporation falls below the detection limit of the SIMS measurement (~10^{15} cm^{-3}).

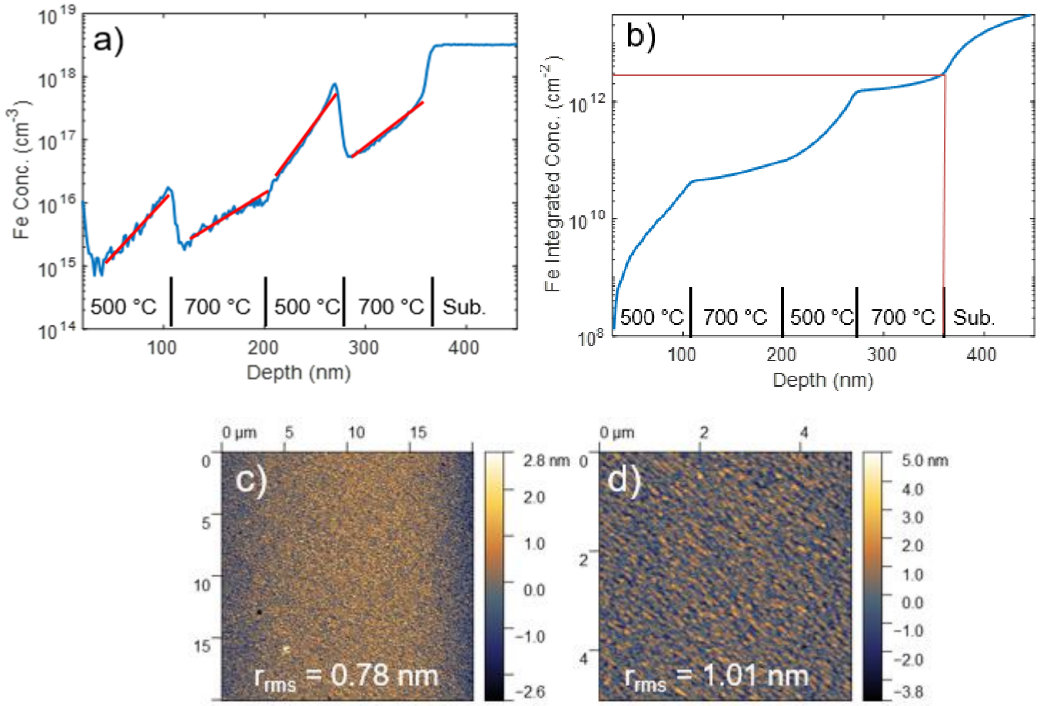

Figure 4.11: SIMS profile of Fe incorporation in low temperature / high temperature superlattice grown on Fe doped (010) β-Ga_2O_3 showing more efficient Fe trapping at lower temperatures (a). Integrated Fe concentration from surface of the film down into the substrate (b). AFM surface morphologies for 20 µm x 20 µm area (c) and 5 µm x 5 µm area (d) of superlattice film.[8]

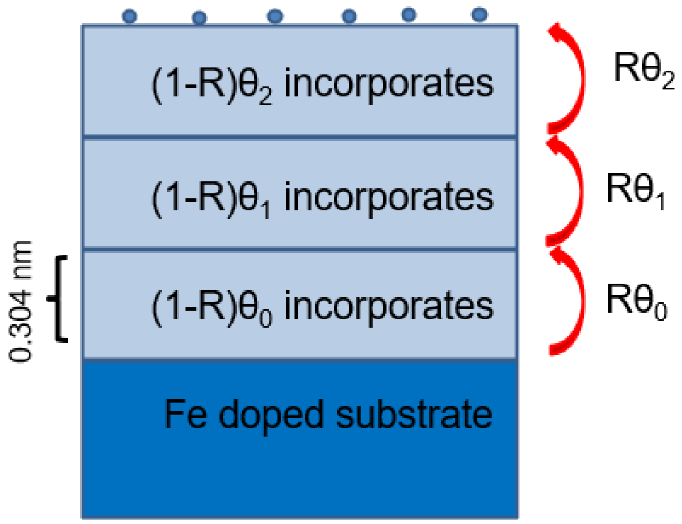

Figure 4.12: Schematic showing Fe surface segregation effect along with surface segregation coefficient R.

To quantify the amount of Fe that surface rides, the Fe concentration was integrated out from the surface of the film down to into the substrate itself. The kinks in this integrated Fe concentration vs. depth profile shown in Fig. 4.11b were consistent with the interface between layers of the film grown at different temperatures. Provided that nearly all the surface riding Fe incorporated into the film structure in this Fe trapping structure, the integrated surface concentration at the film-substrate interface gives the total amount of Fe that surface rides at the onset of growth and eventually incorporates into the structure. This is shown to be about 3×10^{12} cm^{-2} in Fig. 4.11b (i.e., about 0.005 monolayers of initial Fe coverage θ_0). An ideal Fe trapping structure would be designed to consume this quantity of Fe to prevent significant incorporation into the structure grown on top of it. Figures 4.11c and 4.11d show AFM images demonstrating that a smooth morphology was maintained for this low temperature / high temperature film structure with an RMS roughness around 1 nm.

Additional analysis of the incorporation of Fe at the two growth temperatures (500 °C and 700 °C) can yield a quantitative model of Fe incorporation at these growth temperatures. This model used in Refs. 15 and 16 assumes that some fraction (R) of Fe atoms present at the growth surface segregates and rides the film surface while the fraction (1-R) incorporates into a given layer of thickness 0.304 nm (unit cell's length). Taking an initial surface coverage determined previously (θ_0) at the beginning of growth, the surface coverage after the nth layer of growth (θ_n) and sheet concentration n that layer $[Fe]_n$ can be determined. A schematic of this surface segregation effect is shown in Fig. 4.12 for a layer with surface segregation coefficient R. The following equations can be used to relate the Fe surface coverages, sheet concentration within a 0.304 nm thick layer, and surface segregation coefficient:

$$\theta_n = \theta_0 R^n \quad \text{(eqn. 4.1)}$$

$$[Fe]_n = \theta_0(1-R)R^{n-1} \quad \text{(eqn. 4.2)}$$

The total Fe incorporated into a structure of N layers (Q_{Fe}) can be quantified as follows:

$$Q_{Fe} = \theta_0(1-R^N) \quad \text{(eqn. 4.3)}$$

By fitting the SIMS profile, the surface segregation coefficient R can be calculated using the following equation[15,16]:

$$\mathrm{R} = \left(\frac{[Fe]_N}{[Fe]_1}\right)^{\frac{1}{N-1}} \quad \text{(eqn. 4.4)}$$

Fitting the SIMS profile to an exponential decay of Fe concentration over the two different layers separately yields R = 0.993 at a growth temperature of 700 °C and R = 0.982 for a growth temperature of 500 °C, with a higher R corresponding to a greater proportion of surface riding of Fe. This means about 0.7% of surface riding Fe incorporates into a unit cell's length (3.04 Å) of (010) β-Ga_2O_3 grown at 700 °C whereas about 1.8% incorporates for the same thickness of a layer grown at 500 °C. This model's agreement with SIMS data further confirms that this segregation effect determines the surface riding nature of Fe, which is similar to Ca in GaN.[15] This effect was quantified for (010) β-Ga_2O_3, but it might differ between growth orientations with different surface kinetics, as well as other epitaxial growth techniques.

Using this model, the minimum thickness of an Fe trapping layer needed to trap a given surface riding concentration can be calculated. For $\theta_0 = 3\times10^{12}$ cm^{-2}, a layer grown at 500 °C would need to be about 125 nm to reduce Fe to below 10^{15} cm^{-3}. For 700 °C growth, this Fe trapping layer thickness would need to be about 280 nm. The actual net surface riding Fe concentration at the onset of growth is likely influenced by Fe doping concentration in the substrate and surface preparation techniques.

To analyze crystal quality dependence on growth temperature, a film stack was grown with four 100 nm layers with decreasing growth temperature from typical growth conditions at 700 °C to low temperature growth at 400 °C as shown in Fig. 4.13a. This cross-sectional transmission electron microscopy (TEM) image demonstrates no evidence of twinning or dislocations in the layers grown at 500 °C or hotter, suggesting that the low temperature Fe trapping structures can be grown with little introduction of extended defects. The lowest temperature 400 °C layer at the top of the stack demonstrated loss of single crystalline β-phase Ga_2O_3. The Fe tail profile from SIMS is shown in Fig. 4.13b which demonstrates the temperature dependent surface riding effect. No increase in Fe incorporation is seen after the 500 °C growth at the onset of 400 °C growth due to either sufficient trapping of Fe in the first three layers or a small difference in surface segregation coefficient between 400 °C and 500 °C growth.

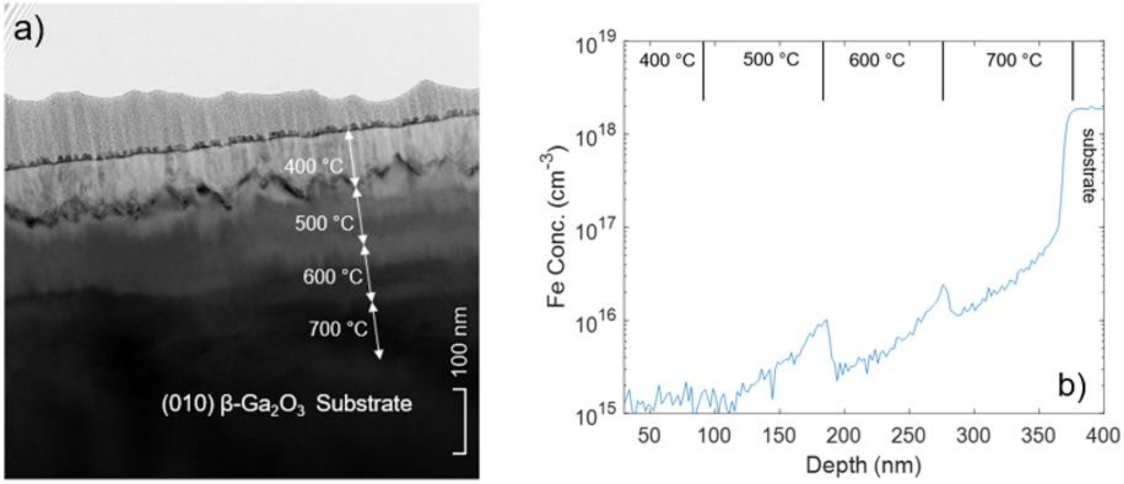

Figure 4.13: Cross-section TEM of stack structure with layers with varying growth temperatures showing loss of crystallinity at 400 °C (a). Fe profile measured by SIMS for the stack structure (b).[8]

In addition to SIMS and TEM, structural analysis of this sample via HRXRD was performed to further investigate crystal quality of this structure. ω-rocking curves of the (020) and (111) reflections demonstrated full width at half maximums similar to that of typical PAMBE grown films, suggesting little mosaic or extended defects as expected in optimized homoepitaxy of (010) β-Ga_2O_3.

Through investigation of Fe incorporation into PAMBE grown (010) β-Ga_2O_3, Fe was conclusively shown to surface ride rather than diffuse into films grown on Fe doped substrates. Surface segregation coefficients of R = 0.993 at 700 °C and R = 0.982 for 500

°C growth were found. Additionally, no extended defects were observed for growth temperatures from 500 to 700 °C, however 400 °C growth led to loss of crystallinity and rougher surface morphologies. The ability to trap Fe more effectively at lower growth temperatures can be utilized via a 500 °C Fe trapping layer prior to device growth without roughening the surface or introducing unintentional defects. The ideal Fe trapping layer thickness would depend on total surface riding Fe concentration, however a 150 nm layer would sufficiently trap the typically observed 3×10^{12} cm^{-3} surface riding Fe concentration determined in this work.

4.4 Summary

Mg and Fe as deep acceptor dopants in β-Ga_2O_3 have been investigated. Intentional doping of (010) β-Ga_2O_3 with Mg in conventional PAMBE allowed for a wide range of acceptor concentrations and sharp, controllable profiles. Annealing of Mg doped films showed significant diffusion at temperatures of 925 °C and higher. This could lead to unintentional Mg incorporation into critical regions of devices for structures that require higher temperature growth or processing steps. The mechanism of Mg diffusion was predicted to be via the Mg interstitial species that is formed via a point defect reaction between Ga interstitials and Mg on the Ga site. Still, Mg doping could be useful for conventional PAMBE grown device structures.

The nature of Fe incorporation from Fe doped substrates into epitaxially grown β-Ga_2O_3 was also studied. Annealing of UID films post growth at 900 °C revealed minimal change in Fe incorporation from the substrate, suggesting this incorporation is not due to diffusion during epitaxial growth. High temperature-low temperature superlattices demonstrated significantly higher incorporation into layers grown at lower temperatures, suggesting the Fe incorporation is due to temperature dependent surface segregation during epitaxial growth. Fitting of the Fe profiles yielded surface segregation coefficients and suggested that low temperature Fe trapping buffers could be utilized prior to growth of critical regions of device structures to limit unintentional Fe incorporation. Application of this low temperature Fe trapping buffer layer to other epitaxial growth techniques could be an interesting solution to this Fe incorporation problem observed for those techniques as well.

References:

1. M. H. Wong, K. Goto, Y. Morikawa, A. Kuramata, S. Yamakoshi, H. Murakami, Y. Kumagai, and M. Higashiwaki. Appl. Phys. Exp. **11**, 064102 (2018).
2. H. Peelaers, and C. G. Van de Walle. Phys. Status Solidi B. **252**, 4 828 (2015).
3. H. Peelaers, J. L. Lyons, J. B. Varley, and C. G. Van de Walle. APL Materials **7**, 022519 (2019).
4. F. Alema, Y. Zhang, A. Osinsky, N. Orischin, N. Valente, A. Mauze, and J. S. Speck, APL Materials **8**, 021110 (2020).
5. M. H. Wong, C. H. Lin, A. Kuramata, S. Yamakoshi, H. Murakami, Y. Kumagai, and M. Higashiwaki, App. Phys. Lett. **113**, 102103 (2018).
6. M.H. Wong, K. Sasaki, A. Kuramata, S. Yamakoshi, and M. Higashiwaki. Appl. Phys. Lett. **106**, 032105 (2015).
7. A. Mauze, Y. Zhang, T. Itoh, T. Mates, H. Peelaers, C. G. Van de Walle, and J. S. Speck. J. Appl. Phys. **130,** 33 (to be published 2021).
8. A. Mauze, Y. Zhang, T. Mates, F. Wu, and J. S. Speck, Appl. Phys. Lett. **115**, 052102 (2019).
9. Y. Zhang, A. Mauze, F. Alema, A. Osinsky, and J. S. Speck. App. Phys. Exp. **12** (4), 044005 (2019).
10. E. Ahmadi, O. S. Koksaldi, S. W. Kaun, Y. Oshima, D. B. Short, U. K. Mishra, and J. S. Speck, Appl. Phys. Exp. **10** (4), 041102 (2017).
11. S.H. Han, A. Mauze, E. Ahmadi, T. Mates, Y. Oshima, and J. S. Speck, Semiconductor Science and Technology **33,** 045001 (2018).
12. A. Mauze, Y. Zhang, T. Itoh, E. Ahmadi, and J. S. Speck. Appl. Phys. Lett. **117**, 222102 (2020).
13. E. Ahmadi, O. S. Koksaldi, X. Zheng, T. Mates, Y. Oshima, U. K. Mishra, and J. S. Speck. Appl. Phys. Exp. **10**, 071101 (2017).
14. M.E. Ingebrigtsen, J.B. Varley, A.Y. Kuznetsov, B.G. Svensson, G. Alfieri, A. Mihaila, U. Badstubner, Appl. Phys. Lett. **112**, 042104 (2018).
15. E. C. Young, N. Granjean, T. E. Mates, and J. S. Speck. Applied Physics Letters **109** 212103 (2016).
16. K. Muraki, S. Fukatsu, and Y. Shiraki. Applied Physics Letters **61** 557 (1992).

Chapter 5: β-$(Al_xGa_{1-x})_2O_3$ / β-Ga_2O_3 Heterostructures

5.1 Introduction

One area that needs development is growth of alloys and heterostructures in the β-Ga_2O_3 materials systems. Alloys in the semiconductor materials have been used to tune bandgaps and lattice constants for applications in optoelectronics, transistors, and for lattice matched buffer layers. InGaN is commonly used in LED applications, while AlGaAs and AlGaN are used to produce heterostructure based devices like modulation doped field effect transistors. Similarly, the β-$(Al_xGa_{1-x})_2O_3$ alloy can be used to make heterostructures with β-Ga_2O_3. The introduction of higher Al contents increases the conduction band offset between the β-$(Al_xGa_{1-x})_2O_3$ and β-Ga_2O_3 allowing for more charge in the 2-dimensional electron gas (2DEG) channel, and therefore more efficient device performance.[1-2] Furthermore, higher 2DEG channel charge has been predicted to screen phonons more, allowing for higher mobility in the channel.[3]

One complication with growing thin films with higher Al content in β-$(Al_xGa_{1-x})_2O_3$ arises due to the difference in crystal structures of Al_2O_3 and Ga_2O_3. The stable phase of Ga_2O_3 is the monoclinic β-phase, while the thermodynamically stable phase of Al_2O_3 is the α-corundum phase. Hill et al. produced a phase diagram from ceramic methods demonstrating the stable phases of alloys in the Al_2O_3-Ga_2O_3 materials systems. Here it was shown that the Al contents that are stable in the β-phase are limited to ~20-30% for temperatures up to 800 °C, above which ~60% Al content in the β-phase is stable before phase separation.[4] For epitaxial growth, this suggests that higher growth temperatures may be able to achieve higher Al contents. In addition to phase stability, the lattice mismatch between β-$(Al_xGa_{1-x})_2O_3$ and β-Ga_2O_3 also plays a role in epitaxial growth. The higher the Al content in β-$(Al_xGa_{1-x})_2O_3$, the smaller the relaxed lattice spacing, and the greater the tensile strain in a coherent β-$(Al_xGa_{1-x})_2O_3$ film on β-Ga_2O_3. Mu et al. predicted critical thickness before cracking of β-$(Al_xGa_{1-x})_2O_3$ on β-Ga_2O_3 for various crystallographic orientations and Al contents. It was calculated that the critical thickness for (100) β-$(Al_xGa_{1-x})_2O_3$ was greater than (010) and (001) orientations for the same Al contents. Furthermore, cracking is expected to significantly limit maximum Al contents for typical β-$(Al_xGa_{1-x})_2O_3$ thicknesses required for heterostructures based devices.[5] Johnson et al. studied phase stability in β-Ga_2O_3 using scanning tunneling electron microscopy, showing planar defect formation and phase instability at higher Al contents.[6]

The (010) orientation has been the primary focus for epitaxial growth of β-Ga_2O_3, due to high quality films with high electron mobility and early device demonstration in this orientation. Oshima et al. demonstrated a compositional analysis of Al content in coherently strained PAMBE grown (010) β-$(Al_xGa_{1-x})_2O_3$ films grown on β-Ga_2O_3 to allow for quantification of Al content based on out of plane lattice spacing determined from high resolution X-ray diffraction (HRXRD).[7] Since then, PAMBE growth has been utilized to grow high quality (010) β-$(Al_xGa_{1-x})_2O_3$ / β-Ga_2O_3 heterostructures that have been used for modulation doped field effect transistors and high mobility heterostructures.[1-2]

5.2 (010) β-$(Al_xGa_{1-x})_2O_3$

Oshima et al. calculated the relationship between out of plane lattice parameter of (010) β-$(Al_xGa_{1-x})_2O_3$ and Al content for films coherently strained to β-Ga_2O_3.[7] Using the fundamental stiffness tensor and measured lattice parameters of β-Ga_2O_3 and relaxed β-$(Al_xGa_{1-x})_2O_3$, out of plane strain along the b-direction was calculated. A stiffness tensor of the form below in the stress-strain relationship in eqn. 5.1 was calculated for the monoclinic β-Ga_2O_3 crystal structure, with the cartesian coordinate system's unit axes being the [100] (a) and [010] (b) directions for x_1 and x_2 respectively. For the case of (010) β-$(Al_xGa_{1-x})_2O_3$, the stress component in the out of plane direction (σ_2) is 0 and the out of plane strain (ε_2) can be calculated using the stress-strain relationship using the second line of the stiffness tensor as given by eqn. 5.2 below.

$$\begin{bmatrix} \sigma_1 \\ 0 \\ \sigma_3 \\ 0 \\ \sigma_5 \\ 0 \end{bmatrix} = \begin{bmatrix} c_{11} & c_{12} & c_{13} & 0 & c_{15} & 0 \\ c_{21} & c_{22} & c_{23} & 0 & c_{25} & 0 \\ c_{31} & c_{32} & c_{33} & 0 & c_{35} & 0 \\ 0 & 0 & 0 & c_{44} & 0 & c_{46} \\ c_{51} & c_{52} & c_{53} & 0 & c_{55} & 0 \\ 0 & 0 & 0 & c_{64} & 0 & c_{66} \end{bmatrix} \begin{bmatrix} \varepsilon_1 \\ \varepsilon_2 \\ \varepsilon_3 \\ 0 \\ \varepsilon_5 \\ 0 \end{bmatrix} \quad \text{(eqn. 5.1)}$$

$$\varepsilon_2 = -\frac{(c_{12}\varepsilon_1 + c_{23}\varepsilon_3 + c_{25}\varepsilon_5)}{c_{22}} \quad \text{(eqn. 5.2)}$$

Using known definitions of the in plane and out of plane strains based on relaxed lattice parameters of the β-$(Al_xGa_{1-x})_2O_3$ from Kranert et al.[8] and β-Ga_2O_3 lattice parameters, the relationship between Al content x and out of plane lattice parameter can be derived as shown in eqn. 5.3. To relate this to peak separation between the (020) β-Ga_2O_3 and β-$(Al_xGa_{1-x})_2O_3$ peaks in HRXRD, this was converted to the form in eqn. 5.4.

$$x = 15.923 - 5.238 \times b_c\ (\text{Å}) \quad \text{(eqn. 5.3)}$$

$$x = 0.4727 \times \Delta\theta\ (deg.) \quad \text{(eqn. 5.4)}$$

A more comprehensive version of this derivation is shown in Appendix B. Atom Probe Tomography (APT) was used to confirm the Al content in these films, verifying the validity of this derivation. This analysis allows HRXRD to be utilized to measure Al content for coherently grown β-$(Al_xGa_{1-x})_2O_3$ films in the (010) orientation.

More recently, the use of metal oxide catalyzed epitaxy (MOCATAXY) to grow (010) β-$(Al_xGa_{1-x})_2O_3$ films has been demonstrated. Similar to growth of β-Ga_2O_3, maximum growth temperatures and growth rates were significantly improved via MOCATAXY. Smooth surface morphology was demonstrated via AFM and high quality crystal quality was confirmed via cross-sectional TEM. APT confirmed minimal In incorporation into the film. Figure 5.1 shows the HRXRD 2θ-ω scans of (010) β-$(Al_xGa_{1-x})_2O_3$ films coherently grown on β-Ga_2O_3 substrates via MOCATAXY. The highest Al content achieved in MBE growth of coherent (010) β-$(Al_xGa_{1-x})_2O_3$ films is around 22% for both MOCATAXY and conventional PAMBE.[9]

Increasing Al flux for similar growth conditions to achieve a higher Al content leads to phase segregation in β-$(Al_xGa_{1-x})_2O_3$. For these films, no (020) β-$(Al_xGa_{1-x})_2O_3$ peak is seen HRXRD, however a lower intensity peak is consistently observed at 2θ values around 65° for these phase-separated films as shown in Fig. 5.2. Johnson et al. investigated the crystal structure in films with higher Al content, showing localized inclusions of planar defects perpendicular to the growth direction similar to the γ-phase. These inclusions at higher Al contents in epitaxially grown β-$(Al_xGa_{1-x})_2O_3$ limit the maximum Al contents that can be achieved for the coherent β-$(Al_xGa_{1-x})_2O_3$ necessary for heterostructure based devices.[6]

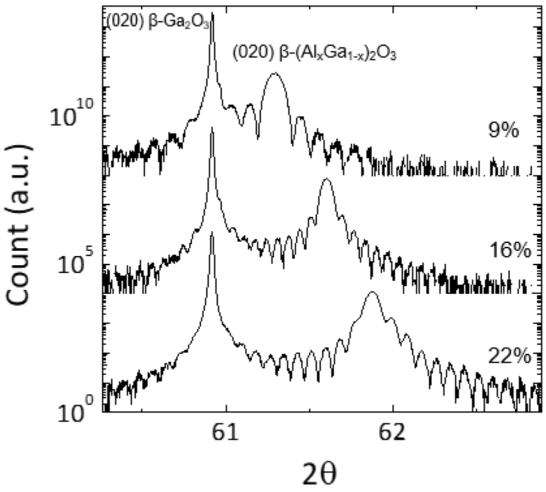

Figure 5.1: HRXRD 2θ-ω scans of β-$(Al_xGa_{1-x})_2O_3$ films with varying Al contents grown on (010) β-Ga_2O_3 substrates.

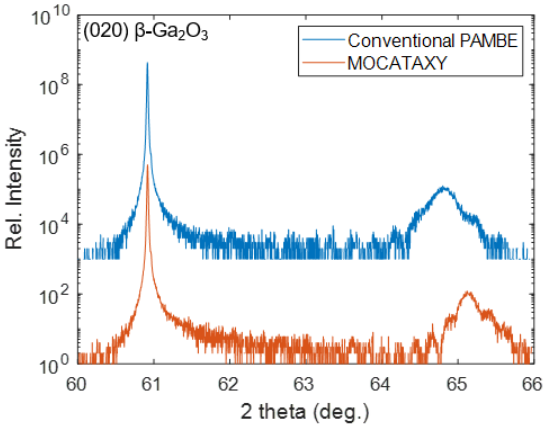

Figure 5.2: HRXRD 2θ-ω scans of phase separated β-$(Al_xGa_{1-x})_2O_3$ films with high Al contents grown via conventional PAMBE and MOCATAXY on (010) β-Ga_2O_3 substrates.

As mentioned in the introduction of this chapter, the critical thickness before cracking of β-$(Al_xGa_{1-x})_2O_3$ was calculated by Mu et al. across various orientations. Interestingly, experimental results for thickness of (010) β-$(Al_xGa_{1-x})_2O_3$ have exceeded these predictions. MBE growth of β-$(Al_xGa_{1-x})_2O_3$ in our work was able to achieve a thickness of 242 nm for 16.3% (010) β-$(Al_{0.16}Ga_{0.84})_2O_3$ while reciprocal space maps confirmed that the film was coherently strained to the substrate beneath it. Still the trend shown by Mu et al. suggests limitations of critical thickness at higher Al contents, potentially limiting the application of extremely high Al content heterostructures.[5] Still, any increase in maximum Al content would significantly improve conduction band offsets in heterostructures, allowing for higher 2DEG charge in the channel, and more efficient devices.

Doping of β-$(Al_xGa_{1-x})_2O_3$ is ultimately necessary for achieving modulation doped field effect transistors.[1-2] Si, Ge, and Sn are candidates for donor dopants in β-Ga_2O_3.[10-14] Si and Ge have been demonstrated as shallow donors in β-Ga_2O_3 with both having been applied to MODFETs.[1-2] The delta doping limitations of Si doping in (010) β-Ga_2O_3 work for the δ-doped MODFETS, with varying doping and spacer thickness allowing for varying 2DEG charges. Ge doping in β-Ga_2O_3 has demonstrated limitations in achieving higher Ge incorporation into the film at higher growth temperatures and Ga/O flux ratios.[10] Because higher Al contents require higher growth temperatures in PAMBE, this could be limiting for Ge doped MODFETs.

To investigate the ability to Ge dope β-$(Al_xGa_{1-x})_2O_3$, various films were grown at a constant Ge cell temperature of 650 °C at a growth temperature of 650 °C and conditions that would typically result in a Ge concentration of 10^{18} cm^{-3}. Interestingly at stoichiometric group III/O fluxes, Ge incorporation for 19% Al content β-$(Al_{0.19}Ga_{0.81})_2O_3$ was ~9×10^{16} cm^{-3}, an order of magnitude lower than for (010) β-Ga_2O_3 grown under the same conditions. The supplied Al flux further suppresses Ge incorporation, limiting its application to MODFETs with high Ge incorporation needed in the doped β-$(Al_xGa_{1-x})_2O_3$ layer.

Sn doping of (010) β-$(Al_xGa_{1-x})_2O_3$ with 20% Al content yields no significant difference in incorporation than (010) β-Ga_2O_3 for both conventional PAMBE and MOCATAXY growth. Fig. 5.3 shows the SIMS profile of Sn doping in a stack with β-$(Al_xGa_{1-x})_2O_3$ between two β-Ga_2O_3 layers, demonstrating similar levels of incorporation. None of the Sn doped β-$(Al_xGa_{1-x})_2O_3$ films demonstrated conductivity in Hall measurements. Varley et al. predicted the transitions for various n-type dopants to deeper states at higher Al contents in β-$(Al_xGa_{1-x})_2O_3$, showing the lowest Al contents at transition for Sn and highest Al content for Si amongst Sn, Ge, and Si.[15] This is in agreement with the experimental demonstration of Si as a shallow dopant in β-$(Al_xGa_{1-x})_2O_3$ and our non-conductive Sn doped β-$(Al_xGa_{1-x})_2O_3$ films.[2]

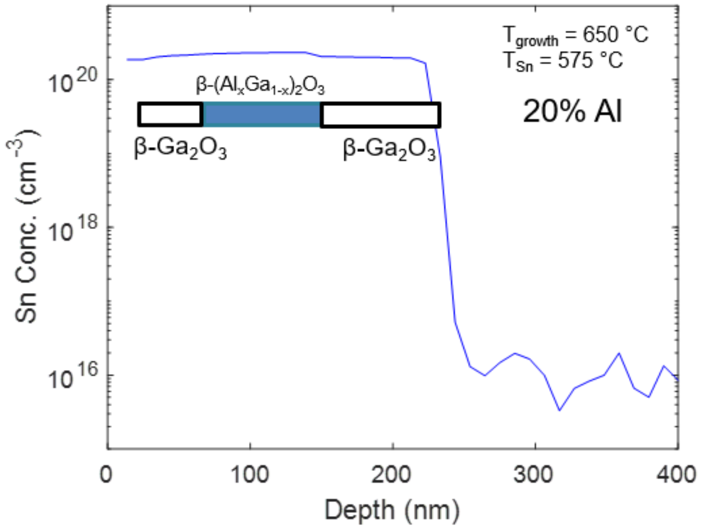

Figure 5.3: Sn doping profile for constant Sn cell temperature in stack with both (010) β-Ga_2O_3 and β-$(Al_xGa_{1-x})_2O_3$.

5.3 (001) β-$(Al_xGa_{1-x})_2O_3$

Poor film quality in (001) growth via conventional PAMBE has limited further investigation into heterostructures and devices in this orientation.[11,16] Our recent work on MOCATAXY growth of (001) β-Ga_2O_3 shows particular promise for improvement of material quality and growth rates in this orientation, potentially opening up applications of device structures grown in this orientation. Its application to (001) β-$(Al_xGa_{1-x})_2O_3$ allows for high quality growth of this alloy, allowing us to study the composition-strain relationship and fundamental properties of coherently strained films of this alloy.

MOCATAXY growth conditions similar to those discussed in Chapter 2 were used for growth of β-$(Al_xGa_{1-x})_2O_3$ films.[11] Growth temperatures of 700 to 900 °C were explored with Ga fluxes of 2-3×10^{-7} torr and an In flux of 4×10^{-7} torr. Fig. 5.4 shows the HRXRD 2θ-ω scans of the (002) β-$(Al_xGa_{1-x})_2O_3$ peaks for growth at 800 °C with varying Al contents. High intensity peaks were observed with fringes indicative of a high-quality film. Thickness around 100 nm was obtained for the β-(Al_xGa_{1-x})$_2$$O_3$ films, showing the potential to grow films thicker than the requirements of typical MODFET structures. These three β-(Al_xGa_{1-x})$_2$$O_3$ films were grown with Sn doping and a cell temperature of 800 °C, corresponding to an expected Sn concentrations in the mid 10^{18} cm^{-3} range. Fig 5.5 shows the typical surface morphology of these β-(Al_xGa_{1-x})$_2$$O_3$ films measured by AFM, with similar groove features to (001) β-Ga_2O_3 films.

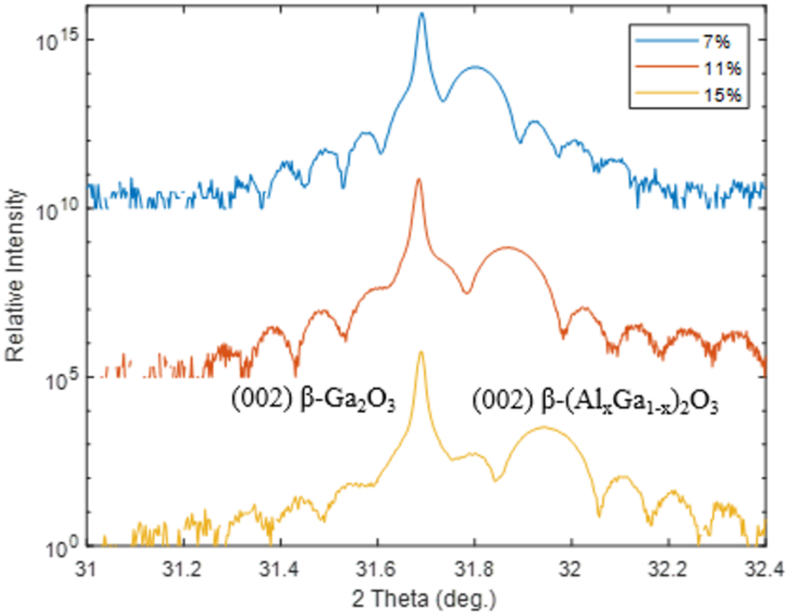

Figure 5.4: HRXRD 2θ-ω scans (001) β-(Al_xGa_{1-x})$_2$$O_3$ films with varying Al contents grown via MOCATAXY on (001) β-Ga_2O_3 substrates. Al contents are estimated based on calculated relationship between out of plane lattice parameter and Al contents shown in eqn. 5.7 and 5.8.

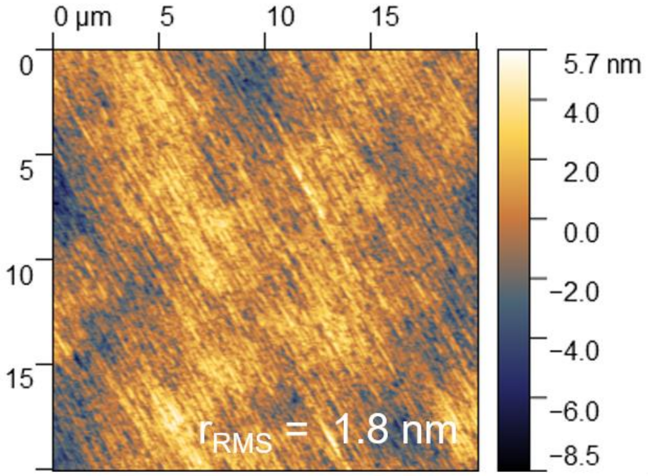

Figure 5.5: Surface morphology of (001) β-$(Al_xGa_{1-x})_2O_3$ film measured by AFM.

Starting from a similar growth condition and decreasing Sn flux (via lower Sn cell temperatures) yielded poorer quality β-$(Al_xGa_{1-x})_2O_3$. Fig 5.6 show the HRXRD profiles of various β-$(Al_xGa_{1-x})_2O_3$ films with identical growth conditions other than Sn cell temperatures. An Al flux of 1.2×10^{-8} torr and a growth temperature of 800 °C was used for all three films. For a Sn cell temperature of 800 °C, a nice (002) β-$(Al_xGa_{1-x})_2O_3$ peak was observed with fringes characteristic of a high-quality film. For a lower Sn cell temperature of 700 °C, a (002) β-$(Al_xGa_{1-x})_2O_3$ peak was still observed with some thickness fringes, but at a lower cell temperature of 600 °C, at which Sn incorporation is expected to be ~10^{16} cm^{-3}, no (002) β-$(Al_xGa_{1-x})_2O_3$ peak was seen in HRXRD.[12] The (001) β-$(Al_xGa_{1-x})_2O_3$ films were non-conductive in Hall measurements. Surface morphology for the various films is also shown in Fig. 5.6 with the highest Sn cell temperature showing the smoothest surfaces.

Various attempts to grow (001) β-$(Al_xGa_{1-x})_2O_3$ without a Sn flux were performed for the range of (001) MOCATAXY growth conditions. Without a Sn flux, growth to growth variation measured via HRXRD was observed, with most films showing spread out (002) β-$(Al_xGa_{1-x})_2O_3$ peaks as seen in Fig. 5.7, indicative of either relaxation or non-uniform thickness or Al composition. This further confirmed the ability for a supplied Sn flux to help stabilize the coherent β-$(Al_xGa_{1-x})_2O_3$ films. Fig. 5.8 shows the RHEED images of growths with and without a supplied Sn flux, showing the streaky RHEED after growth of the Sn doped (001) β-$(Al_xGa_{1-x})_2O_3$ films indicative of smooth surface morphology, whereas a spotty RHEED indicative of a rough surface was observed for the UID (001) β-$(Al_xGa_{1-x})_2O_3$ film.

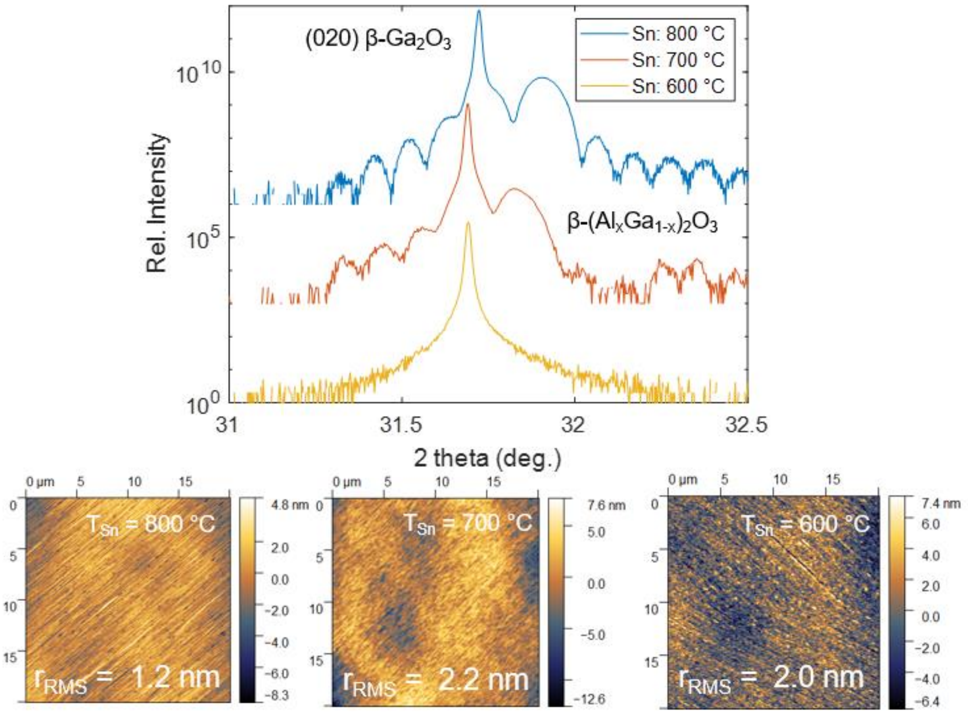

Figure 5.6: HRXRD 2θ-ω scans (001) β-$(Al_xGa_{1-x})_2O_3$ films with various Sn cell temperatures along with corresponding surface morphologies measured by AFM.

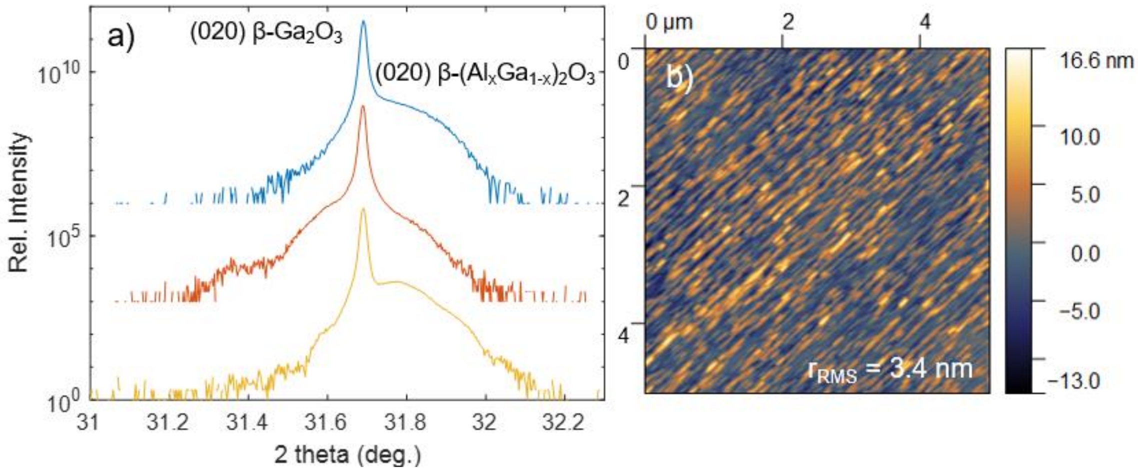

Figure 5.7: HRXRD 2θ-ω scans of various UID (001) β-$(Al_xGa_{1-x})_2O_3$ films along with typical surface morphology for these films measured by AFM.

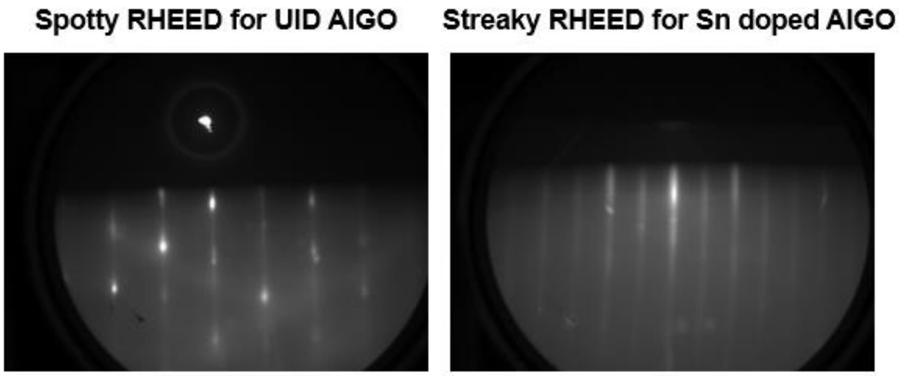
Spotty RHEED for UID AlGO

Streaky RHEED for Sn doped AlGO

Figure 5.8: RHEED images post UID (001) β-$(Al_xGa_{1-x})_2O_3$ and Sn doped (001) β-$(Al_xGa_{1-x})_2O_3$ growth.

Cross-section TEM of a Sn doped (001) β-$(Al_xGa_{1-x})_2O_3$ layer between two β-Ga_2O_3 layers was performed to characterize structural quality. Fig. 5.9 shows the HAADF TEM and electron beam diffraction contrast images of a cross-section of the film, showing no evidence of extended defects in the film. Energy-dispersive x-ray spectroscopy (EDS) was performed to confirm that Al was present in the (001) β-$(Al_xGa_{1-x})_2O_3$ layer and not the β-Ga_2O_3 layers.

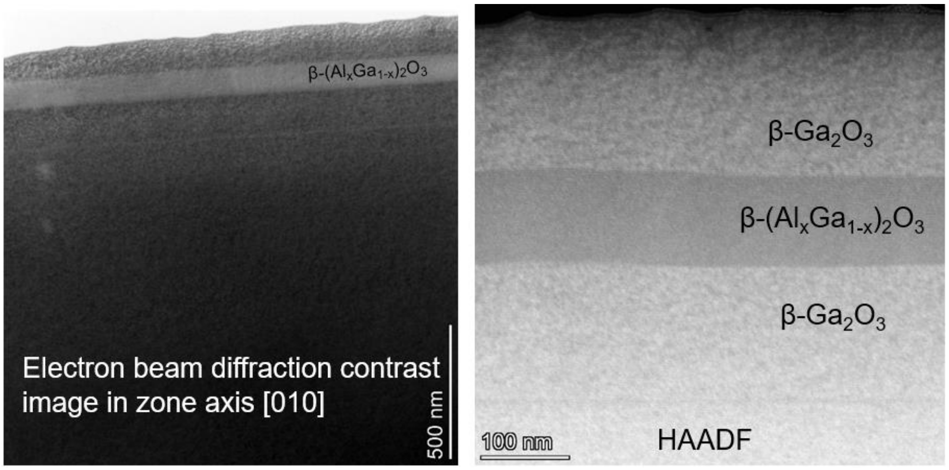

Figure 5.9: Cross-section TEM images of Sn doped β-$(Al_xGa_{1-x})_2O_3$ film between β--Ga_2O_3 layers showing no evidence of extended defects.

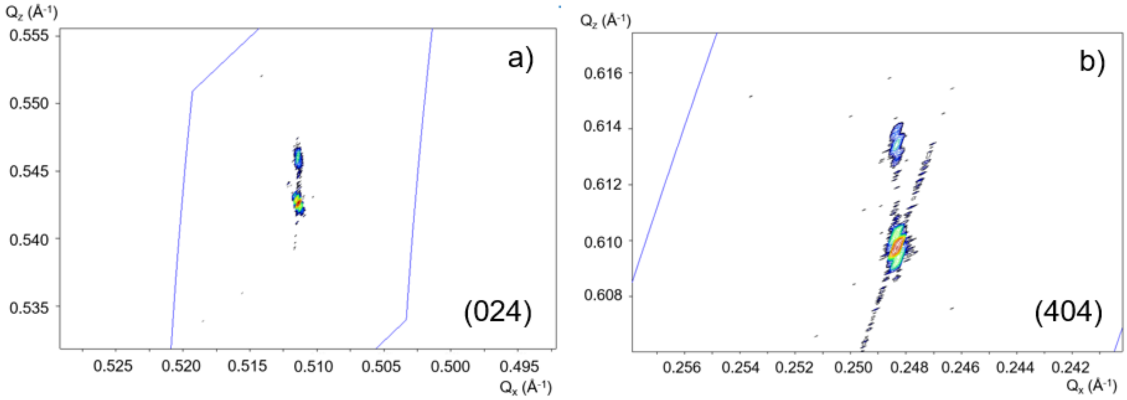

Figure 5.10: Reciprocal Space Maps of (404) and (024) reflections of 90 nm (001) β-$(Al_{0.11}Ga_{0.89})_2O_3$ layer and β-Ga_2O_3 substrate peaks showing coherently strained films.

Reciprocal space maps (RSMs) in HRXRD were performed for the Sn doped β-$(Al_xGa_{1-x})_2O_3$ films to confirm that the layers were coherently strained to the β-Ga_2O_3 beneath them. Fig. 5.10 shows the RSMs for the two asymmetric planes (404) and (024) used to determine and in plane and out of plane lattice parameter of a 90 nm (001) β-

$(Al_{0.11}Ga_{0.89})_2O_3$ layer. As can be observed in the RSMs in Fig 5.10, the out of plane components Q_z of the peaks differ due to the difference in out of plane lattice parameter for the β-$(Al_xGa_{1-x})_2O_3$ layer and β-Ga_2O_3, however the Q_x components are the same, due to the same in plane lattice parameter. RSMs of two planes with non-parallel in plane components were measured to ensure that there was no relaxation in any in-plane direction.

The relationship between the out of plane lattice parameter, and therefore θ angle in XRD for the (002) β-$(Al_xGa_{1-x})_2O_3$ peak, and Al content can be derived for a coherently strained (001) β-$(Al_xGa_{1-x})_2O_3$ film with methods similar to those used for (010) β-$(Al_xGa_{1-x})_2O_3$. The stiffness tensor utilized for the (010) derivation has principal directions [100] and [010] with the third direction, corresponding to ε_3 and σ_3 perpendicular to these two. This corresponds to the out of plane direction for the c-plane. The in-plane components (along the [100] and [010] directions) of the (001) β-$(Al_xGa_{1-x})_2O_3$ film are coherent with the β-Ga_2O_3 beneath it. The out of plane stress component σ_3 is 0 and the out of plane strain ε_3, corresponds to the out of plane lattice parameter. The same relationships between Al content x and relaxed lattice parameter described earlier in the chapter can be used. Equation 5.5 shows the stress-strain relationship using the stiffness tensor set up to solve for out of plane strain for c-plane growth. Equation 5.6 shows a simplified expression in terms of this out of plane strain using the third line of this stiffness tensor.

$$\begin{bmatrix} \sigma_1 \\ \sigma_2 \\ 0 \\ 0 \\ 0 \\ \sigma_6 \end{bmatrix} = \begin{bmatrix} c_{11} & c_{12} & c_{13} & 0 & c_{15} & 0 \\ c_{21} & c_{22} & c_{23} & 0 & c_{25} & 0 \\ c_{31} & c_{32} & c_{33} & 0 & c_{35} & 0 \\ 0 & 0 & 0 & c_{44} & 0 & c_{46} \\ c_{51} & c_{52} & c_{53} & 0 & c_{55} & 0 \\ 0 & 0 & 0 & c_{64} & 0 & c_{66} \end{bmatrix} \begin{bmatrix} \varepsilon_1 \\ \varepsilon_2 \\ \varepsilon_3 \\ \varepsilon_4 \\ \varepsilon_5 \\ \varepsilon_6 \end{bmatrix} \quad \text{(eqn. 5.5)}$$

$$\varepsilon_3 = -\frac{c_{13}\varepsilon_1 + c_{23}\varepsilon_2 + c_{35}\varepsilon_5}{c_{33}} \quad \text{(eqn. 5.6)}$$

Using similar expressions for strain used for the (010) derivation, the out of plane lattice parameter can be derived as a function of Al content x as shown in eqn. 5.7. This can then be related to the Δθ between the (002) β-Ga_2O_3 and β-$(Al_xGa_{1-x})_2O_3$ peaks in HRXRD as shown in eqn. 5.8.

$$x = 18.32 - 3.15c_c \text{ (Å)} \quad \text{(eqn. 5.7)}$$

$$x = 1.13\Delta\theta_{002} \text{ (deg.)} \quad \text{(eqn. 5.8)}$$

The full derivation is shown in Appendix B. A similar derivation for the (100) orientation can be performed, however the x_1 direction of the coordinate system is along the a-direction (not the g_{100} / a* direction) and therefore not in the out of plane direction for (100) oriented films. A transformation of the coordinate system, rotating about the b-axis to put the x_1 direction in this basis along this desired direction is required prior to using similar methodology to relate Al content x and out of plane strain for coherently strained (100) β-$(Al_xGa_{1-x})_2O_3$. This involves a tensor transformation for the stiffness tensor, which is also described in Appendix B.

Finally, confirmation of the actual Al content in the (001) β-$(Al_xGa_{1-x})_2O_3$ films was performed via APT as shown in Fig. 5.11 for a β-$(Al_xGa_{1-x})_2O_3$ film with approximately 14% Al based on peak separation in HRXRD and expression in eqn. 5.8. The average Al content of about 15.6% across the film was measured via APT showing some agreement between calculated Al content from HRXRD peak separation and APT.

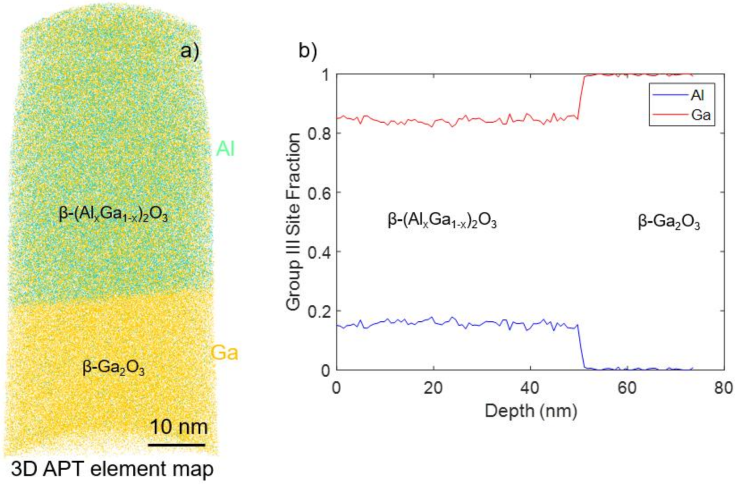

Figure 5.11: APT image and depth profile showing group III site compositions for (001) β-$(Al_xGa_{1-x})_2O_3$ with a measured Al composition of 15.6%.

5.4 Summary

(010) β-$(Al_xGa_{1-x})_2O_3$ growth for Al contents up to 22% were demonstrated via conventional PAMBE and MOCATAXY growth. Ge incorporation into (010) β-$(Al_xGa_{1-x})_2O_3$ was suppressed relative to β-Ga_2O_3, limiting its use as n-type dopant for (010) β-$(Al_xGa_{1-x})_2O_3$ based structures. While Sn doping showed similar incorporation across (010) β-$(Al_xGa_{1-x})_2O_3$ and β-Ga_2O_3, no conductivity was measured via Hall for Sn doped (010) β-$(Al_xGa_{1-x})_2O_3$.

(001) Sn doped β-$(Al_xGa_{1-x})_2O_3$ was grown with up to 15% Al, demonstrating clear thickness fringes in XRD and a high intensity (002) β-$(Al_xGa_{1-x})_2O_3$ peak, and smooth surface morphologies measured via AFM. High structural quality of the films were confirmed via cross-sectional TEM, and RSMs in XRD confirmed that films were coherently strained to the (001) β-Ga_2O_3 substrates. UID β-$(Al_xGa_{1-x})_2O_3$ demonstrated spread out (002) layer peaks in HRXRD and rougher surface morphology indicative of

poorer film quality, suggesting that Sn acts as a surfactant for β-$(Al_xGa_{1-x})_2O_3$. Using the stiffness tensor and stress-strain relations for the (001) β-$(Al_xGa_{1-x})_2O_3$ film, a relationship between out of plane lattice parameter and Al content x could be derived. APT confirmed the actual Al composition in a β-$(Al_xGa_{1-x})_2O_3$ film to be in agreement with the calculated value.

References:

1. E. Ahmadi, O. S. Koksaldi, X. Zheng, T. Mates, Y. Oshima, U. K. Mishra, and J. S. Speck. Appl. Phys. Exp. **10**, 071101 (2017).
2. S. Krishnamoorthy, Z. Xia, C. Joishi, Y. Zhang, J. McGlone, J. M. Johnson, M. Brenner, A. R. Arehart, J. Hwang, S. Lodha, and S. Rajan. Appl. Phys. Lett. **111,** 023502 (2017).
3. K. Ghosh and U. Singisetti. J. Mater. Res. **32,** 224142 (2017).
4. V. G. Hill, R. Roy, and E. F. Osborn. J. Am. Cer. Soc. **35,** 06135 (1952).
5. S. Mu, M. Wang, H. Peelaers, and C. G. Van de Walle APL Mat. **8,** 091105 (2020).
6. J. M. Johnson, H. L. Huang, M. G. Wang, S. Mu, J. B. Varley, A. F. M. A. U. Bhuiyan, Z. X. Feng, N. K. Kalarickal, S. Rajan, H. P. Zhao, C. G. Van de Walle, and J. Hwang. APL Materials. **9**, 51103 (2021).
7. Y. Oshima, E. Ahmadi, S. C. Badescu, F. Wu, and J. S. Speck. Appl. Phys. Exp. **9,** 061102 (2016).
8. C. Kranert, M. Jenderka, J. Lenzner, M. Lorenz, H. von Wenckstern, R. Schmidt-Grund, and M. Grundmann. J. Appl. Phys. **117**, 125703 (2015).
9. P. Vogt, A. Mauze, F. Wu, B. Bonef, and J. S. Speck. Applied Physics Express **11**, 115503 (2018).
10. E. Ahmadi, O. S. Koksaldi, S. W. Kaun, Y. Oshima, D. B. Short, U. K. Mishra, and J. S. Speck, App. Phys. Exp. **10**, 041102 (2017).
11. S. H. Han, A. Mauze, E. Ahmadi, T. Mates, Y. Oshima, and J. S. Speck, Semiconductor Science and Technology **33,** 045001 (2018).
12. A. Mauze, Y. Zhang, T. Itoh, F. Wu, and J. S. Speck, APL Materials **8**, 021104 (2020).
13. A. Mauze, Y. Zhang, T. Itoh, E. Ahmadi, and J. S. Speck. Appl. Phys. Lett. **117**, 222102 (2020).
14. A. T. Neal, S. Mou, S. Rafique, H. Zhao, E. Ahmadi, J. S. Speck, K. T. Stevens, J. D. Blevins, D. B. Thomson, N. Moser, K. D. Chabak, and G. H. Jessen, Appl. Phys. Lett. **113**, 062101 (2018).
15. J. B. Varley, A. Perron, V. Lordi, D. Wickramaratne, and J. L. Lyons. Appl. Phys. Lett. **116,** 172104 (2020).
16. Y. Oshima, E. Ahmadi, S. Kaun, F. Wu, and J. S. Speck. Semiconductor Science and Technology **33**, 015013 (2018).

Chapter 6: Conclusions and Future Work

In this dissertation, PAMBE growth of β-Ga_2O_3 across various orientations was investigated. While conventional PAMBE of (010) β-Ga_2O_3 has shown promising film quality, doping, and heterostructure growth, significant suboxide desorption limits growth rates, structural quality, surface morphology, and electron mobility for other orientations such as (001) and ($\bar{2}$01). MOCATAXY growth, which involves an additional indium flux during PAMBE growth, has shown a significant improvement of β-Ga_2O_3 growth rates across all orientations. Additionally, (001) β-Ga_2O_3 films grown via MOCATAXY demonstrated improved surface morphology, structural quality, and electron mobility compared to conventional PAMBE grown films.

Doping of β-Ga_2O_3 across various orientations was studied in detail for both conventional PAMBE and MOCATAXY of (010) and (001) β-Ga_2O_3 films. Ge doping via conventional PAMBE could reach a range of doping concentrations, however Ge incorporation decreased at higher growth temperatures for both orientations. Ge doping of (001) β-Ga_2O_3 also demonstrated a delay in incorporation. Sn doping across both orientations was demonstrated, with higher doping concentrations than Ge achievable at higher growth temperatures for conventional PAMBE. A significant doping delay and surface segregation effect in (010) β-Ga_2O_3 was observed for Sn, limiting its use for lower donor doping applications for conventional PAMBE. Sn doping via MOCATAXY, on the other hand, demonstrated extremely sharp doping profiles across various Sn concentrations, showing promise for a wide range of donor doping applications. Furthermore, Hall mobility for MOCATAXY grown (010) and (001) β-Ga_2O_3 films were the highest amongst continuously doped MBE films in these orientations. Continuous Si doping of (010) β-Ga_2O_3 using a valved cell allowed for constant doping profiles for high Si concentrations, however films were not conductive enough for Hall measurement. MOCATAXY grown Si doped (001) β-Ga_2O_3 films demonstrated Hall mobility similar to the highest (001) β-Ga_2O_3 mobility for Sn doped films. Temperature dependent Hall measurement of Sn doped (010) β-Ga_2O_3 films revealed a donor level about 77 meV below the conduction band for Sn as well a relatively high background acceptor concentration in the MOCATAXY grown films (on the order of 10^{17} cm^{-3}).

Acceptor doping for conventional PAMBE grown (010) β-Ga_2O_3 films was demonstrated with Mg. A wide range of concentrations was achievable with sharp, controllable doping profiles for the growth temperatures of conventional PAMBE (600 °C to 700 °C). Annealing of Mg doped films at higher temperatures ($\geq$ 925 °C) led to significant diffusion of Mg, limiting its application to lower temperature growth techniques and processing steps. This Mg diffusion was expected to be due to the interstitial Mg species that forms via an exchange reaction with Ga interstitials that diffuse to the Mg doped layer. Fe incorporation from Fe doped (010) β-Ga_2O_3 substrates into conventional PAMBE grown films was also investigated. This effect was determined to be due to surface segregation during film growth, rather than diffusion. Through utilization of a low temperature impurity trapping buffer layer, Fe can be trapped near the substrate, and this incorporation into critical regions of the device structure can be limited.

Growth of the β-$(Al_xGa_{1-x})_2O_3$ for application to heterostructure based devices was also investigated for both the (010) and (001) orientations. Maximum Al fractions on the group III site of 22% and 15% for high quality, coherently strained β-$(Al_xGa_{1-x})_2O_3$ films were demonstrated for the (010) and (001) orientations respectively. These films showed no evidence of extended defects or relaxation. Relationships between out of plane lattice parameter and Al content were also derived using the fundamental stiffness tensor and stress strain relations for β-$(Al_xGa_{1-x})_2O_3$ coherently strained to β-Ga_2O_3.

Advancements in MBE growth and doping of β-Ga_2O_3 and its heterostructures were shown, demonstrating promise for future β-Ga_2O_3 based devices. Still, there are many areas of future work that must be addressed. While MOCATAXY has allowed for high quality films for (010) and (001) β-Ga_2O_3, surface morphology and Hall mobility remain poor for $(\bar{2}01)$ β-Ga_2O_3 films. Additionally, investigation into MOCATAXY growth and doping for other orientations, or miscut from $(\bar{2}01)$ would be interesting to see if improved film quality can be obtained. A better understanding of the role of the indium catalyst during MOCATAXY growth, including adlayer surface coverage, and the interaction between indium and oxygen in the growth environment is also necessary. The role of Sn as a surfactant for (001) β-$(Al_xGa_{1-x})_2O_3$ growth via MOCATAXY should also be studied in further detail, to ultimately achieve high quality UID (001) β-$(Al_xGa_{1-x})_2O_3$ films. If maximum Al contents can also be increased in high quality β-$(Al_xGa_{1-x})_2O_3$ films, this could allow for higher conduction band offsets in β-$(Al_xGa_{1-x})_2O_3$ / β-Ga_2O_3 heterostructures.

Donor and acceptor doping in MBE grown β-Ga_2O_3 films also has much to be investigated. Continuous Si doping in MOCATAXY grown β-Ga_2O_3 has shown more promise for the (001) orientation, but the reason for nonconductive Si doped (010) β-Ga_2O_3

films is still unknown. Additionally, intentional Si doping of MOCATAXY grown (010) and (001) β-$(Al_xGa_{1-x})_2O_3$ has not been studied in detail for application to heterostructure based devices. Further study of acceptors in MBE grown β-Ga_2O_3 via identification of the Mg and Fe acceptor level, and growth of deep acceptor doped / n junctions could be very valuable for future device structures that utilize deep acceptor doping. Other acceptor doping candidates that may experience less diffusion at higher temperatures could also be investigated for MOCATAXY grown β-Ga_2O_3.

Finally, in order to achieve the n- drift regions required for various vertical high power devices, low background ionized acceptor concentrations in MBE grown β-Ga_2O_3 films are needed. Improvement of this material purity is essential to achieve high breakdown voltages and higher mobility in β-Ga_2O_3 films and modulation doped heterostructures. Further development of β-Ga_2O_3 film growth, donor and acceptor doping, and improvement of heterostructures can help achieve viable β-Ga_2O_3 based electronics of the future.

Appendix A

Temperature dependent Hall mobility scattering components:

Fitting of the Temperature dependent Hall mobility was performed using the two primary scattering components in doped β-Ga_2O_3 films: the polar optical phonon scattering and ionized impurity scattering. The expressions for these two scattering rates as represented by Zhang et al.[1] are shown below:

Polar Optical Phonon Scattering Rate (τ_{POP}):

$$\frac{1}{\tau_{POP}(E)} = \frac{e^2\omega_0}{4\pi\hbar\left(\frac{2E}{m^*}\right)^{\frac{1}{2}}}(\varepsilon_\infty{}^{-1} - \varepsilon_S{}^{-1})[N_0\left(1+\frac{\hbar\omega_0}{E}\right)^{\frac{1}{2}} + (N_0+1)\left(1-\frac{\hbar\omega_0}{E}\right)^{\frac{1}{2}} - \frac{\hbar\omega_0}{E}N_0\sinh^{-1}\left(\frac{E}{\hbar\omega_0}\right)^{\frac{1}{2}} + \frac{\hbar\omega_0}{E}(N_0+1)\sinh^{-1}\left(\frac{E}{\hbar\omega_0}-1\right)^{\frac{1}{2}}] \text{ (eqn. A.1)}$$

$$N_0 = \frac{1}{\exp\left(\frac{\hbar\omega_0}{k_BT}\right)-1}\ (phonon\ occupancy\ number) \text{ (eqn. A.2)}$$

$\hbar\omega_0$ is the phonon energy.

k_B is the Boltzmann constant.

ε_S and ε_∞, e, ħ are the static and high frequency dielectric constant, unit charge, and reduced Planck's constant.

Ionized Impurity Scattering rate based on Brooks Herring Model:

$$\frac{1}{\tau_{II}(E)} = \frac{N_Ie^4}{16(2m^*)^{\frac{1}{2}}\pi\varepsilon_S{}^2}[\ln(1+\gamma^2) - \frac{\gamma^2}{1+\gamma^2}]E^{-3/2} \text{ (eqn. A.3)}$$

$$\gamma^2 = 8m^*EL_D{}^2/\hbar^2 \text{ (eqn. A.4)}$$

L_D is the Debye screening length.

For a film with 1 donor and completely ionized acceptors, the total ionized impurity concentration is:

$$N_I = N_D{}^+ + N_A \text{ (eqn. A.5)}$$

Electron mobility can be calculated from these scattering rates using Mattheison's Rule:

Mattheison's Rule for Total Electron Mobility:

$$\mu = \frac{e\langle\tau_m\rangle}{m^*} = \frac{e}{m^*}\frac{\int_0^\infty E^{\frac{3}{2}}\tau_m(E)f(E)dE}{\int_0^\infty E^{\frac{3}{2}}f(E)dE} \text{ (eqn. A.6)}$$

This suggests that effective mobility of various scattering components add in inverse.

$$\frac{1}{\mu_{eff}} = \frac{1}{\mu_1} + \frac{1}{\mu_2} + \cdots \text{ (eqn. A.7)}$$

More specifics of the fitting of the temperature dependent mobility of β-Ga_2O_3 films are shown in Zhang et al.[1]

Additional References:

1. Y. Zhang, F. Alema, A. Mauze, O. S. Koksaldi, R. Miller, A. Osinsky, and J. S. Speck. APL Mat. **7,** 022506 (2019).

Appendix B

Derivation of relationship between Al content x and out of plane lattice parameter for β-$(Al_xGa_{1-x})_2O_3$ coherently strained to β-Ga_2O_3 on various orientations.

Starting with the derivation of the relationship between Al content x and out of plane lattice parameter for (010) β-$(Al_xGa_{1-x})_2O_3$ coherently strained to (010) β-Ga_2O_3, we refer to the stiffness tensor used by Oshima et al.[1] where the unit cell was placed in the Cartesian coordinate system where [100] || $\hat{x}_1$, [010] || $\hat{x}_2$, and g_{001} (same as c*) || $\hat{x}_3$. Voigt notation of the stress-strain tensor is shown below with in plane stress components σ_1 and σ_3, but no out of plane stress component (σ_2). Similarly, the shear components ε_4 and ε_6 are 0.

(010)

$$\begin{bmatrix} \sigma_1 \\ 0 \\ \sigma_3 \\ 0 \\ \sigma_5 \\ 0 \end{bmatrix} = \begin{bmatrix} c_{11} & c_{12} & c_{13} & 0 & c_{15} & 0 \\ c_{21} & c_{22} & c_{23} & 0 & c_{25} & 0 \\ c_{31} & c_{32} & c_{33} & 0 & c_{35} & 0 \\ 0 & 0 & 0 & c_{44} & 0 & c_{46} \\ c_{51} & c_{52} & c_{53} & 0 & c_{55} & 0 \\ 0 & 0 & 0 & c_{64} & 0 & c_{66} \end{bmatrix} \begin{bmatrix} \varepsilon_1 \\ \varepsilon_2 \\ \varepsilon_3 \\ 0 \\ \varepsilon_5 \\ 0 \end{bmatrix} \text{(eqn. B.1)}$$

The Vogt notation of the stiffness tensor for β-Ga_2O_3 in the Cartesian coordinate system described, as calculated by Oshima et al. is expressed below:

$$C = \begin{bmatrix} 237 & 125 & 147 & 0 & -18 & 0 \\ 125 & 354 & 95 & 0 & 11 & 0 \\ 147 & 95 & 257 & 0 & 6 & 0 \\ 0 & 0 & 0 & 54 & 0 & 19 \\ -18 & 11 & 6 & 0 & 67 & 0 \\ 0 & 0 & 0 & 19 & 0 & 95 \end{bmatrix}$$

The definitions of the strain components are expressed below where the in plane lattice parameters are those of β-Ga_2O_3 for the coherently strained β-$(Al_xGa_{1-x})_2O_3$ film.

$$\varepsilon_1 = -\frac{(a_r - a_c)}{a_r} \text{(eqn. B. 2a)}$$

$$\varepsilon_2 = -\frac{(b_r - b_c)}{b_r} \text{(eqn. B. 2b)}$$

$$\varepsilon_3 = \frac{c_c \sin(\beta_c)}{c_r \sin(\beta_r)} - 1 \text{ (eqn. B. 2c)}$$

$$\varepsilon_5 = \frac{c_c \cos(\beta_c)}{c_r \sin(\beta_r)} - \frac{a_c \cos(\beta_r)}{a_r \sin(\beta_r)} \text{ (eqn. B. 2d)}$$

The relaxed lattice parameters shown below for β-$(Al_xGa_{1-x})_2O_3$ have been measured by Kranert et al.[2] and utilized in the derivation by Oshima et al.[1]

$$a_r = a_0 - k_a x \text{ (Å) (eqn. B.3a)}$$
$$b_r = b_0 - k_b x \text{ (Å) (eqn. B.3b)}$$
$$c_r = c_0 - k_c x \text{ (Å) (eqn. B.3c)}$$
$$\beta_r = \beta_0 + k_\beta x\ (deg) \text{ (eqn. B.3d)}$$

$k_a = 0.42$, $k_b = 0.13$, $k_c = 0.17$, and $k_\beta = 0.31$
$a_0 = 12.21$ Å, $b_0 = 3.04$ Å, $c_0 = 5.81$ Å, $\beta_0 = 103.87°$

from the second line of the stress strain relationship in eqn. B.1 we have:

$$\varepsilon_2 = -\frac{(c_{12}\varepsilon_1 + c_{23}\varepsilon_3 + c_{25}\varepsilon_5)}{c_{22}} \text{ (eqn. B.4)}$$

Equating that to the definition of ε_2 from earlier and plugging in definitions of ε_1, ε_3 and ε_5 we get:

$$\frac{1}{c_{22}}\left[c_{12}\frac{a_0-(a_0-k_a x)}{(a_0-k_a x)} + c_{23}\frac{c_0-(c_0-k_c x)}{(c_0-k_c x)} + c_{25}\left(\frac{c_0}{(c_0-k_c x)} - \frac{a_0}{(a_0-k_a x)}\right)\ \cot(\beta_r)\right] = \frac{(b_0-k_b x)-b_c}{(b_0-k_b x)}$$

$$\text{(eqn. B.5)}$$

kx components in the denominators are approximately negligible compared to the a_0, b_0, and c_0 components, so this is approximated as:

$$\frac{1}{c_{22}}\left[c_{12}\frac{k_a x}{a_0} + c_{23}\frac{k_c x}{c_0} + c_{25}\left(\frac{k_c x}{c_0} - \frac{k_a x}{a_0}\right)\ \cot(\beta_r)\right] = \frac{b_0-b_c}{b_0} - \frac{k_b x}{b_0} \quad \text{(eqn. B.6)}$$

Solving for x (Al content) we get:

$$x = \frac{b_0-b_c}{b_0}\left[\frac{k_b}{b_0} + \frac{c_{12}}{c_{22}}\frac{k_a}{a_0} + \frac{c_{23}}{c_{22}}\frac{k_c}{c_0} + \frac{c_{25}}{c_{22}}\left(\frac{k_c}{c_0} - \frac{k_a}{a_0}\right)\ \cot(\beta_0)\right]^{-1} \quad \text{(eqn. B.7)}$$

We now have a relationship between x and out of plane lattice parameter (b_c)

Now let's relate this to the Bragg angle θ for X-ray Diffraction using a Cu Kα source with the 020 reflection.

$$n\lambda = 2d\sin(\theta) \text{ (eqn. B. 8)}$$

Let's define θ_0 and θ_c as the Bragg angles for the β-Ga_2O_3 substrate peak and β-$(Al_xGa_{1-x})_2O_3$ film peak respectively. We can represent the peak separation between the two by δ such that:

$$\theta_C - \theta_0 = \delta = \Delta\theta \text{ (eqn. B. 9)}$$

With trig identities:

$$\sin(\theta_C) = \sin(\theta_0 + \delta) = \sin(\theta_0)\cos(\delta) + \sin(\delta)\cos(\theta_0) \text{ (eqn. B. 10)}$$

Cos (δ) ~1 and sin(δ) is very small so sin(δ) ~ δ

$$\sin(\theta_C) = \sin(\theta_0) + \delta\cos(\theta_0) \text{ (eqn. B. 11)}$$

$$d_{020} = b/2$$

and $d_{020} = n\lambda/\sin(\theta)$ → plug into eqn.

$$\frac{b_0 - b_c}{b_0} = \frac{\frac{1}{\sin(\theta_0)} - \frac{1}{\sin(\theta_0) + \delta\cos(\theta_0)}}{\frac{1}{\sin(\theta_0)}} = \frac{\frac{\sin(\theta_0) + \delta\cos(\theta_0)}{\sin(\theta_0)} - \frac{\sin(\theta_0) + \delta\cos(\theta_0)}{\sin(\theta_0) + \delta\cos(\theta_0)}}{\frac{\sin(\theta_0) + \delta\cos(\theta_0)}{\sin(\theta_0)}} = \frac{1 + \delta\cot(\theta_0) - 1}{1 + \delta\cot(\theta_0)} = \delta\cot(\theta_0)$$

$$\text{(eqn. B. 12)}$$

$$x = \Delta\theta\cot(\theta_0)\left[\frac{k_b}{b_0} + \frac{c_{12}}{c_{22}}\frac{k_a}{a_0} + \frac{c_{23}}{c_{22}}\frac{k_c}{c_0} + \frac{c_{25}}{c_{22}}\left(\frac{k_c}{c_0} - \frac{k_a}{a_0}\right)\cot(\beta_0)\right]^{-1} \text{ (eqn. B. 13)}$$

$$x = 0.4727 \times \Delta\theta \ (\Delta\theta \ in \ degrees) \text{ (for (020) peak) (eqn. B. 14)}$$

$$x = 15.923 - 5.238 \times b_c \text{ (Å)} \quad \text{(eqn. B. 15)}$$

(001)

For (001) β-$(Al_xGa_{1-x})_2O_3$ the same stiffness tensor can be utilized in the same Cartesian coordinate system. Here $\hat{x}_3$ corresponds to the out of plane direction and therefore has no stress (σ_3) component. The in plane stress components are σ_1 and σ_2 and the out of plane strain component is ε_3.

$$\begin{bmatrix} \sigma_1 \\ \sigma_2 \\ 0 \\ 0 \\ 0 \\ \sigma_6 \end{bmatrix} = \begin{bmatrix} c_{11} & c_{12} & c_{13} & 0 & c_{15} & 0 \\ c_{21} & c_{22} & c_{23} & 0 & c_{25} & 0 \\ c_{31} & c_{32} & c_{33} & 0 & c_{35} & 0 \\ 0 & 0 & 0 & c_{44} & 0 & c_{46} \\ c_{51} & c_{52} & c_{53} & 0 & c_{55} & 0 \\ 0 & 0 & 0 & c_{64} & 0 & c_{66} \end{bmatrix} \begin{bmatrix} \varepsilon_1 \\ \varepsilon_2 \\ \varepsilon_3 \\ \varepsilon_4 \\ \varepsilon_5 \\ \varepsilon_6 \end{bmatrix} \text{(eqn. B. 16)}$$

Definitions of strain components are as follows:

$$\varepsilon_3 = \frac{c_c \times \sin(\beta_c)}{c_r \times \sin(\beta_r)} - 1 \text{ (eqn. B. 17a)}$$

$$\varepsilon_1 = \frac{a_c - a_r}{a_r} \text{ (eqn. B. 17b)}$$

$$\varepsilon_2 = \frac{b_c - b_r}{b_r} \text{ (eqn. B. 17c)}$$

$$\varepsilon_5 = \frac{c_c \cos(\beta_c)}{c_r \sin(\beta_r)} - \frac{a_c \cos(\beta_r)}{a_r \sin(\beta_r)} \text{ (eqn. 17d)}$$

Where the second line of the stress-strain relationship can be used to express ε_3 as follows:

$$\varepsilon_3 = -\frac{c_{13}\varepsilon_1 + c_{23}\varepsilon_2 + c_{35}\varepsilon_5}{c_{33}} \text{ (eqn. B. 18)}$$

Equating the two out of plane strain components and plugging in definitions of relaxed lattice parameter for a given Al composition x and we get:

$$\frac{1}{c_{33}}\left[c_{13}\frac{a_0-(a_0-k_a x)}{(a_0-k_a x)} + c_{23}\frac{b_0-(b_0-k_b x)}{(b_0-k_b x)}\right] = \frac{(c_0-k_c x)-c_c}{(c_0-k_c x)} + \frac{c_{35}}{c_{33}}\left(\frac{c_c}{(c_0-k_c x)} - \frac{a_0}{(a_0-k_a x)}\right) \cot(\beta_r)$$
$$\text{(eqn. B. 19a)}$$

$$\frac{1}{c_{33}}\left[c_{13}\frac{a_0-(a_0-k_a x)}{(a_0-k_a x)} + c_{23}\frac{b_0-(b_0-k_b x)}{(b_0-k_b x)}\right] = \frac{(c_0-k_c x)-c_c}{(c_0-k_c x)} + \frac{c_{35}}{c_{33}}\left(\frac{c_c}{(c_0-k_c x)} - \frac{c_0}{(c_0-k_c x)}\right) \cot(\beta_0)$$
$$\text{(eqn. B. 19b)}$$

$$\frac{1}{c_{33}}\left[c_{13}\frac{a_0-(a_0-k_a x)}{(a_0-k_a x)} + c_{23}\frac{b_0-(b_0-k_b x)}{(b_0-k_b x)}\right] = \frac{c_0-c_c}{c_0}\left(1-\frac{c_{35}}{c_{33}}\cot(\beta_0)\right) - \frac{k_c x}{c_0}$$
$$\text{(eqn. B. 19c)}$$

Here the term $\frac{c_{35}}{c_{33}}\cot(\beta_0)$ is about 0.0094, so this term has very small influence on the final Al content (x)

Here a similar approximation is made where kx in the denominators are much smaller than the lattice parameters. Also, $\sin(\beta_c) \sim \sin(\beta_r) \sim \sin(\beta_0)$ and $\cot(\beta_c) \sim \cot(\beta_r) \sim \cot(\beta_0)$. Solving for Al composition x:

$$x = \frac{c_0-c_c}{c_0}\left(1-\frac{c_{35}}{c_{33}}\cot(\beta_0)\right)\left[\frac{k_c}{c_0} + \frac{c_{13}}{c_{33}}\frac{k_a}{a_0} + \frac{c_{23}}{c_{33}}\frac{k_b}{b_0}\right]^{-1} \text{ (eqn. B. 20)}$$

$$x = 18.3228 - 3.1537 c_c \text{ (Å)} \quad \text{(eqn. B. 21)}$$

Relating Al composition x with $\Delta\theta$ peak separation using similar trig identities to the case of (010) and we get:

$$x = \Delta\theta \cot(\theta) \times 18.3228 \text{ (eqn. B. 22)}$$

$$x = 1.13\Delta\theta_{002} \text{ (in degrees) (eqn. B. 23)}$$

(100)

For the case of (100) β-$(Al_xGa_{1-x})_2O_3$, coherently strained to (100) β-Ga_2O_3, a similar approach can be taken. However, because the standard notation of the stiffness tensor (used in Oshima et al.) defines the Cartesian coordinate system basis with [100] ∥ $\hat{x}_1$, [010] ∥ $\hat{x}_2$, and g_{001} (same as c*) ∥ $\hat{x}_3$, no principal axis of the standard cartesian coordinate system (and therefore no stress ε or strain σ component expressed in stress-strain relations from eqn. 1) is out of plane for (100) growth (normal to the a-plane). To facilitate the derivation of the relationship between out of plane lattice parameter and Al content x for (100) β-$(Al_xGa_{1-x})_2O_3$ growth, transformation of the stiffness tensor can be performed so that one of the principal directions is along g_{100} (same as a*). This can be done via a rotation of $\hat{x}_1$and $\hat{x}_3$ axes about the $\hat{x}_2$ axis by 13.7° such that the $\hat{x}_1$ ∥ g_{100} and therefore normal to the (100) plane and $\hat{x}_3$ ∥ [001]. Once the stiffness tensor transformation is complete, the remaining derivation follows that for (001) β-$(Al_xGa_{1-x})_2O_3$ closely.

Standard 4th rank tensor transformation laws can be applied for the 81 components of the stiffness tensor as described by Nye et al. and Newmann et al. where[3-4]:

$$C'_{ijkl} = \sum a_{im} a_{jn} a_{ko} a_{lp} C_{mnop} \quad (\text{eqn. B. }24)$$

Each of the 81 transformed tensor components are the sum of 81 terms. Here the components of the 2nd rank tensor are the direction cosines defined by the transformation of the cartesian coordinate system. In the case of a rotation of the coordinate system about a principle axis $\hat{x}_2$ by an angle θ, the direction cosines a_{ij} are as follows:

$$a = \begin{bmatrix} \cos\theta & 0 & \sin\theta \\ 0 & 1 & 0 \\ -\sin\theta & 0 & \cos\theta \end{bmatrix} \quad (eqn.\text{B. }25)$$

Calculating each of these transformed tensor components C'_{ijkl} using the components C_{mnop} allows us to express the transformed stiffness tensor in Voigt notation as follows:

$$C' = \begin{bmatrix} 257 & 118 & 139 & 0 & -23 & 0 \\ 118 & 354 & 102 & 0 & 17 & 0 \\ 139 & 102 & 353 & 0 & -15 & 0 \\ 0 & 0 & 0 & 65 & 0 & 26 \\ -23 & 17 & -15 & 0 & 59 & 0 \\ 0 & 0 & 0 & 26 & 0 & 84 \end{bmatrix} (eqn.\text{B. }26)$$

With the principal axes of the Cartesian coordinate system being $\hat{x}_1$ ∥ g_{100} (same as a*) and therefore is normal to the (100) plane $\hat{x}_2$ ∥ [010]and $\hat{x}_3$ ∥ [001]. Using this transformed stiffness tensor, the following stress-strain relation can be set up:

$$\begin{bmatrix} 0 \\ \sigma_2 \\ \sigma_3 \\ \sigma_4 \\ 0 \\ 0 \end{bmatrix} = \begin{bmatrix} c_{11} & c_{12} & c_{13} & 0 & c_{15} & 0 \\ c_{21} & c_{22} & c_{23} & 0 & c_{25} & 0 \\ c_{31} & c_{32} & c_{33} & 0 & c_{35} & 0 \\ 0 & 0 & 0 & c_{44} & 0 & c_{46} \\ c_{51} & c_{52} & c_{53} & 0 & c_{55} & 0 \\ 0 & 0 & 0 & c_{64} & 0 & c_{66} \end{bmatrix} \begin{bmatrix} \varepsilon_1 \\ \varepsilon_2 \\ \varepsilon_3 \\ \varepsilon_4 \\ \varepsilon_5 \\ \varepsilon_6 \end{bmatrix} (eqn. \mathrm{B}.27)$$

From the first line, a relationship between out of plane strain and the two in plane strain components can be determined using the transformed stiffness tensor components

$$\varepsilon_1 = -\frac{c_{13}\varepsilon_3 + c_{12}\varepsilon_2 + c_{15}\varepsilon_5}{c_{11}} (eqn. \mathrm{B}.28)$$

The individual strain components for this transformed Cartesian coordinate system are as follows:

$$\varepsilon_1 = \frac{a_c \times \sin(\beta_c)}{a_r \times \sin(\beta_r)} - 1 \ (eqn. \mathrm{B}.29a)$$

$$\varepsilon_2 = \frac{b_c - b_r}{b_r} \ (eqn. \mathrm{B}.29b)$$

$$\varepsilon_3 = \frac{c_c - c_r}{c_r} (eqn. \mathrm{B}.29c)$$

$$\varepsilon_5 = \frac{c_c \cos(\beta_c)}{c_r \sin(\beta_r)} - \frac{a_c \cos(\beta_r)}{a_r \sin(\beta_r)} (eqn. \mathrm{B}.29d)$$

A relationship between Al content x and lattice parameter a_c of the (100) β-$(Al_xGa_{1-x})_2O_3$ can be derived, similar to the case of (001) shown previously:

$$\frac{1}{c_{11}}\left[c_{13}\frac{c_0-(c_0-k_c x)}{(c_0-k_c x)} + c_{12}\frac{b_0-(b_0-k_b x)}{(b_0-k_b x)}\right] = \frac{(a_0-k_a x)-a_c}{(a_0-k_a x)} + \frac{c_{15}}{c_{11}}\left(\frac{c_0}{(c_0-k_c x)} - \frac{a_c}{(a_0-k_a x)}\right) \cot(\beta_0)$$

$$(eqn. \mathrm{B}.30)$$

$$x = \frac{a_0-a_c}{a_0}\left(1+\frac{c_{15}}{c_{11}}\cot(\beta_0)\right)\left[\frac{k_a}{a_0} + \frac{c_{13}}{c_{11}}\frac{k_c}{c_0} + \frac{c_{12}}{c_{11}}\frac{k_b}{b_0}\right]^{-1} \ (eqn. \mathrm{B}.31)$$

$$x = 14.6320 - 1.20a_c \ (eqn. \mathrm{B}.32)$$

Here the term $\frac{c_{15}}{c_{11}}\cot(\beta_0)$ is about 0.022, so this term has a small influence on the final Al content (x).

Using trig identities similar to the case of (010) yields a relationship between peak spacing and Al content x:

$$x = \Delta\theta \cot(\theta) \times 14.6320 \ (eqn. \mathrm{B}.33)$$

$$x = 1.95\Delta\theta_{200} \ \text{(in degrees)} \ (eqn. \mathrm{B}.34)$$

References:

1. Y. Oshima, E. Ahmadi, S.C. Bedescu, F. Wu, and J.S. Speck. Appl. Phys. Exp. **9**, 061102 (2016).
2. C. Kranert, M. Jenderka, J. Lenzner, M. Lorenz, H. von Wenckstern, R. Schmidt-Grund, and M. Grundmann. J. Appl. Phys. **117**, 125703 (2015).
3. J. F. Nye. *Physical Properties of Crystals: The Representations by Tensors and Matrices.* Oxford Science Publications. 1957.
4. R. E. Newnham. *Properties of Materials: Anisotropy, Symmetry, Structure.* Oxford University Press. 2005.